THE UNIVERSITY OF CHICAGO

DEVELOPMENT OF KINETIC INDUCTANCE DETECTORS FOR MM- AND SUB-MM OBSERVATIONS

A DISSERTATION SUBMITTED TO
THE FACULTY OF THE DIVISION OF THE PHYSICAL SCIENCES
IN CANDIDACY FOR THE DEGREE OF
DOCTOR OF PHILOSOPHY

DEPARTMENT OF ASTRONOMY AND ASTROPHYSICS

BY

QING YANG TANG

CHICAGO, ILLINOIS

AUGUST 2021

Dedicated to all the teachers who nurtured my knowledge and growth as a person

TABLE OF CONTENTS

LIST OF FIGURES vi

LIST OF TABLES x

ACKNOWLEDGMENTS xi

ABSTRACT xiii

1 INTRODUCTION 1
1.1 Far Infrared Astronomy 1
1.1.1 Cosmic Microwave Background 1
1.1.2 High Redshift Galaxies 6
1.2 Microwave Kinetic Inductance Detectors (MKIDs) 7

2 PHYSICS OF KINETIC INDUCTANCE DETECTOR 10
2.1 BCS Theory 10
2.1.1 Two Fluid Model and Kinetic Inductance 11
2.2 Mattis-Bardeen Theory 12
2.2.1 Surface Impedance of Superconductors 14
2.2.2 Fractional Frequency Shift with Temperature 17
2.3 Microwave Circuitry 17
2.4 Resonator Circuits 19
2.4.1 S21 Equation 22
2.5 Responsivity 24
2.6 Noise 26
2.6.1 Fundamental g-r Noise 26
2.6.2 Photon Noise 27
2.6.3 Two-Level System Noise 27
2.6.4 Other Noise Sources 28
2.6.5 Noise Analysis 29
2.7 MKID Designs 34
2.7.1 CPW Resonator 34
2.7.2 Lumped-Element KIDs 35

3 ANTENNA-COUPLED KIDS FOR CMB DETECTION 37
3.1 Introduction 37
3.2 Design 38
3.2.1 Millimetre-Wave Coupling 38
3.2.2 Prototype Array 40
3.3 Fabrication 43
3.3.1 Lens Seating Wafers 46
3.4 Experimental Setup 47
3.4.1 Cryostat Setup 47

3.4.2 Resonator Box . . . 50
3.4.3 Measurement Setup . . . 50
3.4.4 Optical Measurement Setup . . . 51
3.5 Microstrip Test to Characterize SiN Dielectric . . . 52
3.5.1 Data Fitting . . . 53
3.6 Results . . . 53
3.6.1 Characterizing Resonators . . . 53
3.6.2 Noise Performance . . . 55
3.6.3 Optical Performance . . . 55
3.7 Summary . . . 57

4 OMT-COUPLED KIDS FOR CMB DETECTION . . . 59
4.1 Introduction . . . 59
4.2 Design . . . 60
4.3 Fabrication . . . 61
4.4 Setup . . . 65
4.5 Optical Results . . . 66
4.6 Summary and Future Work . . . 67

5 CHARACTERIZING MM-WAVE EMISSIONS FROM OPTICALLY SELECTED GALAXIES . . . 68
5.1 Introduction . . . 68
5.2 Data . . . 69
5.2.1 Stellar Mass Catalog . . . 69
5.2.2 Herschel/SPIRE . . . 73
5.2.3 SPT-SZ/SPTPol . . . 73
5.2.4 Data Processing . . . 74
5.2.5 Matched Filter Algorithm . . . 77
5.3 Method . . . 79
5.3.1 SED Fitting . . . 80
5.3.2 Effective Frequency Bands . . . 83
5.3.3 K-to-Jy Conversion . . . 84
5.4 Results . . . 85
5.4.1 Stacking . . . 85
5.4.2 Quiescent Galaxies . . . 86
5.5 Next Steps and Future Work . . . 87
5.5.1 Galaxy Clustering Bias . . . 87
5.5.2 Estimation of CIB Contribution . . . 89
5.5.3 Galaxy Luminosity . . . 90
5.5.4 Other Applications . . . 90

LIST OF FIGURES

1.1 Temperature and polarization power spectrum of the CMB. Image taken from Abazajian et al. (2016). 3

1.2 Description of how KIDs work. a) Incoming photon with energy $h\nu > 2\Delta$ breaks a Cooper pair into excited quasiparticles in a superconducting material. b) The superconducting material can be designed into a LC resonance circuit with a kinetic inductance L_k and geometric inductance L_m. The circuit is capacitively coupled to a transmission readout line. c) In frequency space, the circuit normally resonates at frequency f_r. When L_s is changed due to a temperature change or incoming photon, it will shift the resonance. The change in R_s results in a broadened and shallower resonance. d) The readout signal undergoes a phase shift at the resonance frequency. This changes slightly when a change in L_s occurs. Image taken from Gao (2008) with permission. 8

2.1 The fractional number density of quasiparticles n_{qp} and number density of superconducting charge carriers n_s to the total charge carrier number density n as described by the two-fluid model. 12

2.2 Fractional frequency shift with temperature variations. The fit parameters were extrapolated by fitting to Equation 2.26 and 2.55 (see Section 2.6.3 for a detailed discussion of Equation 2.55). 18

2.3 A schematic on the 2-port diagram. 18

2.4 Left: Figure of $|S_{21}|$ of a resonator as a function of frequency. Right: I and Q plot of the same resonator. Note that the resonance occurs at the frequency where the IQ circle is closest to the origin. 20

2.5 Circuit diagram of a parallel RLC resonance circuit. The resonator is capacitively coupled to a transmission line using a coupling capacitor C_c. 20

2.6 A S_{21} plot of a sample resonator data in blue dots and the corresponding fit in orange line. 24

2.7 S_{21} of a resonator at $\sim$ 136 mK in a dark environment (blue and red dashed curves) and an optical environment with a 10 K blackbody (solid black curve). Note the resonance shift and the degradation in Q (shallower and wider resonance dip). 25

2.8 IQ plot of the raw data taken for noise analysis. First, a low resolution sweep is done to capture both the resonance and the off-resonance data. A high resolution sweep is done specifically at the dip of the resonance. Then time-stream data is taken where the tone is set to the resonance frequency and an off-resonance frequency. The time-stream data manifests itself as a "noise ball" in the IQ plane. 30

2.9 Plot showing the IQ resonator data before and after cable delay. Notice that all the off-resonance points condensed into a single point on either side of the resonance after cable delay. 31

2.10 Plot showing the high resolution IQ sweep before and after the rotation and translation. A circle centred at the origin is drawn to show that the data after the transformation aligns perfectly with the circle, the on-resonance portion lined up in the direction of the I-axis. 31

2.11 Frequency to phase fitting for a sample high resolution IQ sweep data, with fit parameters. 32
2.12 Noise PSD of a sample resonator, along with fit to Equation 2.63. 33
2.13 Varying noise contributions to the detector. Taken with permission from Barry et al. (2018). 34
2.14 Diagram of a $\lambda/4$-resonator. 35
2.15 Diagram of a LEKID resonator. Note that the inductor is a long meander and capacitor is a series of IDC fingers. 36

3.1 Design layout of the antenna-coupled KID for CMB detection. Dual-slot antenna is coupled to a Nb microstrip line, which feeds the signal to LEKIDs. As a test structure, a "dark" KID was incorporated in the design to measure any photon detection via ways other than the antenna-microstrip structure. Taken with permission from Barry et al. (2018). 39
3.2 Bird-eye overview of the prototype array. There are 7 lenslets on the chip, with an optical and dark KID for each pixel. There are also 5 additional ancillary KIDs to diagnose the device: two dark KIDs (NL) that have the same geometry as the KIDs underneath lenslets, two dark KIDs that have silicon nitride coverage (NL, SiN), and 1 dark bare Al KID. The ground plane layer of the design, including the antenna slots, is not shown to avoid overcrowding the figure. 42
3.3 Cartoon of cross section view of the wafer during all the processing steps. The bottom right figure shows the microwave readout region, the IDC, and the mm-wave transmission line from left to right. See text for details of process steps. . . 44
3.4 *Left.* Optical microscope image of the antenna and Nb microstrip structure. *Middle.* Optical microscope image of the feedline coupled to the KID. The KID is capacitively coupled to the Nb feedline at the bottom. *Right.* Scanning electron microscope (SEM) image of a fabricated single polarization antenna-coupled KID. 46
3.5 *Left.* Photograph of the lens seating wafer partially populated with alumina lenslets. *Right.* SEM image of a SU-8 post on the lens seating wafer. The diameter is measured to be roughly 500 µm and the height is 70 µm. 47
3.6 *Left.* IR microscope image of the alignment of SU-8 posts to holes by viewing two wafers with different features lying one on top of another. Each rectangular bar measures 50 µm x 200 µm. Rectangles of the same orientation are on the same wafer. When perfectly aligned, the ends of four orthogonal rectangles should form a square, as shown in the upper left inset image. We estimate misalignment to be no more than 20 µm. *Right.* Side view of the lens wafer when the posts are misaligned with the holes (top) and aligned (bottom). A cartoon is shown as a comparison to illustrate SU-8 post and hole alignment. The posts are shown in purple and wafers in gray. 48
3.7 *Left.* Photograph of the device chip mounted in a resonator box. *Right.* Photograph of the lens-side of the resonator box. The 150 GHz bandpass filter is not shown. 50

3.8 Schematic of the single-tone homodyne readout configuration for noise measurement. A synthesizer produces a single tone, which is split into two paths. One goes through various attenuation and into the cryostat, where the signal is amplified after it passes through the device. After room temperature amplification, the signal passes through a low-pass filter (LPF) and then goes into the RF port of an IQ mixer. The other end from the splitter goes directly into the LO port of the splitter. The output of the IQ mixer are I and Q of the S_{21}. These signals are passed through a LPF before being digitized by an ADC and collected into the computer for storage and analysis. 52
3.9 *Left.* Optical microscope image of the test Nb microstrip with SiN_x structure. *Right.* Plot of Q_i values obtained from S21 curves at different temperatures of the Nb microstrip with an input power of ≈ -90 dBm. The degradation in Q at $T < 500$ mK is attributed to two-level system behaviour, while at $T \gtrsim 1$ K, this is due to thermally excited quasiparticles. 53
3.10 S_{21} of a sample resonator on a prototype array. 54
3.11 Plot of the internal and coupling quality factors (Q_i and Q_c) obtained from fitting to the S_{21} data of the VNA resonator sweeps. 54
3.12 Fractional frequency noise spectrum and NEP of the detector. A fit is done (dashed red line) to extrapolate the quasiparticle lifetime $\tau_{qp} = 850\,\mu s$. The inset figure shows the dark responsivity, namely the fractional frequency shift as a function of quasiparticle density, that goes into the NEP calculation in Equation 2.64. This is obtained by looking at the dark response for KIDs with various inductor volumes. Taken with permission from Barry et al. (2018). 56
3.13 Fractional frequency shift of the optical and dark resonator under lenslet E as a function of blackbody temperature, showing the dark resonator (blue and orange dots) are seeing ∼35% of optical power as the optical resonator (red and green dots). This measurement also showed that heat sinking the resonator box did not significantly affect the resonance frequency. 57

4.1 *Left.* Layout design of an pixel on the chip. *Right.* Labelled close-up of the OMT structure coupled to a KID through a microstrip. 62
4.2 Cartoon of cross section view of the wafer during all the processing steps. The bottom right figure shows the OMT and mm-wave transmission line, the IDC, and the microwave readout region from left to right. See text for details of process steps. 63
4.3 Photograph of a finished device. 65
4.4 Feedhorn used in the OMTKID optical setup. 66
4.5 Comparison of the optical vs dark KID response on the OMTKID array. 67

5.1 The distribution of galaxies as a function of photometric redshift and stellar mass. 71
5.2 Galaxy density of the SSDF-DES stellar mass catalog used in this work. Density smoothed by 5' Gaussian beam for display purposes. The regions with the lowest densities reside in the vicinity of bright stars which are accounted for in our galaxy survey mask. 72

5.3 Work flow diagram of making filtered maps for SPT and *Herschel*. The map is first masked and the matched filter is calculated using properties of the map and source profile. Then the masked map is convolved with the matched filter to make filtered maps. 75
5.4 A 2D optimal filter at 150 GHz used for this analysis. 79
5.5 SPTpol 150 GHz raw map (top left) and the equivalent map that has been matched filtered for point sources (top right). Colour scale for both maps are modified to ignore bright sources and show the fluctuation variations. Bottom shows a 25'x25' cutout centred on a SMG. Units of all maps are expressed in temperature fluctuations (ΔT) of milliKelvin (mK). 80
5.6 Work flow diagram of making stacked galaxy SEDs. First, galaxies are divided into different redshift and stellar mass bins. For each bin, all the galaxy fluxes are averaged for every filtered map. Errors are estimated by using bootstrap over 100 realizations of the galaxy samples in the bin. 81
5.7 Work flow diagram of fitting method to the stacked galaxy SEDs. Due to computation constraints, we compute beforehand the effective frequencies a table of different blackbody temperatures and redshifts, effectively creating a lookup table of template blackbodies. The algorithm iteratively fits each template blackbody to the stacked SED data and fits for the amplitude of the dust and tSZ component and the χ^2 value is calculated. The best fit model corresponds to the blackbody template with the smallest χ^2 value. 82
5.8 SED composed of stacked fluxes of 24 SPTpol galaxy clusters in the redshift of $0.15 < z < 0.55$. Errorbars are calculated using the bootstrap method over 50 realizations. The lack of fitting at 220 GHz band may come from not accounting for the SZ selection in this sample. 83
5.9 Stacked galaxy fluxes (black dots) divided into redshift bins (columns) and stellar mass bins (row) along with its best SED fit (purple dashed line). The errorbars are within the size of the dots (roughly $\pm$0.1 K). The number of objects in each bin and the dust temperature obtained from fitting are also shown. 86
5.10 Temperatures from the best fit modified blackbody SEDs (Equation 5.8) of stacked galaxy fluxes. *Left:* Dust temperature correlation with redshift for different stellar mass bins. *Right:* Dust tmeperature correlation with stellar mass for different redshift bins. The errors for the temperature fit are roughly $\pm$0.1 K, which are within the size of the markers. 87
5.11 Stacked fluxes of quiescent galaxies (defined as log(SFR) < -11) along with the fit. 88

LIST OF TABLES

3.1 Design parameters for the different MKIDs on the prototype array. 43
3.2 Lithography details for fabrication of detector wafer and lens seating wafer. Step number matches the process step shown in Figure 4.2. 44
3.3 Recipes used for fabrication. Step number matches the processes shown in Figure 4.2. 46

4.1 Lithography details for fabrication of detector wafer. Step number matches the process step shown in Figure 4.2. 64
4.2 Recipes used for chemical vapor deposition and plasma etch. Step number matches the processes shown in Figure 4.2. 64

ACKNOWLEDGMENTS

I acknowledge that the University of Chicago and its surrounding areas, where I have resided for the past six years, sits on the traditional homelands for the Council of the Three Fires: the Odawa, Ojibwe and Potawatomi Nations. Many other Tribes like the Miami, Inoka, Menominee, Ho-Chunk, Sac, and Fox also call this region home.

I have been blessed to work with so many amazing scientist over the course of my PhD. First and foremost, I thank my advisor, Prof. Erik Shirokoff, for supporting and guiding me and being such a kind advisor and always available whenever I needed help. I also thank the members of my thesis committee, Prof. John Carlstrom, Prof. Wayne Hu, and Prof. Abigail Vieregg, for their guidance during my PhD. I would also like to highlight the support from Dr. Pete Barry and Dr. Lindsey Bleem. Pete, thank you for teaching me everything about detector physics and design. Lindsey, thank you for being patient with me while teaching an instrumentationalist about statistics and data analysis. As someone who has never stepped in a cleanroom before, I am forever indebted to the Pritzner Nanofabrication Facility staff, especially Peter Duda and Anna Mukhortova for being such great teachers and so patient with my never-ending questions. I've also had the honour in working alongside a plethora of great scientists in the Shirokoff group and the South Pole Telescope collaboration, ranging from professors, postdocs, undergraduates and fellow graduate students, all of whom have graciously passed their knowledge onto me. I am thankful to all the support staff and workers in my life who are vital in keeping my workplace in a working state, and especially to Laticia Rebeles and Jennifer Smith, for their help in supporting the department graduate students. I would also like to thank Dr. Alessandro Monfardini and NIKA group during my brief stay at Institut Neel in Grenoble for their warm welcome. Merci beaucoup pour tout!

I'm also grateful to the friends I've made during my time in Chicago. To Josh and Ryan, thank you for being such awesome office mates, I will miss all the cat story exchanges! Thank you to Nora, Gourav, Jason, Mandy, Phil, Huanqing, Meng-Xiang, Cory, Celeste, John, Fei, Rebecca, Adina, Andrea, Emily, Maya, Ross, and many others, for all the happy

hour $1 pizzas, Jimmy's, board game & video game nights, cooking & baking parties, general parties, outdoor BBQs, softball games, Chicago city outings, watercolour painting sessions, and much more. I am especially thankful to those who made my first year in Chicago such a treasured memory in my heart and solidified my sense of belonging in this community.

To my beloved friend, Melanie Wong-King-Cheong, thank you for always being there and listening to me, I'm so lucky to have you in the past ten years of my life. Lastly and most importantly, I'd like to thank my family. 妈，爸，哥们儿，丽丽，大黄，谢谢你们为我所付出的一切。

ABSTRACT

Kinetic inductance detectors (KIDs) are a type of athermal pair-breaking superconducting detectors. Several superconductors have an energy gap on the order of 0.1eV, which makes KIDs well-suited for mm and sub-mm wave observations. Compared to their counterparts in this regime, KIDs have innate multiplexing capabilities which makes them ideal in experiments requiring a large number of detectors. The first half of this thesis discusses the design, fabrication, and characterization of a prototype KID array for CMB observations, made out of Al/Nb KIDs coupled to a Nb/SiN/Nb microstrip.

Another target of the future observations using KIDs will be surveying dusty star-forming galaxies (DSFG). They are believed to make up the light emitted in the universe in the infrared and mm-wave regime, known as the cosmic infrared background (CIB). However, the link between DSFGs and the sources that make up the cosmic optical background is still unclear. The second half of this thesis describes the characterization of mm-wave emission in the SPT-SZ, SPTpol, and Herschel SPIRE bands of optically-selected galaxies from the DES Year 3 catalog.

CHAPTER 1

INTRODUCTION

1.1 Far Infrared Astronomy

Far-infrared astronomy is a relatively new field compared to observations in other parts of the electromagnetic spectrum. Observing in this frequency band, also known as the millimeter (mm) and sub-mm band, has historically been challenging due to atmospheric absorption bands due to molecules such as water vapour. Yet, observations at these wavelengths contain a wealth of information which can further our understanding of the universe.

1.1.1 Cosmic Microwave Background

First detected by Penzias & Wilson (1965), the cosmic microwave background (CMB) is often called the first light of the universe. In early universe, baryons and photons were bound together by Thomson scattering. As the universe expanded and cooled, neutral hydrogen was eventually able to form. The previously trapped photons from the photon-baryon plasma were able to free-stream. This light became known as the CMB.

The CMB is one of the most important probes for studying cosmology. Subsequent observations were able to tighten the constraints on the current cosmological model, known as the Lambda Cold Dark Matter (ΛCDM) model. Most notably, the COBE satellite (Fixsen et al., 1996), was the first to confirm the CMB has a blackbody spectrum of roughly $T_0 = 2.73$ K, along with slight deviations at roughly one part in 100000. In the late 2000s, WMAP mapped the first three peaks and troughs of the CMB power spectrum (Bennett et al., 2003). As of now, the latest full-sky measurement of the CMB comes from the *Planck* satellite, which finished observing in 2013 (Planck Collaboration et al., 2020). In addition, there are several on-going ground-based experiments that aim to study more cosmology with the CMB, such as South Pole Telescope (SPT) (Benson et al., 2014), Background Imaging of Cosmic

Extragalactic Polarization (BICEP) Array (Hui et al., 2018), and Simons Observatory (Ade et al., 2019), to name a few.

Features of the CMB

A full description of the cosmology that can be done with CMB measurements is well beyond the scope of this thesis. Instead, the following contains a brief overview of the main features of the CMB and its implications on cosmology.

At an initial glance, the CMB is incredibly homogeneous. To see the small anisotropies, one needs to plot the angular power spectrum, which can be done by decomposing the temperature map of the sky into spherical harmonics

$$T(\theta, \phi) = \sum_{lm} a_{lm} Y_{lm}(\theta, \phi) \tag{1.1}$$

where l is the multipole number, m is the azimuthal number, $Y_{l,m}$ is the spherical harmonics, and a_{lm} is the coefficient. The power spectrum can then be calculated by

$$C_l = \langle a_{lm}^2 \rangle \tag{1.2}$$

The most prominent anisotropy comes from the CMB *dipole* ($l = 1$), which has an amplitude of roughly 3 mK. This naturally arises due to Earth's motion through the background isotropic universe, resulting in a temperature distribution of $T = T_0[1 + (v/c)\cos\theta]$. When the dipole is subtracted from the CMB, the resulting anisotropy contains a plethora of information about the very early universe. The power spectrum of the CMB is shown below in Figure 1.2.

The first peak of the CMB is sensitive to the curvature of the universe. This can be calculated using the size of the sound horizon at recombination and what the angular size should be today. Current measurements of the CMB peak at $l \approx 200$ are extremely consistent with

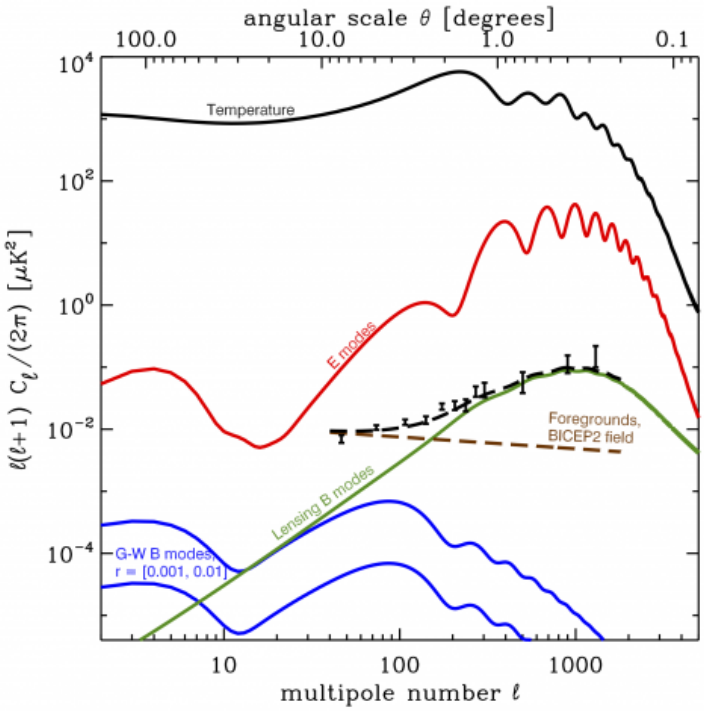

Figure 1.1: Temperature and polarization power spectrum of the CMB. Image taken from Abazajian et al. (2016).

a flat universe. The second peak (or rather, the ratio of the odd-to-even peaks), can constrain the baryon density of the universe. In the primordial universe, baryons contribute the gravitational potential wells. The odd peaks correspond to how much the plasma compresses whereas the even peaks inform us how much the plasma rarefies. Increasing baryon density would mean more suppression of the second peak relative to the first. Higher order peaks indicate the dark matter density in the universe. This is because in a radiation-dominated universe, at maximal compression, the photons would redshift with the expanding universe, causing the gravitation potential wells to decay away and driving the acoustic peaks higher in amplitude. Conversely, in a matter-dominated universe, the gravitation potential would not change, leading to relatively smaller peaks and fluctuations. If the first three peaks can be measured accurately, then the effects of dark matter density can be disentangled from the baryon density. At even higher multipoles, the physical scale becomes comparable to the scale of random walks of photons. Over a wavelength of perturbation, the temperature

fluctuation will be smoothed out and become more damped at even smaller scales. This damping tail serve as an important check for the underlying theory, such as the Gaussianity of the fluctuations.

We can also detect polarization signals from the CMB. Unlike temperature fluctuations, polarization is only produced by scattering. The two types of polarization are called E-modes and B-modes, which is analogous to the E and B field of classic electrodynamics. E modes arise from Thomson scattering off density fluctuations in the plasma. E modes were discovered in 2002 by Degree Angular Scale Interferometer (DASI) (Kovac et al., 2002). Conversely, B-modes comes from the gravitational waves during inflation, immediately after the Big Bang. The B-mode signal is much weaker than the E-mode signal. Coupled with the difficulties in removing foregrounds, their detection is much more difficult than that of E-modes. The first detection of B-modes was done by SPT in 2013 (Hanson et al., 2013), which came from gravitational lensing of E-modes. There still has been no detection of primordial gravitational B-modes at the time of this thesis.

Future CMB Experiments

Future CMB experiments will provide several key measurements in particle physics and cosmology. The CMB-Stage 4 (S4) is a next generation CMB experiment set to deploy around 2025 (Abazajian et al., 2016). The aim is to deploy detectors on telescopes located at the Chilean desert and the South Pole.

The major science goals of CMB-S4 will be briefly discussed below, which is a brief summary from Abazajian et al. (2016). Please note that the science to be done with CMB-S4 far exceeds this short list.

- **Inflationary B-modes**: An unambiguous detection of primordial gravitational B-modes will be the final proof for inflation and solidify the current cosmological models. CMB-S4 aims to detect the tensor-to-scalar ratio (amplitude of the B-mode signal to the E-mode signal) r to $r \lesssim 0.001$. A non-detection at that scale would mean the

current inflationary cosmological model must be reworked. In addition, the energy scales during inflation are around 10^{16} GeV. Thus, CMB-S4 would be a direct probe for extremely high energy physics.

- **Neutrino mass hierarchy**: Neutrinos do not participate in gravitational collapse until late times when they have become non-relativistic. Thus, primordial fluctuations in the neutrino density are damped away on scales smaller than the horizon at that time and only perturbations to the dark matter and baryons remain. These perturbations grow more slowly because neutrino energy density contributes to the expansion rate but not source potentials, causing a suppression in the amplitude and growth rate of matter perturbations at smaller scales. The CMB is directly sensitive to the matter spectrum. By extracting the sum of neutrino masses from the effects on the matter spectrum, the neutrino mass hierarchy can be disentangled.

- **Light relics**: The damping tail of the CMB power spectrum is sensitive to the radiation energy density, which dictates the expansion of the universe in the early universe. CMB-S4 aims to extend the damping tail to higher multipoles ($l \sim 5000$), which would be sensitive to thermal light relics from the Big Bang that would contribute to the radiation energy density, such as axions and sterile neutrinos.

- **Dark energy**: Gravitational lensing of the CMB are great tracers of structure in the universe. We can greatly improve our current understanding of dark energy and the acceleration of the universe by studying the expansion rate (H, or the Hubble constant) and amount of clustering (σ_8) as a function of time. CMB-S4 can accomplish this by synergizing with other galaxy surveys such as the Rubin Observatory.

Current target sensitivity for the experiment is estimated to be around 1.0 µK arcmin. Since the detector technology has improved to the extent of being photon noise-dominated, the only way to reach this sensitivity is by increasing the number of detectors. Indeed, CMB-S4 aims to deploy around $O(10^5)$ detectors, an order of magnitude improvement over

current CMB experiments that deploy around $O(10^4)$ detectors. Multi-frequency bands are needed to characterize and subtract foregrounds, such as dust and synchrotron radiation. Although the traditional detector technology, transition-edge sensor (TES) bolometers, is well understood and remains the baseline plan for CMB-S4, scaling to such a large number of detectors remains a challenge.

1.1.2 High Redshift Galaxies

In early galaxies where most star formation occurred, UV light from stars is absorbed by surrounding dust and gas and reemitted at far-infrared wavelengths, which are then redshifted to mm-wavelengths as they travel to Earth. Due to dust obscuration, these galaxies, known as sub-mm galaxies (SMGs), are often only observable in the sub-mm band. SMGs are some of the oldest and farthest galaxies in our universe and have extremely high star formation rates. Observations at these wavelengths both locally, in the Milky Way, and on the extragalactic scale are vital to forming a complete understanding of star formation from earliest collapse to stellar birth and galaxy evolution processes including during the epoch of reionization, when the first stars turned on.

The first SMG surveys were done by the Submillimetre Common-User Bolometer Array (SCUBA), in which ~ 200 bright high redshift galaxies were discovered Blain et al. (2002). These galaxies were predicted since the COBE satellite's observation of the cosmic infrared background (CIB). When compared to optical galaxy surveys, the measurement of the CIB necessitates a population of dusty star-forming galaxies not observed in the optical bands. Thus, SMGs make up a considerable amount of the energy output of the universe. More recently, surveys from the *Spitzer Space Telescope* and *Herschel Space Observatory* as well as observations from ground-based telescopes like the SPT have catalogued millions of SMGs. Observations of these galaxies is extremely important since they serve as a probe for early star formation. The star formation rate of these galaxies have been estimated to be as high as several thousand solar masses per year (Casey et al., 2014), proving these galaxies to be

an excellent probe of astrophysics in a very star-formation dense environment.

Detection of SMGs

To measure the redshift and understand the structure of distant galaxies, spectroscopy of atomic and molecular lines is key in the sub-mm and mm bands. In particular, the [CII] (ionized atomic carbon) and the CO (carbon-monoxide) rotational emission lines are extremely bright in the sub-mm band for galaxies at high redshifts. Matching these lines allows us to readily identify the redshifts of these galaxies, critical to survey science and cosmology using high redshift galaxies. The [CII] and CO lines are coolants of atomic and molecular gas respectively. Thus, in addition to estimating the star formation rates from [CII] lines, we can use both [CII] and CO lines to differentiate heating mechanisms in the dense regions of galaxies. Obtaining spectroscopic information about the early universe can probe the epoch of reionization, star-formation in galaxies, active galactic nuclei, black hole growth and the birth of galaxies.

Current leading mm and sub-mm telescopes such as ALMA have extraordinarily high resolution and sensitivities for single-object observations, but limited bandwidth and small fields of view make blind redshift surveys impractical. Traditional grating spectrometers can be cumbersome due to their size, complex 3D structure, and thus, cost. There is a strong need for developing a spectroscopic survey of SMGs in the sub-mm band.

1.2 Microwave Kinetic Inductance Detectors (MKIDs)

Developed by Day et al. (2003), kinetic inductance detectors (KIDs) are a type of athermal superconducting detectors. When cooled to below T_c, the electrons condense into states known as Cooper pairs with a band gap energy, Δ, relative to the higher energy states, similar to semiconductors. The band gap energy is related to T_c by $2\Delta \approx 3.5 k_B T_c$.

In a KID, any incident light with energy $E = h\nu > 2\Delta$ will break up a Cooper pair into

quasiparticles. These quasiparticles are electrons in higher energy states. The number of quasiparticles generated is described by $N_{qp} = \eta h\nu/\Delta$, where η is the efficiency of creating quasiparticles. This change in quasiparticle density δn_{qp} causes a change in the complex surface impedance of the superconductor, $Z_s = R_s + i\omega L_s$, where R_s is the resistive term associated with quasiparticles and L_s is the kinetic inductance arising from Cooper pairs' inertia in a changing electric field. After a timescale of $\tau_{qp} \approx 10^{-3} - 10^{-6}$s, the quasiparticles recombine into Cooper pairs. This change, δZ_s, can be measured using a resonant circuit, where the width and frequency of the resonance (f_r) is altered by changes in R_s and L_s respectively when operated as a LC circuit. See Figure 1.2 for a visual schematic of a KID design.

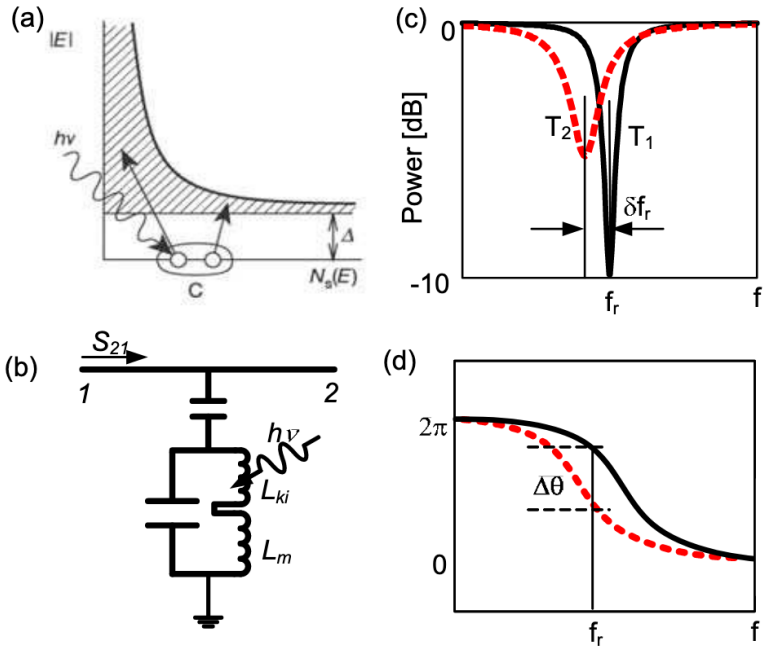

Figure 1.2: Description of how KIDs work. a) Incoming photon with energy $h\nu > 2\Delta$ breaks a Cooper pair into excited quasiparticles in a superconducting material. b) The superconducting material can be designed into a LC resonance circuit with a kinetic inductance L_k and geometric inductance L_m. The circuit is capacitively coupled to a transmission readout line. c) In frequency space, the circuit normally resonates at frequency f_r. When L_s is changed due to a temperature change or incoming photon, it will shift the resonance. The change in R_s results in a broadened and shallower resonance. d) The readout signal undergoes a phase shift at the resonance frequency. This changes slightly when a change in L_s occurs. Image taken from Gao (2008) with permission.

KIDs' main advantage is their innate multiplexing capabilities. Each KID can be designed with a slightly different geometry to have a different inductance and/or capacitance. Thus, each KID can be coupled to the feedline and have a unique resonance frequency. A single silicon germanium (SiGe) amplifier can readout thousands of detectors at once. Additionally, they have low noise, where its intrinsic noise comes from the generation and regeneration of quasiparticles. However, excess phase noise dominating low frequencies and at low temperatures arising from two level systems (TLSs) from surfaces of metals and dielectrics has been observed. Although the physics behind TLS is not very well-understood, TLS noise can be mitigated by minimizing the surface area when designing the capacitor of the KID.

The T_c of common superconductors such as Al and TiN make KIDs feasible for millimeter and sub-millimeter wavelength observations. Several non-CMB millimeter and sub-millimeter wavelength experiments have deployed - or are currently developing - KIDs, such as SuperSpec (Shirokoff et al., 2012), NIKA2 (Adam et al., 2018), TolTEC (Austermann et al., 2018), and BLAST-TNG (Galitzki et al., 2014). There are multiple on-going developments toward feedhorn coupled multi-colour KID polarimeters for CMB experiments. To date, most designs have been based on OMT-coupled $\lambda/4$ CPW resonators using a novel optical coupling scheme, such as the devices proposed by Johnson et al. (2018). Resonators based on distributed resonators present a unique challenge, and are constrained by the competing requirements to both absorb the power along the length of the region of high-current density and not sacrifice noise and stability.

In this thesis I will discuss the development of a novel KID detector for CMB and other sub-mm astronomy observations.

CHAPTER 2

PHYSICS OF KINETIC INDUCTANCE DETECTOR

In this chapter, I will give an overview of the physics governing kinetic inductance detectors, namely the superconducting science, microwave circuitry, and characterization of a detector.

2.1 BCS Theory

Developed in 1957 (Bardeen et al., 1957), Bardeen–Cooper–Schrieffer (BCS) theory was one of the first theories to explain superconductivity at the microscopic level. The foundation of the theory stipulates that under the critical temperature T_c at which a material becomes a superconductor, the electrons in the metal close to the Fermi level condenses into particles called Cooper pairs. When an electron is moving through the crystal lattice of a superconductor, the lattice structure is drawn to the negative charge. The lattice distortion results in a net positive charge which then attracts another electron.

Unlike normal electrons, Cooper pairs act more like bosons and are not restricted by the Pauli exclusion principle to be at the same energy level. In a superconductor, these Cooper pairs can form into a Bose-Einstein condensate. At this ground energy state, there exists an energy gap, Δ, to upper energy states, which is typically on the order of a few milli-eV. This energy gap keeps the Cooper pairs from being affected by electron-phonon interactions which lead to resistance in a normal metal. In BCS theory, the relationship between Δ and T_c can be described as

$$2\Delta \approx 3.5 k_B T_c \tag{2.1}$$

One classic phenomenon of superconductivity is the Meissner effect. During the transition of a superconductor to below its critical temperature T_c, supercurrents form on the surface of the superconductor which cancels any magnetic field applied inside the superconductor. This expels any magnetic field from the bulk superconductor. In particular, we can define a characteristic scale for the decay of the magnetic field at the surface of the superconductor,

called the London penetration depth $\lambda_L = \sqrt{mc^2/4\pi n_s e^2}$, where m is the mass of an electron and n_s is the density of superconducting charge carriers (Cooper pairs). The magnetic field decays by a factor of e over the London penetration depth into the surface of the superconductor.

2.1.1 Two Fluid Model and Kinetic Inductance

Under the two fluid model developed by Gorter & Casimir (1934), at temperatures $0 < T < T_c$, there exists two types of charge carriers in the superconductors: Cooper pairs and "normal" electrons (or quasiparticles). In other words, there are two types of electron "fluids". One can think of the superconductor as having two parallel channels, a resistor (quasiparticles) and an inductor (Cooper pairs). For DC, the superconductor experiences no resistance since the resistive channel is shorted by the inductor. However, in the AC case, the superconductor gains a complex impedance. The energy stored in the inductor comes from the kinetic motion of the Cooper pairs, giving rise to an kinetic inductance.

In this model, the number density of the charge carriers n can be related to the number density of the quasiparticles n_{qp} and the number density of the superconducting charge carrier n_s as $n = n_{qp} + n_s$. The temperature dependency of n_s can be described as

$$\frac{n_s}{n} = 1 - \left(\frac{T}{T_c}\right)^4 \tag{2.2}$$

Figure 2.1 shows the temperature dependency of the above equation.

Although the two fluid model correctly predicts some behaviours of superconductors, it is not quite sophisticated enough to describe a KID. The sections below will describe a more encompassing theory of how a KID works at the microscopic level.

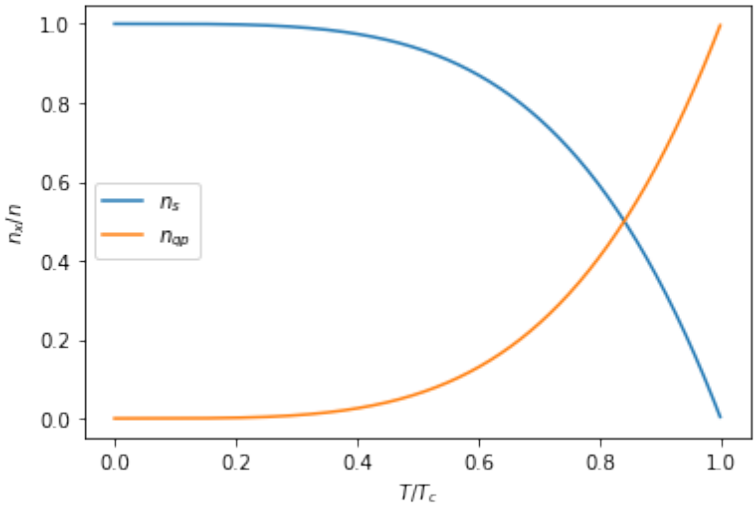

Figure 2.1: The fractional number density of quasiparticles n_{qp} and number density of superconducting charge carriers n_s to the total charge carrier number density n as described by the two-fluid model.

2.2 Mattis-Bardeen Theory

The following sections follow discussions from Zmuidzinas (2012), Gao (2008), and Mazin (2005). Please refer to those sources for a more detailed discussion.

The Mattis-Bardeen theory (Mattis & Bardeen, 1958) was first developed to explain the anomalous skin effect of superconductors. Under this framework, the complex conductivity, defined as $\sigma(\omega) = \sigma_1(\omega) - i\sigma_2(\omega)$, can be calculated. The normal-state conductivity is given by $\sigma_n = 1/\rho_n$. The ratios of the real and complex component of the conductivity to the normal conductivity are given by

$$\frac{\sigma_1}{\sigma_n} = \frac{2}{\hbar\omega}\int_{\Delta}^{\infty} dE \frac{E^2 + \Delta^2 + \hbar\omega E}{\sqrt{E^2 - \Delta^2}\sqrt{(E+\hbar\omega)^2 - \Delta^2}}[f(E) - f(E+\hbar\omega)] \tag{2.3}$$

$$\frac{\sigma_2}{\sigma_n} = \frac{1}{\hbar\omega}\int_{\Delta}^{\Delta+\hbar\omega} dE \frac{E^2 + \Delta^2 - \hbar\omega E}{\sqrt{E^2 - \Delta^2}\sqrt{\Delta^2 - (E-\hbar\omega)^2}}[1 - 2f(E)] \tag{2.4}$$

, where $f(E)$ is the distribution function for unpaired quasiparticles. For thermal equilibrium, this can be calculated as $f(E) = 1/(e^{E/k_BT} + 1)$.

The density of quasiparticles can then be defined as:

$$n_{qp} = 4N_0 \int_{\Delta}^{\infty} dE \frac{E}{E^2 - \Delta^2} f(E) \tag{2.5}$$

where N_0 is the single-spin density of electron states at the Fermi energy.

Let's consider the limit at low temperature ($k_B T \ll \Delta_0$) and frequency ($\hbar\omega \ll \Delta_0$), where $\Delta_0 = \Delta(0 \text{ Kelvin})$. By simplifying the integrals, equations 2.3, 2.4, and 2.5 can be approximated as:

$$\frac{\sigma_1}{\sigma_n} \approx \frac{4\Delta}{\hbar\omega} \exp\left(-\frac{\Delta_0}{k_B T}\right) K_0\left(\frac{\hbar\omega}{2k_B T}\right) \sinh\left(\frac{\hbar\omega}{2k_B T}\right) \tag{2.6}$$

$$\frac{\sigma_2}{\sigma_n} \approx \frac{\pi\Delta}{\hbar\omega}\left[1 - 2\exp\left(-\frac{\Delta_0 + \hbar\omega}{k_B T}\right) I_0\left(\frac{\hbar\omega}{2k_B T}\right)\right] \tag{2.7}$$

$$n_{qp} \approx 2N_0\sqrt{2\pi k_B T \Delta_0} \exp\left(\frac{-\Delta_0}{k_B T}\right) \tag{2.8}$$

where I_0 and K_0 are the modified Bessel functions of the first and second kind.

The conductivity quality factor can be defined as $Q_\sigma = \sigma_2/\sigma_1$ so using Equations 2.6 and 2.7, we find that

$$Q_\sigma \approx \frac{\pi}{4} \frac{e^{\Delta_0/k_B T}}{\sinh(\hbar\omega/2k_B T) K_0(\hbar\omega/2k_B T)} \tag{2.9}$$

Once the quasiparticles are generated, typically it will take a time of τ_{qp}, the quasiparticle lifetime, before they recombine back into a Cooper pair. An expression for τ_{qp} is given below (Kaplan et al., 1976)

$$\tau^{-1} = \frac{\sqrt{\pi}}{\tau_0}\left(\frac{2\Delta}{k_B T_c}\right)^{5/2}\left(\frac{T}{T_c}\right)^{1/2} e^{-\Delta/k_B T} \tag{2.10}$$

where τ_0 is a material-dependent parameter.

In 2012, Zmuidzinas (2012) proposed another form of τ_{qp} that was well-described by the data, which is as follows

$$\tau_{qp} = \frac{\tau_{max}}{1 + n_{qp}/n^*} \tag{2.11}$$

where τ_{max} is the experimentally observed maximum quasiparticle lifetime and n^* is the cross-over quasiparticle density and was found to be roughly $\sim 100\,\mu\text{m}^{-3}$.

In the case where most of the quasiparticles are from optical power rather than generated thermally, the above equation can be rewritten as

$$\tau_{qp} = \frac{\tau_{max}}{\sqrt{1 + \frac{2\Gamma\tau_{max}}{N^*}}} = \frac{\tau_{max}}{\sqrt{1 + \frac{2P_{opt}\eta_{pb}\tau_{max}}{\Delta n^* V_L}}} \tag{2.12}$$

where $N^* = n^* V_L$ (V_L is the volume of the inductor), $\Gamma = P_{opt}\eta_{pb}/\Delta$ is the generation rate, P_{opt} is the optical power and $\eta_{pb} \approx 0.57$ is the pair-breaking efficiency (Kozorezov et al., 2000).

2.2.1 Surface Impedance of Superconductors

Generally, we cannot measure the complex conductivity. However, this quantity can usually be derived from the complex surface impedance $Z_s = R_s + iX_s$, which can be measured (R_s is the surface resistance and X_s is the surface reactance). Nonetheless, this is not a straightforward task and in reality, we generally only consider specific cases, namely the local limit and the extreme anomalous limit for thick films, and the thin film limit.

Before we move onto the following sections, we need to provide some background regarding the characteristic lengths in superconductivity. Please refer to de Visser (2014) or Zmuidzinas (2012) as a reference.

Firstly, ξ_0 is the coherence length of the Cooper pairs, it can be thought of as the physical size of the Cooper pairs or the distance between the two electrons in a Cooper pair. ξ_0 can be calculated as $\xi_0 = \hbar v_f/\pi\Delta_0$, where v_f is the Fermi velocity of electrons. The other characteristic length in superconductivity is known as the penetration depth, λ, the scale of the decay of magnetic field at the surface of the superconductor, which has been alluded to in Section 2.1.

However, ξ_0 is only the coherence length of a pure material. The mean free path of a

superconductor's charge carrier can be defined as $l = \tau v_f$, where τ is the characteristic time between collisions of Cooper pairs with impurities in the material. Taking into account of this mean free path, we can define an effective coherence length ξ by

$$\frac{1}{\xi} = \frac{1}{\xi_0} + \frac{1}{l} \tag{2.13}$$

In superconductivity, the *clean* limit refers to when $l \gg \xi_0$, therefore $\xi \to \xi_0$. The *dirty* limit refers to when $l \ll \xi_0$, and therefore $\xi \to l$.

Local Limit

For the local limit, the penetration depth is long compared to the coherence length. The penetration depth can be calculated as $\lambda_{\text{local}} = \sqrt{\hbar/\pi\Delta\mu_0\sigma_n}$. In this scenario, $\lambda \gg \xi$, so the Cooper pair scale is much smaller than the scale of the effects of the magnetic field, therefore the response is *local*. This limit only holds when the superconductor thickness is much greater than the penetration depth.

We can relate the surface impedance to the conductivity by

$$Z_s = \sqrt{\frac{i\mu_0\omega}{\sigma}} \tag{2.14}$$

For small changes in temperature, we can see the variance in δZ_s will go as

$$\ln \delta Z_s \approx -\frac{1}{2} \ln \delta\omega \tag{2.15}$$

$$\frac{\delta Z_s}{Z_s} \approx -\frac{1}{2}\frac{\delta\sigma}{\sigma} \tag{2.16}$$

Extreme Anomalous Limit

In the extreme anomalous limit, the penetration depth is much less than the coherence length, meaning the Cooper pairs extend over distances much larger than the magnetic penetration

depth. Like the local limit, this only holds when the superconductor's thickness is much greater than the penetration depth. However, in this case $\lambda_{\text{anol}} = \lambda_{\text{local}}^{2/3}(\sqrt{3}l/2\pi)^{1/3}$.

Similarly to the local limit, we can calculate the surface impedance as

$$Z_s = i\mu_0\omega\lambda_{\text{anol}}\left(1 + \frac{i\delta\sigma}{\sigma_2}\right)^{-1/3} \tag{2.17}$$

Looking at small variations, we see that

$$\ln \delta Z_s \approx -\frac{1}{3}\delta \ln \sigma \tag{2.18}$$

and therefore

$$\frac{\delta Z_s}{Z_s} = -\frac{1}{3}\frac{\delta\sigma}{\sigma} \tag{2.19}$$

This is usually the case for Al, which make up the inductor of detectors described in Chapter 3 and 4.

Thin Film Limit

When the thickness of the superconductor, t, is much less than λ, the current distribution in the superconductor is essentially constant. The effective penetration depth is then $\lambda_{\text{thin}} = \lambda_{\text{local}}^2/t$. Then the surface conductivity can be calculated as

$$Z_s = i\mu_0\omega\lambda_{\text{thin}}\left(1 + \frac{i\delta\sigma}{\sigma_2}\right)^{-1} \tag{2.20}$$

and similarly to above, we see that

$$\ln \delta Z_s \approx -\delta \ln \sigma \tag{2.21}$$

$$\frac{\delta Z_s}{Z_s} = -\frac{\delta\sigma}{\sigma} \tag{2.22}$$

2.2.2 Fractional Frequency Shift with Temperature

From Equation 2.31 and Zmuidzinas (2012), we see that $\omega \sim L^{-1/2}$, therefore

$$\frac{\delta\omega(T)}{\omega_0} = -\frac{1}{2}\frac{\delta L}{L} = -\frac{\alpha\delta L_k(T)}{2L_k(0)} = -\frac{\alpha}{2}\left(\frac{L_k(T)}{L_k(0)} - 1\right) \tag{2.23}$$

where α is the fraction of the total inductance (L) that can be attributed to the kinetic inductance (L_k)

$$\alpha = \frac{L_k}{L} \tag{2.24}$$

Then considering $Z_s = i\omega L_s$, Equation 2.14 for the thick films in the local limit, and the fact $\sigma_2 \gg \sigma_1$ for superconductors,

We can rewrite Equation 2.23 as

$$\frac{\delta\omega(T)}{\omega_0} = -\frac{\alpha}{2}\left(\sqrt{\frac{\sigma_2(0)}{\sigma_2(T)}} - 1\right) = -\frac{\alpha}{2}\left(\sqrt{\frac{\sigma_2(0)/\sigma_n(0)}{\sigma_2(T)\sigma_n(T)}} - 1\right) \tag{2.25}$$

Now we can use Equation 2.7 and plugging in $T = 0$ for $\sigma_2(0)/\sigma_n(0)$, and work through the algebra to find that the frequency shift arising from quasiparticle dynamics can be described as

$$\frac{\delta\omega}{\omega_0} = \frac{\omega - \omega_0}{\omega_0} = -\frac{\alpha}{4}\left(\sqrt{\frac{2\pi k_B T}{\Delta}}e^{-\Delta/k_B T} + 2e^{-(\Delta/k_B T + \hbar\omega/2\pi k_B T)}\right) I_0\left(\frac{\hbar\omega}{2k_B T}\right) \tag{2.26}$$

Figure 2.2 shows the fractional frequency shift due to temperature variations for a sample resonator, along with the extrapolated fit parameters.

2.3 Microwave Circuitry

Since KIDs are typically designed to be in the microwave regime (∼few 100 MHz to ∼few GHz), it'll be useful to first establish common concepts and tools used in microwave engineering.

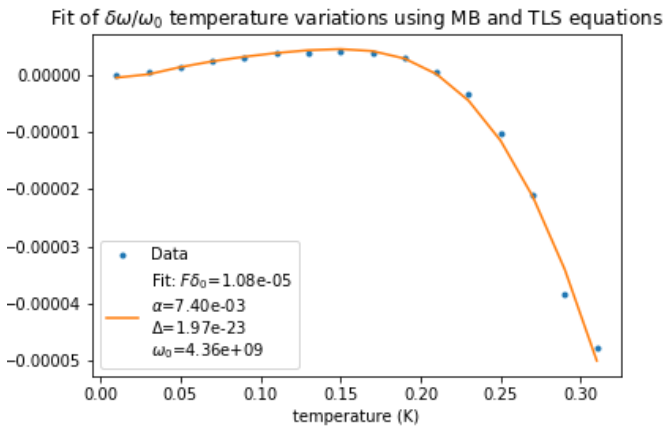

Figure 2.2: Fractional frequency shift with temperature variations. The fit parameters were extrapolated by fitting to Equation 2.26 and 2.55 (see Section 2.6.3 for a detailed discussion of Equation 2.55).

In a microwave circuit, many of the electrical components can be analyzed in terms of the scattering parameters or $S-$parameters. Let's look at the two-port case, which is typically the most common scenario, shown 2.3.

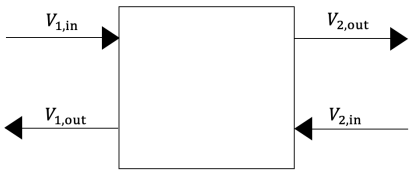

Figure 2.3: A schematic on the 2-port diagram.

We can describe the incident and reflective powers of the above system using the following scattering matrix

$$\begin{pmatrix} V_{1,\text{out}} \\ V_{2,\text{out}} \end{pmatrix} = \begin{bmatrix} S_{11} & S_{12} \\ S_{21} & S_{22} \end{bmatrix} \begin{pmatrix} V_{1,\text{in}} \\ V_{2,\text{in}} \end{pmatrix} \tag{2.27}$$

We can then define $S_{11} = V_{1,\text{out}}/V_{1,\text{in}}$ and $S_{21} = V_{2,\text{out}}/V_{1,\text{in}}$. These are typically referred to as the input port voltage reflection coefficient and the forward voltage gain respectively.

—S_{21}— is often simply referred as the *linear gain* of the system. We often works with *logarithmic gain* in units of decibels, which can be calculated as

$$g = 20 \log_{10} |S_{21}| \text{ dB} \tag{2.28}$$

noting that the factor of 2 comes from squaring the voltage for definition of power.

Similarly, we see that $S_{22} = V_{2,\text{out}}/V_{2,\text{in}}$ and $S_{12} = V_{1,\text{out}}/V_{2,\text{in}}$. These are typically referred to as the output port voltage reflection coefficient and the reverse voltage gain respectively.

The two-port system can also be easily extended to a 3-port system or higher.

I and Q

Any sinusoid can be constructed from two amplitude-modulated that are offset by a phase of $\pi/2$. As an example, we can see that

$$s(t) = A(t) \sin(2\pi f t + \phi(t)) = A(t) \cos[\phi(t)] \sin(2\pi f t) + A(t) \sin[\phi(t)] \cos(2\pi f t) \tag{2.29}$$

where we can take $I(t) = A(t) \cos[\phi(t)]$ and $Q(t) = A(t) \sin[\phi(t)]$. I is known as the *in-phase* component and Q is known as the *quadrature* component of the signal.

In microwave circuitry, where the signal is represented by $s(t) = A(t)e^{i(2\pi f t + \phi(t))}$, I represents the real part of the signal and Q represents the imaginary part. When we analyze S_{21} data (described in more detail in Section 2.4.1), the magnitude can be calculated as $|S_{21}| = \sqrt{I^2 + Q^2}$ and the phase as $\phi = \arctan(Q/I)$. Figure 2.4 shows the S_{21} of a resonator in I and Q coordinates and $|S_{21}|$ as a function of frequency.

2.4 Resonator Circuits

Let's look at an example of a parallel RLC circuit.

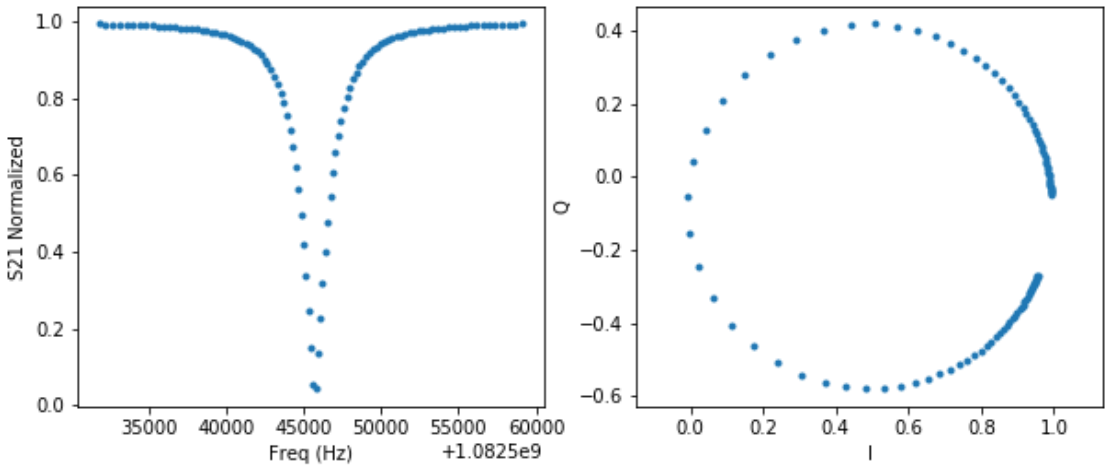

Figure 2.4: Left: Figure of $|S_{21}|$ of a resonator as a function of frequency. Right: I and Q plot of the same resonator. Note that the resonance occurs at the frequency where the IQ circle is closest to the origin.

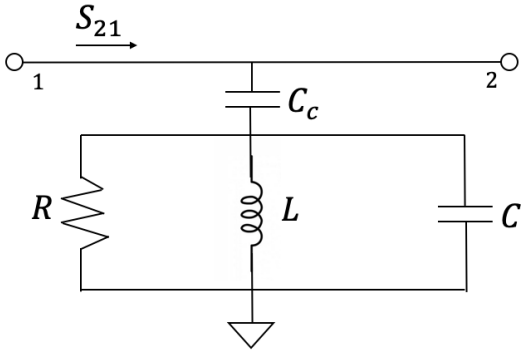

Figure 2.5: Circuit diagram of a parallel RLC resonance circuit. The resonator is capacitively coupled to a transmission line using a coupling capacitor C_c.

For a KID in normal operations, the resistance R is quite small. For the circuit above, the average energy stored in the inductor (W_m) and the average energy stored in the capacitor (W_e) can be calculated as

$$W_m = \frac{1}{4}L|I|^2 \quad \text{and} \quad W_e = \frac{1}{4}C|V|^2 \tag{2.30}$$

On resonance, there is an equal amount of energy stored in W_m and W_e. The resonance

frequency is given as

$$\omega_0 = \frac{1}{\sqrt{LC}} = \frac{1}{(L_g + L_k)C} \tag{2.31}$$

where L_g is the geometric inductance and $L = L_k + L_g$.

For a resonance circuit, we can quantify the quality factor as

$$Q = \omega_0 \frac{\text{energy stored in resonator}}{\text{power loss}} \tag{2.32}$$

Typically, Q refers to the total quality factor. We can further break up Q into the *intrinsic* quality factor Q_i, which encompasses loss arising from the film defects, dielectric, radiation, etc., and the *coupling* quality factor Q_c, which describes the energy leaking out of the capacitor coupling the resonator to the readout line. This relationship is given by

$$\frac{1}{Q} = \frac{1}{Q_i} + \frac{1}{Q_c} \tag{2.33}$$

Generally, Q_c can be set when designing the circuit by different capacitance values.

For a parallel RLC circuit, $Q_i = \omega_0 RC$, we can see that by considering that the energy stored in the resonator should be $W_m + W_e$ as described by Equation 2.30. Since on resonance, $W_m = W_e$, the total energy should be $2W_e = \frac{1}{2}C\langle V\rangle^2$, and the power dissipated should be $P = |V|^2/2R$. Therefore, according to Equation 2.32

$$Q_i = \omega_0 RC = \omega_0 Z_0 C/2 \tag{2.34}$$

where we use the fact $R = Z_0/2$ for parallel RLC circuits. We can also go through the same arguments considering the power dissipated being $P = |I|^2 R/2$ instead and find

$$Q_i = \omega_0 L/R \tag{2.35}$$

Considering the coupling quality factor, we can see that the power dissipated through

the coupling capacitance C_c can be described as (Barry, 2014)

$$P = \frac{|I|^2 R}{2} = \frac{|I|^2 Z_0}{4} = \left| \frac{V_c}{Z_{res}} \right|^2 \frac{Z_0}{4} = \frac{|V_c|^2 \omega_0^2 C_c^2 Z_0}{4} \tag{2.36}$$

where V_c is the peak voltage across the capacitor and $Z_{res} = 1/\omega_0 C_c$ is the resonator impedance. We need to modify Equation 2.30 for the maximal energy stored in the capacitor, which is $W_{e,max} = C|V|^2/2$, and plug all this into Equation 2.32 to arrive at

$$Q_c = \frac{2C}{\omega_0 Z_0 C_c^2} \tag{2.37}$$

2.4.1 S21 Equation

Following Pozar (2005), we can describe the two-port network in terms of voltages and current as an $ABCD$ matrix where

$$\begin{pmatrix} V_1 \\ I_1 \end{pmatrix} = \begin{bmatrix} A & B \\ C & D \end{bmatrix} \begin{pmatrix} V_2 \\ I_2 \end{pmatrix} \tag{2.38}$$

Relating the two representations of the two-port network, the S_{21} can be described in terms of the $ABCD$ matrix as

$$S_{21} = \frac{2}{A + B/Z_0 + CZ_0 + D} \tag{2.39}$$

In the case of the *shunt impedance* circuit, the values of the matrix are: $A = 1$, $B = 0$, $C = Y = 1/Z$, and $D = 1$, where $Z = R + iX$ (see Pozar (2005)). For MKIDs, we can define $Y = Y_L + Y_C = 1/i\omega L + i\omega C$. Plugging all this into Equation 2.39, we have

$$S_{21} = \frac{2}{2 + (1/i\omega L + \omega C)Z_0} = \frac{1}{1 + iQ_i(1 - (\omega_0/\omega)^2)} \tag{2.40}$$

where we use definitions from Equations 2.31 and 2.34.

The S_{21} equation above is for a simple parallel RLC circuit. A more detailed derivation pertaining to MKIDs can be found in Gao (2008), where the S_{21} equation can be described as

$$S_{21} = 1 - \frac{Q/Q_c}{1 + 2iQx} \tag{2.41}$$

where $x = \delta\omega/\omega_0 = (\omega - \omega_0)/\omega_0$.

Thus, we see that at FWHM of the resonance, $Q = \pm\frac{1}{2}\delta\omega$ so $\Delta\omega_{\mathrm{FWHM}} = \omega_0/Q$.

Impedance mismatching

The S_{21} equation derived above assumes perfect impedance matching (50Ω in standard microwave circuitry). However, there usually exists a small amount of impedance mismatching which causes some degree of reflection in the transmission lines. This distorts the resonance from a perfect Lorentzian shape and the S_{21} equation needs to be modified to account for this.

A more complete version of the S_{21} which accounts for this term is given below:

$$S_{21} = \frac{Q_c + iQ_cQ_i\left(2x + \frac{2\delta\omega_{\mathrm{asym}}}{\omega_0}\right)}{(Q_i + Q_c) + 2iQ_cQ_ix} = 1 - \frac{\tilde{Q}/\tilde{Q}_c}{1 + 2i\tilde{Q}x} \tag{2.42}$$

where $\delta\omega_{\mathrm{asym}}$ is a parameter we need to fit for that accounts for the asymmetry, $x = (\omega - (\omega_0 + \delta\omega_{\mathrm{asym}}))/(\omega_0 + \delta\omega_{\mathrm{asym}})$, and $\tilde{Q}$ and $\tilde{Q}_c$ are the complex version of Q and Q_c. The second equality in Equation 2.42 is to recognize that instead of adding the parameter $\delta\omega$ into S_{21}, the asymmetry can also be accounted for by making Q_c (and therefore Q) complex. Therefore, the two are related by $1/Q_c = \mathrm{Re}(1/\tilde{Q}_c)$ and $\delta\omega_{\mathrm{asym}} \sim \mathrm{Im}(1/\tilde{Q}_c)$.

Please see Geerlings (2013) for a full derivation of Equation 2.42. Figure 2.6 shows a sample resonator with fit using Equation 2.42.

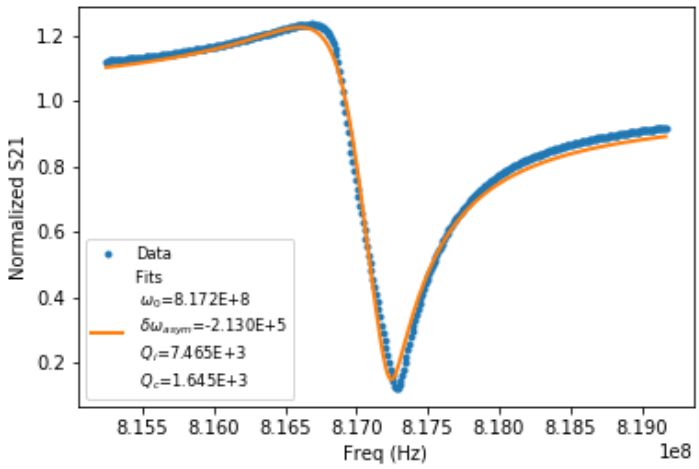

Figure 2.6: A S_{21} plot of a sample resonator data in blue dots and the corresponding fit in orange line.

2.5 Responsivity

In the case that the only the kinetic inductance is modified by a change in n_{qp} , we can see that (Gao, 2008) by following Equation 2.23, we can derive

$$\frac{\delta\omega}{\omega_0} = -\frac{\alpha\delta L_k}{2L_k} = -\frac{\alpha\delta X_s}{2X_s} \tag{2.43}$$

and similarly with Equation 2.35,

$$\delta Q_i^{-1} = \frac{\delta R}{\omega_0 L} = \alpha\frac{\delta R_s}{X_s} \tag{2.44}$$

From Zmuidzinas (2012), we can use the two above equations along with the Mattis Bardeen conductivity response functions (Equations 2.6 and 2.7) to derive a relationship between the change in resonance frequency ($\delta x = \delta\omega/\omega_0$) with a change in number of quasiparticles (δN_{qp})

$$\frac{\delta x}{\delta N_{qp}} = \frac{\alpha\gamma}{4N_0\Delta_0 V_L}\left(1 + \sqrt{\frac{2\Delta_0}{\pi k_B T}}\exp\left(-\frac{\hbar\omega}{2k_B T}\right) I_0\left(\frac{\hbar\omega}{2k_B T}\right)\right) \tag{2.45}$$

where $\gamma = 1, 1/2, 1/3$ for the thin-film, local, and extreme anomalous limit (see Section 2.2.1).

Similarly for a change in Q_i,

$$\frac{\delta Q_i^{-1}}{\delta N_{qp}} = \frac{2\alpha\gamma}{4N_0\Delta_0 V_L}\frac{2}{\pi}\sqrt{\frac{2\Delta_0}{\pi k_B T}}\sinh\left(\frac{\hbar\omega}{2k_B T}\right)K_0\left(\frac{\hbar\omega}{2k_B T}\right) \tag{2.46}$$

Considering that $N_{qp} = n_{qp}V_L$ and $\delta n_{qp}/\delta P_{opt} = \eta_{pb}\tau_{qp}/\Delta V_L \approx \eta_{pb}\tau_{qp}/\Delta_0 V_L$, we can see that (Barry, 2014)

$$\frac{\delta x}{\delta P_{opt}} = \frac{\alpha\gamma\eta_{pb}\tau_{qp}}{4N_0\Delta_0^2 V_L}\left(1 + \sqrt{\frac{2\Delta_0}{\pi k_B T}}\exp\left(-\frac{\hbar\omega}{2k_B T}\right)I_0\left(\frac{\hbar\omega}{2k_B T}\right)\right) \tag{2.47}$$

and

$$\frac{\delta Q_i^{-1}}{\delta P_{opt}} = \frac{2\alpha\gamma\eta_{pb}\tau_{qp}}{4N_0\Delta_0^2 V_L}\frac{2}{\pi}\sqrt{\frac{2\Delta_0}{\pi k_B T}}\sinh\left(\frac{\hbar\omega}{2k_B T}\right)K_0\left(\frac{\hbar\omega}{2k_B T}\right) \tag{2.48}$$

We can substitute in τ_{qp} from Equation 2.12 to have the full equations.

Figure 2.7 shows the S_{21} curve of a resonator with and without optical power absorbed.

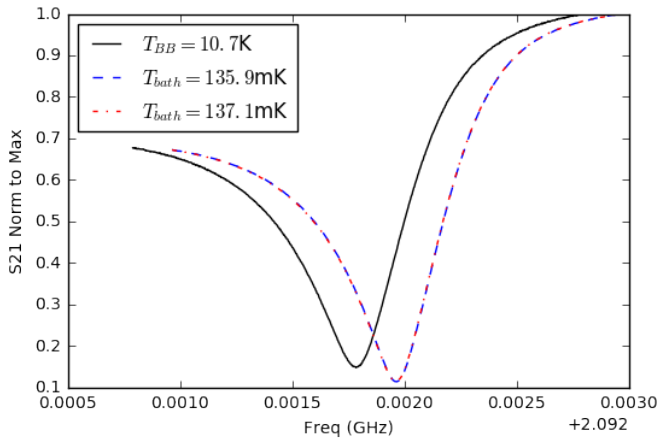

Figure 2.7: S_{21} of a resonator at $\sim$ 136 mK in a dark environment (blue and red dashed curves) and an optical environment with a 10 K blackbody (solid black curve). Note the resonance shift and the degradation in Q (shallower and wider resonance dip).

2.6 Noise

2.6.1 Fundamental g-r Noise

The most fundamental source of noise comes from the generation and recombination (g-r) of quasiparticles and Cooper pairs in the MKID.

Quasiparticles are generated in pair, where a photon with energy $E > 2\Delta$ breaks a Cooper pair. Phonons in the substrate with energy $E > 2\Delta$ can similarly break Cooper pairs.

Once the quasiparticles are generated, they have a finite lifetime before recombining back into a Cooper pair, and in the process emitting a phonon of energy $E > 2\Delta$. The quasiparticle lifetime τ_{qp} is typically on the timescale of $10^{-3} - 10^{-6}$ second.

The sensitivity of photodetectors is often characterized by its noise equivalent power (NEP), which is defined as the signal power that gives a signal-to-noise ratio of one in a 1 Hz output bandwidth. The g-r NEP of MKIDs is given as

$$\mathrm{NEP}_{gr} = \frac{2\Delta}{\eta_{pb}} \sqrt{\frac{N_{qp}}{\tau_{qp}}} \propto \exp\left(-\Delta/k_B T\right) \tag{2.49}$$

η_{pb} is the pair-breaking efficiency. Evidently, decreasing the operating temperature can drastically decrease the g-r noise.

We can express the noise power spectral density (PSD) from generation-recombination by de Visser (2014); Baselmans (2012)

$$S_{g-r} = \frac{4N_{qp}\tau_{qp}}{1 + (\omega\tau_{qp})^2} \left[\frac{\delta\theta}{\delta N_{qp}}\right]^2 \tag{2.50}$$

where $\delta\theta/\delta N_{qp}$ describes the phase change per quasiparticle.

2.6.2 Photon Noise

Typically we want to design detectors that are photon-noise dominated. For observing in the far-infrared/sub-mm wavelengths, this means the sensitivity is limited by the random arrival rate of photons.

We can calculate the NEP for light absorbed with power P and frequency ν_0 with bandwidth $\Delta\nu$ as

$$NEP_\gamma^2 = \int 2h\nu P(\nu)d\nu + \int [P(\nu)]^2 d\nu \approx 2h\nu_0 P + P^2/\Delta\nu = 2h\nu_0 P(1+\bar{n}) \tag{2.51}$$

where the first term corresponds to Poisson noise or photon shot noise, the second term corresponds to the "Bose" or "bunching" noise, and $\bar{n}$ is the average photon occupation number.

The absorbed power generates a number of quasiparticles described as (Baselmans, 2012)

$$N_{qp} = \frac{P\tau_{qp}}{\eta_{pb}\Delta} \tag{2.52}$$

2.6.3 Two-Level System Noise

One source of noise for MKIDs that has not yet been fully understood is the two-level system (TLS) noise. TLS noise comes from quantum tunnelling between local minima of the potential energy on the surface of the detector, which couples to the electric field and affecting the capacitance, and therefore ω_0, of the KID.

Currently, TLS noise is still not very well characterized or understood. Empirically, it has been demonstrated (Gao, 2008) that the spectral shape of TLS has the following dependencies:

$$S \propto f^{-1/2} P_{\mathrm{ro}}^{-1/2} T^{-2} \frac{\int |E|^3 d^3r}{(\int |\epsilon E|^2 d^3r)^2} \tag{2.53}$$

So the TLS noise is dominant at lower frequencies, more prominent with low readout power

and temperatures, and high electric field in the region contributing to TLS noise.

One way to get minimize the TLS noise contribution is by increasing the capacitor geometry of the KID such that the electric fields coupling exist mainly outside the TLS region of the detector.

Loss from TLS

Following Zmuidzinas (2012), the TLS loss can be characterized by the moving (tunneling) atoms carrying a dipole, which effectively modifies the dielectric constant ϵ. Therefore, the loss tangent can be described as

$$\delta_{\mathrm{TLS}} = \frac{\mathrm{Im}\ \epsilon_{\mathrm{TLS}}}{\mathrm{Re}\ \epsilon} = \delta_0 \tanh\left(\frac{\hbar\omega}{2k_BT}\right) \tag{2.54}$$

where δ_0 is the TLS loss in limit where $k_BT \ll \hbar\omega$ and TLS only occupies the potential ground state.

As outlined in Zmuidzinas (2012), we can describe the frequency shift as

$$\frac{\delta\omega}{\omega_0} = -\frac{F_{\mathrm{TLS}}}{2}\frac{\mathrm{Re}\ \epsilon_{\mathrm{TLS}}}{\mathrm{Re}\ \epsilon} = \frac{F_{\mathrm{TLS}}\delta_0}{\pi}\left[\mathrm{Re}\ \Psi\left(\frac{1}{2} + \frac{\hbar\omega}{2\pi i k_BT}\right) - \ln\frac{\hbar\omega}{k_BT}\right] \tag{2.55}$$

where F_{TLS} is the filling factor that describes the fraction of the electric energy stored in the TLS-affected material and Ψ is the complex digamma function.

Translated into quality factor, we see that

$$\frac{1}{Q_{i,\mathrm{TLS}}} = F_{\mathrm{TLS}}\delta_{\mathrm{TLS}} = F_{\mathrm{TLS}}\delta_0 \tanh\left(\frac{\hbar\omega}{2k_BT}\right) \tag{2.56}$$

2.6.4 Other Noise Sources

Noise from the readout chain is typically dominated by the first stage cryogenic amplifier. From Barry (2014), we see that we can calculate what the spectrum of the amplifier noise

using the following equation:

$$S_{xx} = 4k_B T_a R \frac{Q_c^2}{4Q^4 V_{in}^2} \tag{2.57}$$

where T_a is the temperature of the amplifier, R is the effective resistance of the amplifier, and $V_{in} = V_{out}/S_{21}$.

A derivation of the amplifier NEP can be found in Zmuidzinas (2012). The result is summarized as

$$NEP_{\text{amp}}^2 = \frac{8N_{qp}^2 \Delta_0^2 k_B T_a}{\eta_{pb}^2 \chi_c \chi_{qp}^2 \tau_{qp}^2 P_a} \tag{2.58}$$

where $\chi_c = 4Q_c Q_i/(Q_c + Q_i)^2$ is the coupling efficiency factor and $\chi_{qp} = Q_i/Q_{qp}$ is the fraction of resonator's internal loss is contributed by quasiparticles.

2.6.5 Noise Analysis

This section will briefly go over how noise analysis is done on KIDs. Please refer to Appendix E in Gao (2008) for a more complete overview on analyzing resonator data. For information on the measurement setup used for data taking, please refer to Section 3.4

For general noise analysis, typically four sets of data are taken. First, low-resolution resonator sweep is taken that is sufficiently wide to capture the off-resonance frequency points on either side of the resonance, and the resonance frequency is calculated. Second, a high-resolution resonator sweep is taken centred on the resonance frequency. Third, the synthesizer feeds in a tone at the resonance frequency, and time stream data is taken and the same thing is repeated for an off-resonance frequency. All the components needed for noise analysis of a sample resonator is plotted in Figure 2.8.

To analyze this data, we must first remove the cable delay. Indeed, the transmission curve can be modelled by modifying the S_{21} in Equation 2.42 to be

$$t(f) = ae^{-2\pi i f \tau} S_{21} \tag{2.59}$$

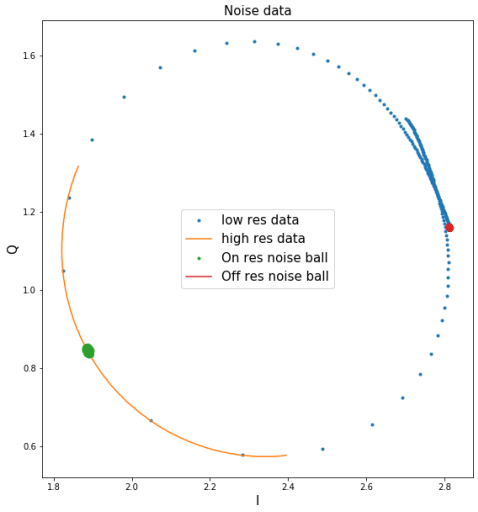

Figure 2.8: IQ plot of the raw data taken for noise analysis. First, a low resolution sweep is done to capture both the resonance and the off-resonance data. A high resolution sweep is done specifically at the dip of the resonance. Then time-stream data is taken where the tone is set to the resonance frequency and an off-resonance frequency. The time-stream data manifests itself as a "noise ball" in the IQ plane.

where a is a complex constant account for the phase and gain through the cabling and τ accounts for the delay associated with the length of the cables.

We isolate the off-resonance portion of the low resolution data and fit the phase of that data to $-2\pi f\tau$ to extract τ. Then we multiply the data by $\exp(2\pi i f\tau)$ to correct the cable delay, this reduces off-resonance portion of the data to stationary points, as seen in Figure 2.9.

Once the cable delay is removed, we can switch to using just the high resolution sweep data. The resonance data can be fitted as a circle using $z_c = x_c + iy_c$ with an angle rotation $\alpha = \arg(z_c)$. Ultimately we will use the shift in phase of the noise ball to estimate the shift in frequency. Therefore we want to line up the data such that on resonance lines up with the I axis ($\theta = 0$). To do this, we modify the data with the cable delay removed t_{cr} by a rotation and translation such that the IQ circle is centred at origin with the on-resonance

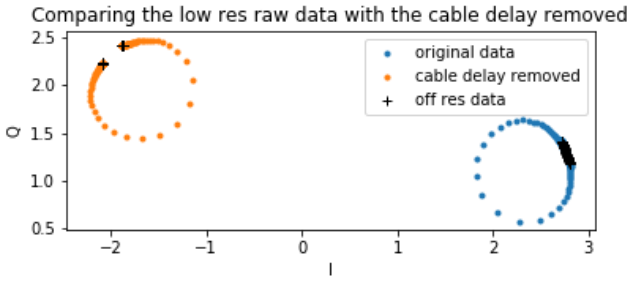

Figure 2.9: Plot showing the IQ resonator data before and after cable delay. Notice that all the off-resonance points condensed into a single point on either side of the resonance after cable delay.

point lying along the I-axis. This can be done by using the following equation

$$t_{ct} = (z_c - t_{cr})e^{i\alpha} \tag{2.60}$$

Figure 2.10 shows what the high resolution sweep data looks like after rotation and translation. Notice that the data lines up perfectly with a circle that's centred at the origin in the IQ plane.

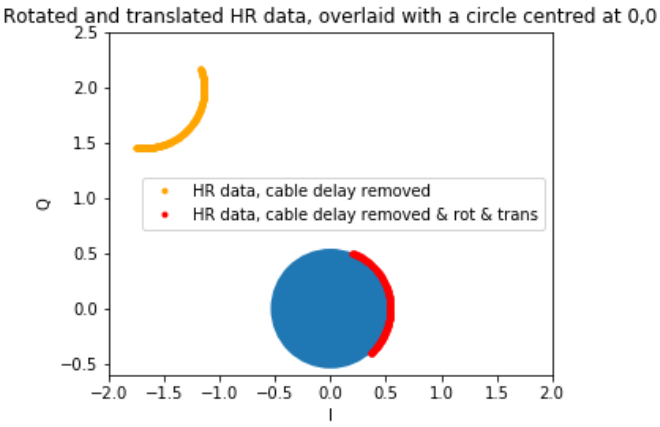

Figure 2.10: Plot showing the high resolution IQ sweep before and after the rotation and translation. A circle centred at the origin is drawn to show that the data after the transformation aligns perfectly with the circle, the on-resonance portion lined up in the direction of the I-axis.

Last step to do before we consider the time-stream data is fitting for a relationship between the phase and the frequency of the IQ data. This can be done using

$$\theta = -\theta_0 + 2\arctan\left(2Q_r\left(1 - \frac{f_r}{f}\right)\right) \tag{2.61}$$

and θ_0, Q_r, and f_r can be extracted from the fit. Figure 2.11 shows the frequency to phase fitting of a sample resonator high resolution IQ sweep.

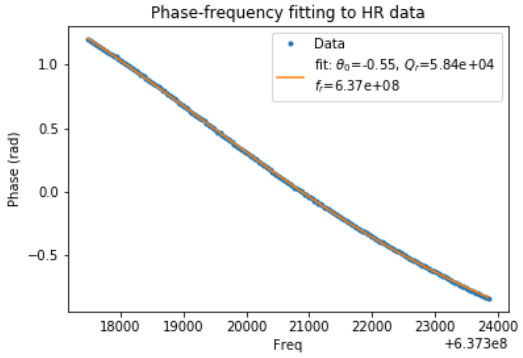

Figure 2.11: Frequency to phase fitting for a sample high resolution IQ sweep data, with fit parameters.

Once we extrapolated all the parameters for the different steps, we can apply the same transformations to the time-stream data as the IQ sweeps, namely: removing the cable delay, rotating and translating the data, and converting the IQ data to frequency using the phase-frequency relationship. The last step is to construct the noise PSD of the time-stream, which can be done using

$$PSD = S_{xx}\ [\mathrm{Hz}^{-1}] = \frac{|FFT(f)|^2}{N f_s f_0^2} \tag{2.62}$$

where f is the time-stream data translated into frequency, N is the number of points in the data, f_s is the sampling rate of the time-stream, and f_0 is the frequency of the tone sent by the synthesizer in generating the time-stream.

Although noise analysis is relatively straightforward, precaution must be taken to make optimal measurements. For example, random cosmic ray hits can deposit energy onto the detectors causing a spike in the time-stream. Vibration from the pulse-tube can also induce

periodic patterns in the time-streams. It is recommended to take several time-streams and do an initial preliminary quality check to flag any problematic data. We can also average noise PSDs from several time-streams to reduce the scatter.

Following McGeehan et al. (2018), we can fit the fractional frequency noise PSD in the functional form

$$S_{xx}(f) = \left(\frac{A + Bf^{-n}}{1 + (2\pi f\tau)^2} + C \right) \frac{1}{1 + (2\pi f\tau_{filt})^2} \tag{2.63}$$

where A is the resonator white noise level associated with the g-r noise, $Bf^{-}n$ fits the low frequency roll-off (where n is often found to be 0.5 due to TLS noise), τ is the quasiparticle lifetime extracted from the roll-off frequency of the resonator white noise level, and C and τ_{filt} are terms associated with the amplifier white noise level and the anti-aliasing filter roll-off.

An example of the final noise PSD and its fit is shown in Figure 2.12.

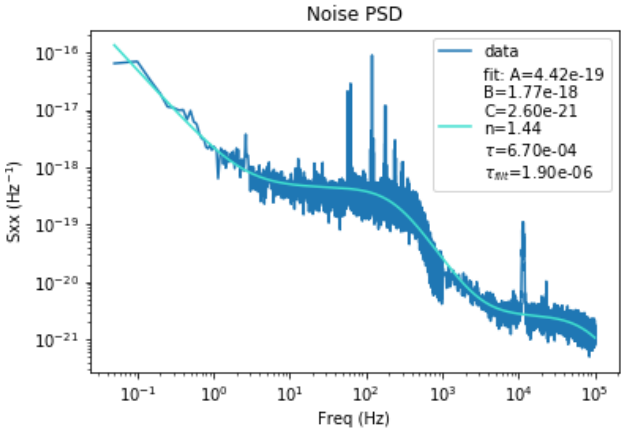

Figure 2.12: Noise PSD of a sample resonator, along with fit to Equation 2.63.

We can convert the noise PSD to NEP using the following equation as outlined in Baselmans et al. (2008)

$$NEP^2 = S_{xx} \left[\frac{\eta_{pb}\tau}{\Delta} \frac{\delta\theta}{\delta N_{qp}} \right]^{-2} (1 + \omega^2\tau^2)(1 + \omega^2\tau_{res}^2) \tag{2.64}$$

where $\tau_{res} = Q/\pi f_0$ is the ring-down time of the resonator, and we can obtain τ from the

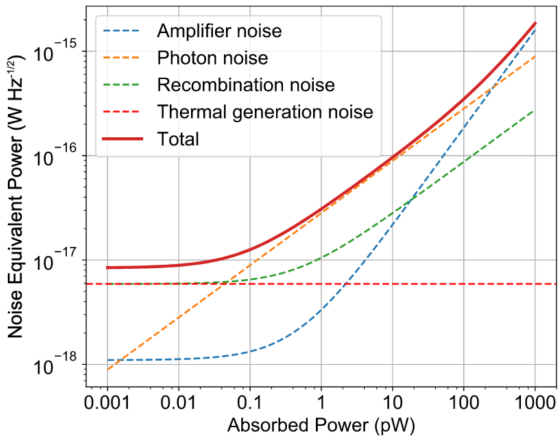

Figure 2.13: Varying noise contributions to the detector. Taken with permission from Barry et al. (2018).

fit of Equation 2.63.

Figure 2.13 shows the expected noise contribution from various sources when considering an optical load for a detector with volume of 4800 μm^3. This model calculates the number of quasiparticles generated both optically and thermally, considering the detector at an ambient temperature of $T_b = 230$ mK, and it shows the detector is expected to be photon noise dominated at an optical loading of 1 to 10 pW, which is typical of most ground-based CMB experiments. The device described in this figure is the main subject of Chapter 3.

2.7 MKID Designs

2.7.1 CPW Resonator

The very first MKIDs developed were done using the co-planar waveguide (CPW) design Day et al. (2003). Two slots are cut into the ground plane to form a centre line. The shape of the CPW resonator is often designed as a "hanger" resonator where there is a bend close to the readout line, and a portion of the resonator lies parallel to the readout line, which sets the coupling capacitance. In the quarter-wavelength ($\lambda/4$) resonators, the end farther from the feedline is shorted to ground and the other end is open. Half-wavelength resonators

can also be designed where both ends of the CPW line are open. Please see Figure 2.14 for a diagram of a CPW resonator.

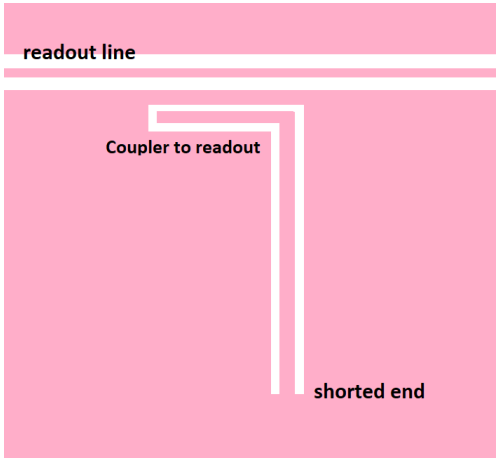

Figure 2.14: Diagram of a $\lambda/4$-resonator.

One obvious drawback to the CPW resonators is the current density is highly nonuniform across the resonator. In $\lambda/4$-resonators, current density is the highest at the shorted end of the line. Thus, it is impractical to design CPW resonators as a direct absorbers. They are usually coupled to another photon-sensing element, e.g. antennae or OMT probes, via a microstrip with a quasiparticle trapping mechanism.

2.7.2 Lumped-Element KIDs

Lumped-element KIDs (LEKIDs) were first developed in 2007 by Doyle et al. (2008). In this configuration, the capacitor and inductor element of the MKIDs are physically separated out. Generally, the capacitor is designed as a series of interdigited capacitor (IDC) fingers and the inductor as a long meander. By configuring the inductor geometry and film properties and adding a backshort, the LEKID can be designed as a direct photon absorber, as seen by Adam et al. (2018). Please see Figure 2.15 for a diagram of a LEKID resonator.

Compared to the CPW resonators, the LEKID inductor has a more uniform current distribution and sensitivity. In general, controlling the different design parameters is much easier with LEKIDs than CPW. For example, we can keep the inductor identical across

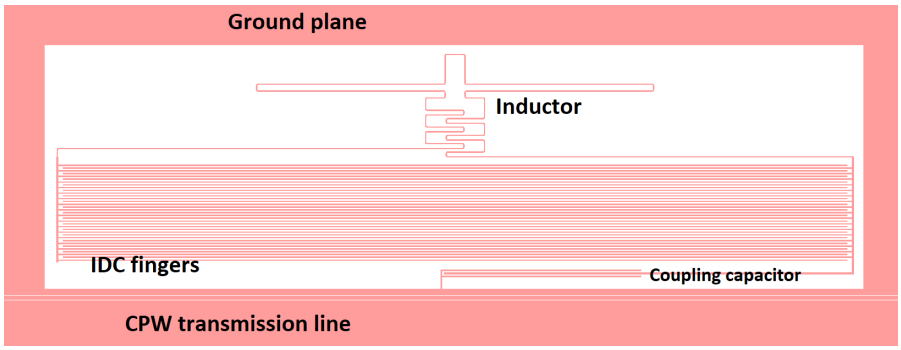

Figure 2.15: Diagram of a LEKID resonator. Note that the inductor is a long meander and capacitor is a series of IDC fingers.

multiple pixels by simply adjusting the capacitor geometry. However, since KIDs are typically designed in the $\sim$ GHz range, LEKIDs need tend to occupy a much larger footprint on the detector wafer than CPW resonators.

CHAPTER 3

ANTENNA-COUPLED KIDS FOR CMB DETECTION

This chapter describes the work that was published in Tang et al. (2018) and Barry et al. (2018).

In this chapter, we describe the work done to develop an antenna-coupled MKID prototype array in the 150 GHz band optimized for CMB detection. This design uses a twin slot antenna coupled to inverted Nb/SiN_x/Nb microstrip, which is then coupled to an Al/Nb KID grown on high resistivity Si.

3.1 Introduction

In the last few decades, studies of the CMB have made tremendous contributions to our understanding of the cosmological universe. Nonetheless, there still remain many science goals for CMB observers. Future space and ground-based CMB experiments will require a substantial increase in the number of detectors to reach the target sensitivity due to the detectors being photon noise dominated. For example, CMB-Stage 4 (S4) collaboration is the next generation CMB experiment and will consist of a collaboration of telescopes at the South Pole and Atacama plateau in Chile. To reach the target sensitivity, the number of detectors will increase from $O(10,000)$ of current CMB experiments to $O(500,000)$ (Abazajian et al., 2016). Although the conventional transition edge sensor (TES) bolometers are well-understood and characterized, they face several challenges in scaling up for these future missions, especially with regards to complicated fabrication process, which requires precise control, and difficulty in multiplexing, due to the readout electronics needed.

Kinetic inductance detectors (KIDs) are an alternative technology that offers simple designs and intrinsic multiplexing capabilities. With these advantages, KIDs present a feasible solution for the next generation CMB experiments. Several non-CMB millimeter and submillimeter wavelength experiments have deployed, or are currently developing, KIDs, such

as SuperSpec (Shirokoff et al., 2012), NIKA (Adam et al., 2018), and MAKO (Swenson et al., 2012). Current developments in KID arrays for CMB experiments employ horn-coupled lumped element KIDs (LEKIDs) and $\lambda/4$ CPW resonators as seen in McCarrick et al. (2018) and Johnson et al. (2018). In this chapter, we present the design, fabrication process, and initial testing of an antenna-coupled LEKID array for CMB detection.

3.2 Design

The preliminary design of antenna-coupled KIDs for CMB detection uses dual-slot antennas, sensitive to the a single polarizations. Figure 3.1 depicts a schematic of the detectors. The dimensions of the antenna slots were chosen to have a well-defined beam (half angle $\approx 15^{\circ}$) at 150 GHz. We couple the antenna to an inverted microstrip transmission line. The microstrip consists of a bottom Nb layer, which forms the microstrip, a top layer of Nb as the ground plane, and a layer of silicon nitride (SiN_x) in between as the dielectric. The reason for the inverted structure is because this allows for the film of the detector to be deposited onto a clean crystalline silicon surface, which is the most critical layer processing in the fabrication process. The microstrip carries the mm-wave signal from the antenna to our detectors, which are Nb/Al LEKIDs, comprising a discrete inductive meander and interdigitated capacitor (IDC), refer to Section 2.7 for more detail. The Al KIDs are coupled capacitively to a co-planar waveguide (CPW) transmission line for readout, made in the same bottom Nb layer of the microstrip. For details regarding antenna and detector design, refer to Barry et al. (2018), but we will briefly summarize the main components of the design below.

3.2.1 Millimetre-Wave Coupling

This design utilizes a novel yet simple method to couple the mm-wave signal from the microstrip to the KID. Our microstrip has a line width of 4 µm, which was chosen to balance radiation loss (from larger lines) and lithography limitations and has a 500 nm thick layer

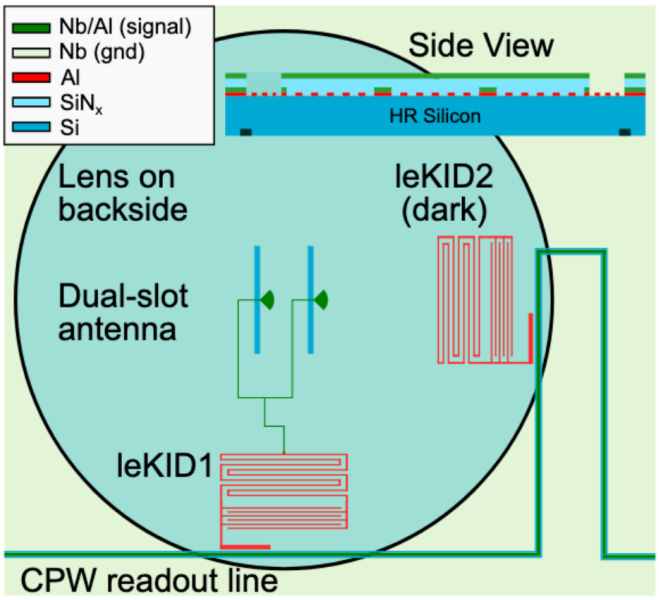

Figure 3.1: Design layout of the antenna-coupled KID for CMB detection. Dual-slot antenna is coupled to a Nb microstrip line, which feeds the signal to LEKIDs. As a test structure, a "dark" KID was incorporated in the design to measure any photon detection via ways other than the antenna-microstrip structure. Taken with permission from Barry et al. (2018).

of SiN ($\epsilon_r = 7$). From Pozar (2005), the characteristic impedance of a microstrip line when the microstrip linewidth is much larger than the thickness of the dielectric ($W \gg d$) can be found using the approximation

$$Z_0 = \frac{120\pi}{\sqrt{\epsilon_e}[W/d + 1.393 + 0.667\ln(W/d + 1.444)]} \tag{3.1}$$

where ϵ_e is the effective dielectric constant of a microstrip, which can be calculated as

$$\epsilon_e = \frac{\epsilon_r + 1}{2} + \frac{\epsilon - 1}{2}\frac{1}{\sqrt{1 + 12d/W}} \tag{3.2}$$

where ϵ_r is the relative dielectric constant. Alternatively, the characteristic impedance can also be found more accurately via Sonnet simulations, which gives $Z_0 = 17.6\Omega$ for our microstrip.

The two microstrip lines are combined into a single 8 µm thick microstrip line. The increase in line width is to allow for impedance matching to the two thinner microstrip lines.

The thick microstrip terminates at a junction which has galvanic contact to the Al inductor. The position of the junction is chosen to be at a voltage null of the inductor, corresponding to the middle of the inductor meander. In our design, the ground plane does not terminate at the junction but extends out further into the Al inductor along with the dielectric layer. This way, we can also treat the Al inductor as a lossy microstrip since the bandgap energy is lower than the mm-wave signal. The attenuation from conductor loss can be given by (Pozar, 2005)

$$\alpha_c = \frac{R_s}{Z_0 W} \text{ Np/m} \approx 8.686 \frac{R_s}{Z_0 W} \text{ dB/m} \tag{3.3}$$

where $R_s = \sqrt{\omega \mu_0 / 2\sigma}$ is the surface resistivity of the conductor.

For our design, since the power is dissipated via two diverging paths, we can calculate the attenuation as $\alpha_c/2$. To ensure that any quasiparticles generated from the light signal stays within the inductor, we design the length of the Al inductor microstrip to be sufficiently long for all the mm-wave power to be dissipated along its length. Our Al inductors have a film thickness of 50 nm and has a surface resistivity of $R_s \approx 0.2\Omega$/sq, linewidth of 4 µm, and characteristic impedance of 17.6 Ω. Plugging this into the above, we estimate $\alpha_c \approx 12.3$ dB/mm *for both ends of the inductor meander*. Our final design incorporates a 3 mm length for the Al inductor to act as a lossy microstrip from the mm-wave junction. The ground plane and the dielectric layer is removed from the Al inductor after the 3 mm length.

Lastly, we verify the reflection at the microstrip-to-inductor inductor is sufficiently low. Sonnet simulations showed the S_{11} response of a signal sent down the microstrip is less than -20 dB across a bandwidth of 100-350 GHz, which corresponds to less than 1% of reflected power.

3.2.2 Prototype Array

The KIDs are designed to have a resonance frequency in the range of 500-1100 MHz. The inductor meander is made out of Al and the IDC fingers are made out of Nb. As described

above, the ground plane extends out to partially cover the Al inductors in order for the Al to act as a lossy microstrip. The SiN dielectric layer siting above the IDC fingers is removed to avoid dielectric loss affecting the KID.

The initial prototype array is a 7-pixel device. A layout of the array is shown in Figure 3.2. Under each lenslet, there are two KIDs. The optical KID is connected to the antenna sitting directly underneath the lenslet via the Nb/SiN/N microstrip. The "dark" KID is not connected to a microstrip and is simply capacitively coupled to the CPW readout line and sits at an equal distance to the antenna. Six out of the seven antennae are orientated in the same direction. The last antenna is orientated to be sensitive to the orthogonal polarization to the rest. Several test resonators are designed to diagnose the chip. There are two dark KIDs that are not located underneath any lenslets but have the same geometry as the KIDs sitting underneath the lenslet. Two additional dark KIDs are placed away from the lenslets that have similar geometry as the other KIDs but with the SiN layer unetched to cover the whole KID to study how much dielectric loss affects the resonator. Lastly there is a dark KID made entirely out of Al that is completely uncovered by neither the ground plane nor SiN layer. In total there are 21 KIDs on the prototype array.

To allow for easy identification of the resonators, the resonances are placed in distinct "bands". Within each resonator bank, the resonances have identical inductor geometry. Instead, the IDC finger lengths are slightly modified for each resonator in a given band, which gives ∼few MHz of separation between the resonators in each bank. Refer to Table 3.1 for more information on the design parameters.

The antenna design uses dual-slot antenna, which consists of a pair of long rectangles cut into the ground plane. An optical microscope image of the antenna can be seen in Figure 4.1. For dual-slot antenna, the polarization sensitivity is orientated along the length of the slot. A microstrip feedline connects to the antenna at the centre of the slot, where a voltage source is applied. The microstrip is terminated at the antenna by using radial stubs, which acts as a high-pass filter to ground.

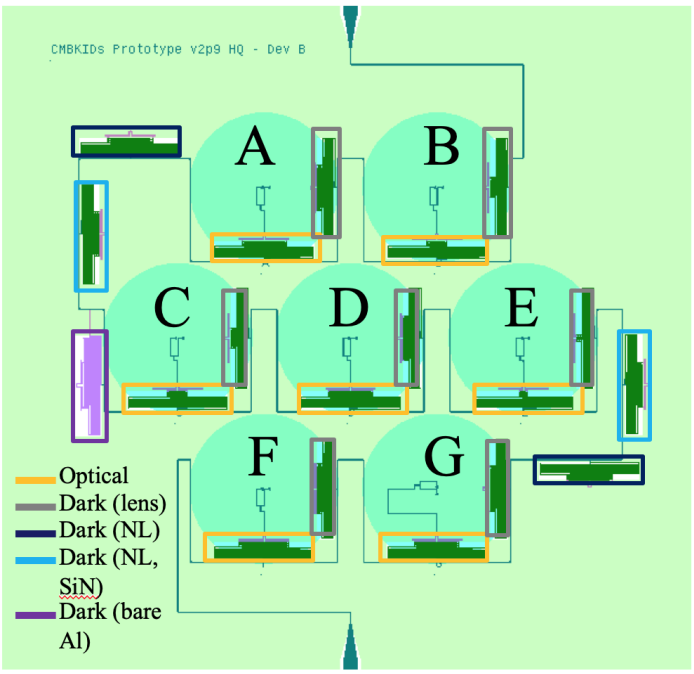

Figure 3.2: Bird-eye overview of the prototype array. There are 7 lenslets on the chip, with an optical and dark KID for each pixel. There are also 5 additional ancillary KIDs to diagnose the device: two dark KIDs (NL) that have the same geometry as the KIDs underneath lenslets, two dark KIDs that have silicon nitride coverage (NL, SiN), and 1 dark bare Al KID. The ground plane layer of the design, including the antenna slots, is not shown to avoid overcrowding the figure.

Position	Type	Design Freq. (MHz)	Inductor leng. (µm)
A, D, G	Optical, Dark	750	1800
E	Optical, Dark	850	300
B, C	Optical, Dark	800	800
F	Optical, Dark	700	2000
Anc.	Dark (NL, NL SiN)	570	1800
Anc.	Dark (NL, NL SiN)	1100	1800
Anc.	Dark (Bare Al-only)	540	1800

Table 3.1: Design parameters for the different MKIDs on the prototype array.

The main parameters of the antenna, namely the slot length (l), slot width (w), and slot separation distance (d), were chosen to have optimal performance at 150 GHz band while keeping impedance matched to the microstrip line. Simulations were done using the Ansys HFSS 3D electromagnetic simulation software where a parameter sweep was done for the three slot parameters. The final antenna design has the following parameter values: $l = 739\,\mu\text{m}$, $w = 12\,\mu\text{m}$, and $d = 288\,\mu\text{m}$. Simulations showed the antenna S_{11} response to be ≤ -10 dB ($\leq 10\%$ power reflected) in the range of 148-152 GHz. The far-field beam pattern has the gain falling off by 10 dB at 20^o angle.

3.3 Fabrication

Fabrication is done on a high resistivity (> 4 kΩ·cm) silicon wafer. Figure 4.2 shows the process flow in detail and contains the step numbers referred by the text below in parentheses.

Prior to each lithography step, the wafer is cleaned using acetone, isopropyl alcohol (IPA), and deionized (DI) water baths and then vacuum baked at 90^oC for 3 minutes to dehydrate the surface. The specific parameters used in each lithography and plasma etch/deposition are shown in Tables 4.1 and 4.2, respectively.

The wafer is first cleaned with a sonicated acetone bath, IPA and water bath. A hydrofluoric (HF) acid bath dip removes native oxide followed by a 150^oC vacuum bake for 15 minutes to dehydrate the wafer. We then deposit 50nm of Al via sputtering[1]. After spin-

1. AJA ATC 2200 Sputtering System: https://www.ajaint.com/atc-series-sputtering-systems.html

ning resist (cf. Table 4.1), we expose the pattern using a maskless lithography writer from Heidelberg Instruments[2]. The film then etched using a standard Al wet etchant containing phosphoric and nitric acid (step 1). To remove the photoresist after etching, we use an O_2 plasma asher[3] at 70^oC and 300 W for 240 seconds to descum the wafer before using a NMP (1-Methyl-2-pyrrolidon) bath heated at 80^oC. This is then followed by ultrasonic NMP bath, IPA, and DI water rinse.

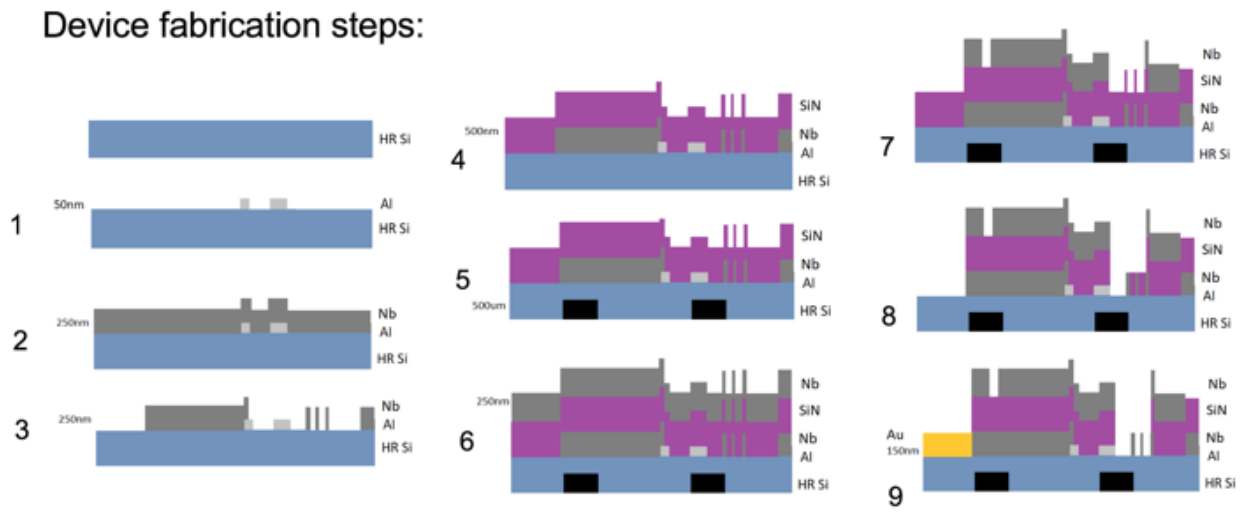

Figure 3.3: Cartoon of cross section view of the wafer during all the processing steps. The bottom right figure shows the microwave readout region, the IDC, and the mm-wave transmission line from left to right. See text for details of process steps.

Step	Layer	Photoresist	Laser (nm)	Dosage (mJ/cm^2)
1	Al KIDs	AZ 1512	375	130
3,7	Nb CPW/ground plane	AZ 1512	375	100
5	Si holes/lenses	AZ 1518	405	135
8	SiN_x	AZ 1512	375	110
9	Au pads	AZ 1518	405	150
	SU-8 posts	SU-8 3050	375	245

Table 3.2: Lithography details for fabrication of detector wafer and lens seating wafer. Step number matches the process step shown in Figure 4.2.

2. Heidelberg MLA150: https://himt.de/index.php/maskless-write-lasers.html

3. YES CV200 RFS Plasma Strip/Descum System: http://www.yieldengineering.com/products/plasma-strip-descum-systems/cv200rf-series

Once the wafer is clean from the Al processing, we deposit 250 nm of Nb using sputtering (step 2). This layer contains much of the transmission lines, i.e. microstrip lines for the mm-wave and CPW lines for readout, as well as the IDC fingers for our KIDs. Two critical junctions need to be taken care of, namely the junction of the Nb microstrip line feeding the mm-wave signal to the Al inductor, and the connection between Al inductor and Nb IDC. To ensure proper galvanic contact at these junctions, we do 1 minute of ion beam milling to remove the native oxide on the Al inductor surface in the same vacuum chamber immediately before doing the Nb deposition. The ion milling process was tested to ensure less than $\lesssim$ 2 nm of the Al inductor would be removed. The Nb layer is then patterned and dry etched using an inductively coupled plasma (ICP) fluorine etcher[4] (step 3). We then grow the dielectric layer of our microstrip, 500 nm of SiN_x, over our wafer (step 4) using High Density Plasma Chemical Vapor Deposition (HPDCVD)[5]. After depositing the dielectric layer, we pattern alignment features on the backside of our wafer and etch $\approx$80 µm into the silicon wafer with the deep silicon Reactive Ion Etcher (RIE)[6] (refer to Section 3.3.1 more details on the lens alignment technique). We then deposit another 250 nm of Nb on top of the SiN_x layer which acts as the groundplane via sputtering (step 6). We pattern and etch to form the antenna slots and ground plane (step 7) and remove the SiN_x (step 8) using the ICP fluorine etcher to remove the dielectric from the IDCs and CPW wirebond pads. The final step is to deposit Au pads to ensure proper thermal contact between the chip and the resonator box. This is done via liftoff where we pattern our wafer and then deposit $\sim$100 nm of Au on top of the wafer with patterned resist using an electron beam evaporator[7]. A thin layer ($\sim$ 10 nm) of Ti is deposited to "wet" the surface in order for the Au to adhere to the bare Si wafer. The wafer is then left to sit in a heated NMP bath overnight for the Au film to liftoff. Wafer is then cleaned using a sonicated NMP bath, IPA, and DI water

4. PlasmaTherm ICP Fluorine Etcher: http://www.plasma-therm.com/apex_SLR.html

5. PlasmaTherm VERSALINE HDPCVD: http://www.plasma-therm.com/versaline.html

6. PlasmaTherm VERSALINE DSE: http://www.plasma-therm.com/versaline-dse.html

7. Angstrom EvoVac Electron Beam Evaporator: https://angstromengineering.com/products/evovac/

Step	Recipe	ICP Pow. (W)	Bias Pow. (W)	Pres. (mTorr)	He Pres. (Torr)	Gas 1 (sccm)	Gas 2 (sccm)	Gas 3 (sccm)
3,7	Nb etch	600	50	50	5	CF_4, 40	CHF_3, 10	Ar, 10
4	SiN_x dep	400	20	10	5	SiH_4, 20	N_2, 2	Ar, 20
8	SiN_x etch	100	20	30	5	SF_6, 20	-	-

Table 3.3: Recipes used for fabrication. Step number matches the processes shown in Figure 4.2.

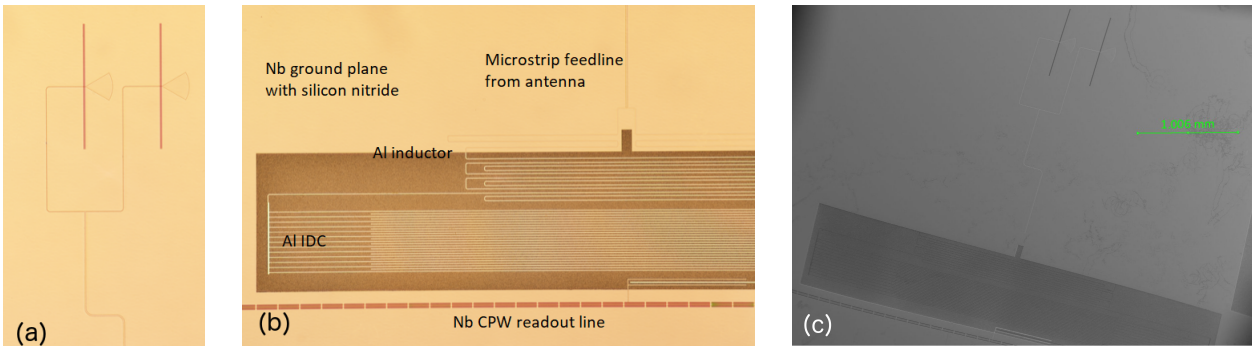

Figure 3.4: *Left.* Optical microscope image of the antenna and Nb microstrip structure. *Middle.* Optical microscope image of the feedline coupled to the KID. The KID is capacitively coupled to the Nb feedline at the bottom. *Right.* Scanning electron microscope (SEM) image of a fabricated single polarization antenna-coupled KID.

rinse. Finally, photoresist is spun on top of the wafer and it is diced, and a chip is ready to be tested. Microscope images of the final devices are shown in Figure 4.1. A photograph of the chip mounted in a resonator box and the lens-side version is shown in Figure 3.7

3.3.1 Lens Seating Wafers

To focus radiation onto the antenna, we use 1/4-inch diameter alumina lenslets with a thermoformed polyetherimide anti-reflection (AR) coating optimized for 150 GHz. The spherical lenses are placed into a seating wafer that provides a well-defined extension length to maximize the antenna directivity (Quealy, 2012; Filipovic et al., 1993). An image of the lens wafer with lenses is shown in Figure 3.3.1.

The lenslets are glued onto the lens seating wafer, which is made from a 500 µm thick double-sided polished silicon substrate. We pattern the lenslet holes, as described in Table 4.1, and subsequently etch 250 µm into the wafer. Alignment between the antenna and

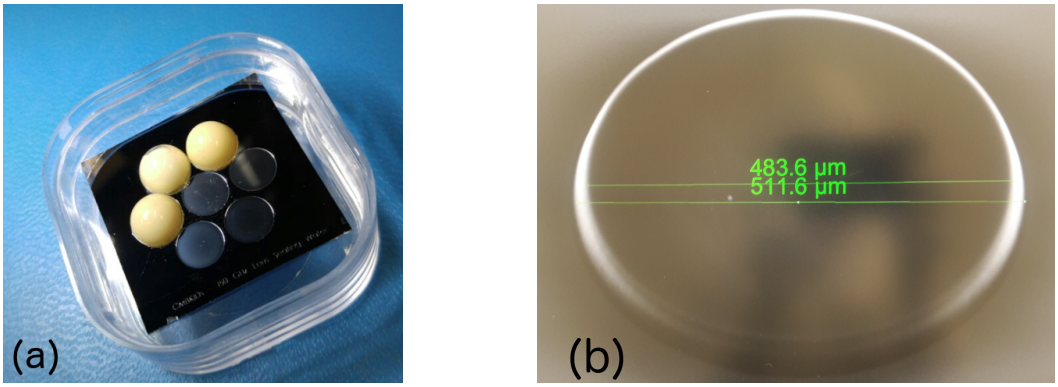

Figure 3.5: *Left.* Photograph of the lens seating wafer partially populated with alumina lenslets. *Right.* SEM image of a SU-8 post on the lens seating wafer. The diameter is measured to be roughly 500 µm and the height is 70 µm.

lenses is critical to have a well-defined beam. To do this, we pattern posts made from SU-8 3050, a permanent epoxy negative photoresist, on the backside of the wafer, with parameters specified in Table 4.1. After the photoresist is developed, the wafer is baked at 160^oC for 2 hours to cure the SU-8 posts. Each post is approximately 70 µm tall and 500 µm wide in diameter (Figure 3.3.1), designed to fit the 80 µm deep holes on the backside of the detector wafer. To measure the misalignment, Figure 3.3.1 shows the mismatch between two wafers aligned this way viewed through an infrared (IR) camera microscope. We observe a maximal misalignment of 20 µm after multiple realignments of the wafer assembly. Figure 3.3.1 shows the side view of the lens wafer when the holes and posts are aligned and misaligned.

3.4 Experimental Setup

3.4.1 Cryostat Setup

Testing was done in two cryostat setups. For the microstrip resonator chips designed to measure the microwave loss of the SiN dielectric layer (see Section 3.5), we use an adiabatic demagnetization refrigerator (ADR). For all other testing described in this work, we use a helium-3 dilution refrigerator.

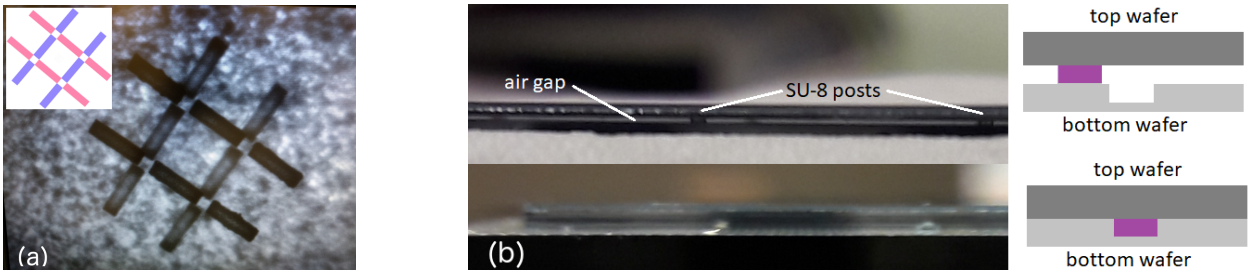

Figure 3.6: *Left.* IR microscope image of the alignment of SU-8 posts to holes by viewing two wafers with different features lying one on top of another. Each rectangular bar measures 50 µm x 200 µm. Rectangles of the same orientation are on the same wafer. When perfectly aligned, the ends of four orthogonal rectangles should form a square, as shown in the upper left inset image. We estimate misalignment to be no more than 20 µm. *Right.* Side view of the lens wafer when the posts are misaligned with the holes (top) and aligned (bottom). A cartoon is shown as a comparison to illustrate SU-8 post and hole alignment. The posts are shown in purple and wafers in gray.

Dilution Refrigerator

The helium dilution refrigerator is a Bluefors cryogen-free Dilution Refrigerator. The operating principle behind dilution refrigerators uses He-3 and He-4 isotopes. The working fluid is He-3, being moved by vacuum pumps. At around 800 mK, the mixture will separate into a concentrated phase (He-3 rich) and a dilute phase (He-3 poor). In the mixing chamber, heat is needed to move He-3 atoms from the concentrated into the dilute phase, causing cooling to occur. The heavier He-4 will settle at the bottom of the mixing chamber due to gravity. He-3 has a much higher vapour pressure than He-4, causing the helium that is pumped away to be almost pure He-3, and osmotic pressure drives He-3 from the mixing chamber to still where it is pumped away. The evaporated He-3 is then pumped back into the cryostat to feed the cycle.

For this cryostat, 20 dB of attenuation is put on the 4 K stage. A further 30 dB of attenuation is put on the the stage connected to the mixing chamber, which is capable of reaching temperatures ∼10 mK. Stainless steel cables are used to feed the signal from room to the 4 K stage, and CuN/NbTi cables are used to connect the 4 K stage to the mixing chamber stage. The device is mounted on a plate heat sunk to the mixing chamber stage

and connected to the microwave readout line via flexible Cu cables. We connect the device output line to silicon germanium (SiGe) amplifier mounted on the 4 K stage, which has a gain of ∼20 dB from 0.1-9 GHz.

ADR Cryostat

The ADR cryostat is a Model 104 Olympus cryostat made by High Precision Devices, Inc. The working principle of an ADR utilizes the change in heat capacity of the magnet (paramagnetic salt pills) with change in magnetic field. During the adiabatic magnetization stage, the magnetic field is slowly increasing, causing the magnetic dipoles to align, lowering the magnetic entropy and heat capaciy. The magnet is connected to a thermal sink (in our case a 4 K plate cooled by a pulse-tube cryocooler) so the excess heat is carried away. The magnet is then left to soak at the maximum magnetic field for some time to allow thermal equilibrium between the salt pill and the heat sink. Then the magnet is disconnected for from heat sink, and the magnetic field is slowly ramped down during the adiabatic demagnetization stage. The magnetic dipoles randomize, causing the entropy and heat capacity to increase. Since the magnetic is no longer connected to a heat sink, the increase in heat capacity causes a decrease in temperature.

For our cryostat, two internal stages are mounted on the 4 K plate, for which the refrigerants are used to reach temperatures of ≈ 500 mK and 50 mK (the detector stage). This stage has a temperature range of 50 mK to ≈ 2 K. We connect the device output line to CIT-CRYO-12A high electron mobility transistor (HEMT) amplifier mounted on the 4 K stage, which has a gain of ∼20 dB from 0.1-12 GHz. DC blocks are placed on both the input and output lines on the 50 K, 4 K, and 500 mK stages for thermal isolation and two cryogenic 20 dB attenuators are placed along the input to the device to minimize thermal noise. The input power at the device is ~ -90 dBm and the readout amplification gain from the HEMT amplifier and a commercial room temperature amplifier is ≈ 50 dB.

3.4.2 Resonator Box

The device chip is mounted on a custom gold-plated OHFC copper box (Figure 3.7). The chip held in place via flexible Cu clips at the corners that can be screwed down. To reduce vibration from the pulse-tube, we further secure the chip in place by using rubber cement along the edges of the chip to bond it to the box. The RF connection is made via SMA connector from the outside of the box. In the interior of the resonator box, the centre pin of the SMA connector is then soldered onto a microstrip launchpad made using a TMM101 substrate. We use Al wires to wirebond the microstrip line of the box to the Nb CPW readout line of the chip. Several Al wirebonds are made along the perimeter of the chip to connect the resonator box to the ground plane of the chip.

For optical testing, the alignment procedure with the lens seating wafer is described in Section 3.3.1. Since the Al wirebonds are superconducting under 1 K and cannot be used for thermal connectivity, we also use Au wirebonds to connect Au pads of the chip to the box for thermal contact.

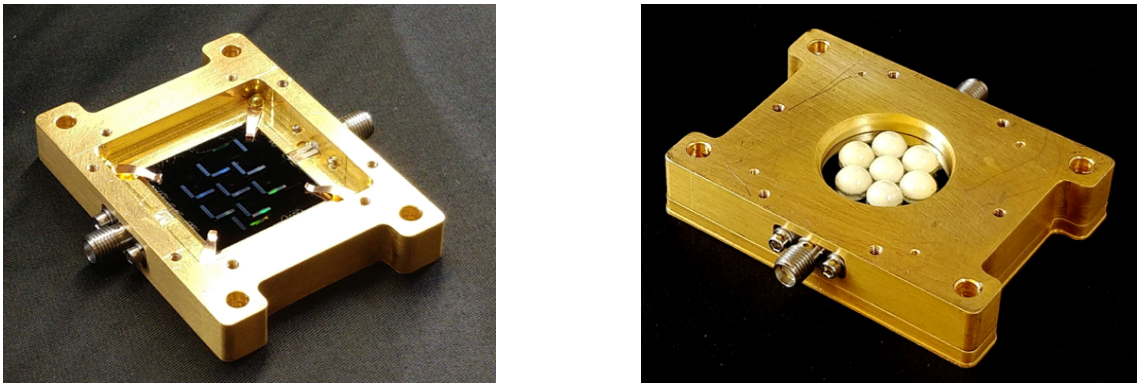

Figure 3.7: *Left.* Photograph of the device chip mounted in a resonator box. *Right.* Photograph of the lens-side of the resonator box. The 150 GHz bandpass filter is not shown.

3.4.3 Measurement Setup

The RF measurements reported in this work are performed either using a vector network analyzer (VNA) to characterize the response of the resonators or single-tone homodyne

readout to study resonator noise.

For measurements done using the VNA, the input signal from Port 1 of VNA is sent to a variable attenuator and then to the input of the cryostat via standard SMA cabling. The signal from the output of the cryostat is passed through a 1400 MHz low-pass filter and two room temperature amplifiers (each with $G \approx 35$ dB) with a 20 dB attenuator in between before being sent back into Port 2 of the VNA.

The setup for noise measurement is very similar. However, a synthesizer is used to generate the tone, which is then fed into a splitter. One end goes to a variable attenuator and cryostat, following the same path as that of the VNA measurement, but is sent to the RF port of an IQ mixer after room temperature amplification. The other end from the splitter is sent directly to the local oscillator (LO) port of the IQ mixer. The IQ mixer's output (the $I(t)$ and $Q(t)$ of the S_{21} described in Section 2.3) are then furthered filtered via low-pass filtered and digitized via a set of analog-to-digital converters (ADCs) before sent to the computer for data storage and analysis. Figure 3.8 shows a schematic diagram of this configuration.

3.4.4 Optical Measurement Setup

For making optical measurements of the prototype device, we use a blackbody mounted on the 4 K shield of the dewar directly facing the resonator box. The blackbody is made out of a copper plate coated in Eccosorb CR-110 with SiC crystals embedded to minimize reflection. The blackbody is thermally isolated from the 4 K shield by suspending it onto a plate using Kevlar strings. The whole unit is then bolted onto the 4 K shield. For the resonator box, we mount a 150 GHz bandpass filter directly on top of the lenslets.

The temperature of the blackbody is regulated using an attached resistive heater and thermometer. Using a proportional–integral–derivative (PID) controller with our setup, the blackbody can reach up to a temperature of roughly 50 K. We first take a measurement using the VNA setup and locate the resonances at base temperature. Subsequent VNA sweeps are

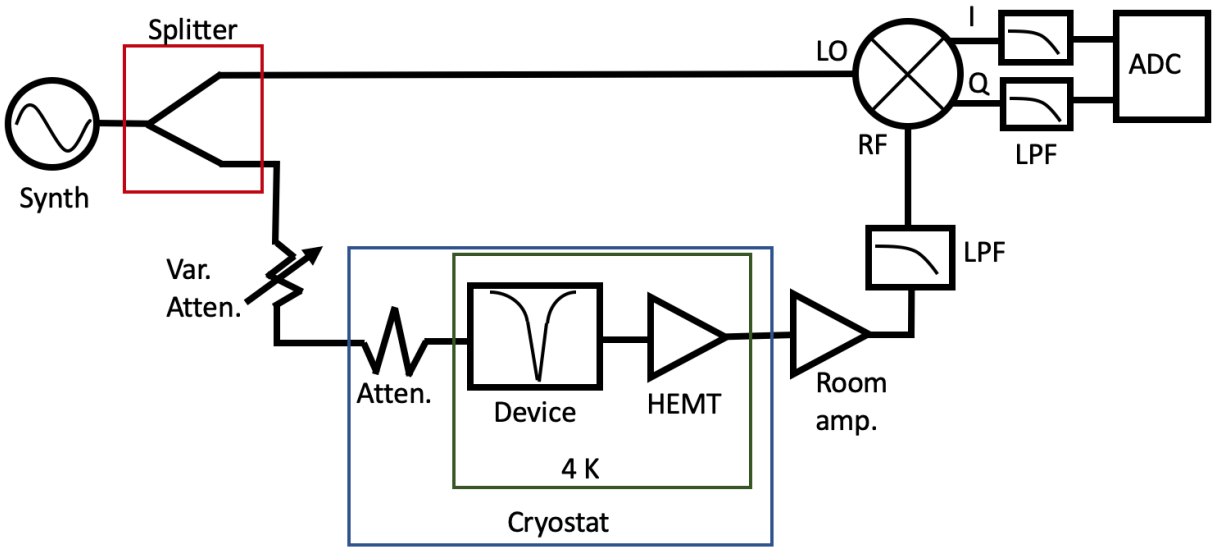

Figure 3.8: Schematic of the single-tone homodyne readout configuration for noise measurement. A synthesizer produces a single tone, which is split into two paths. One goes through various attenuation and into the cryostat, where the signal is amplified after it passes through the device. After room temperature amplification, the signal passes through a low-pass filter (LPF) and then goes into the RF port of an IQ mixer. The other end from the splitter goes directly into the LO port of the splitter. The output of the IQ mixer are I and Q of the S_{21}. These signals are passed through a LPF before being digitized by an ADC and collected into the computer for storage and analysis.

done to measure the resonances at different blackbody temperatures.

3.5 Microstrip Test to Characterize SiN Dielectric

To measure the microwave loss in the microstrip carrying the optical signal from antennae to the KID, we design and fabricate test microstrip resonators (Figure 3.5.1), which have a resonance frequency of $\sim$ 5 GHz, using the same materials as described in Section 4.3. The ground plane with the CPW lines is made by e-beam deposition of 175 nm of Nb on high resistivity silicon wafers (>4 kΩ). 500 nm of SiN_x is then grown on top, followed by a deposition of 225 nm of Nb sputtered using lift-off to form the microstrip resonators. The lithography, SiN_x deposition and etch recipes used are the same as the ones in Table 4.1 and 4.2.

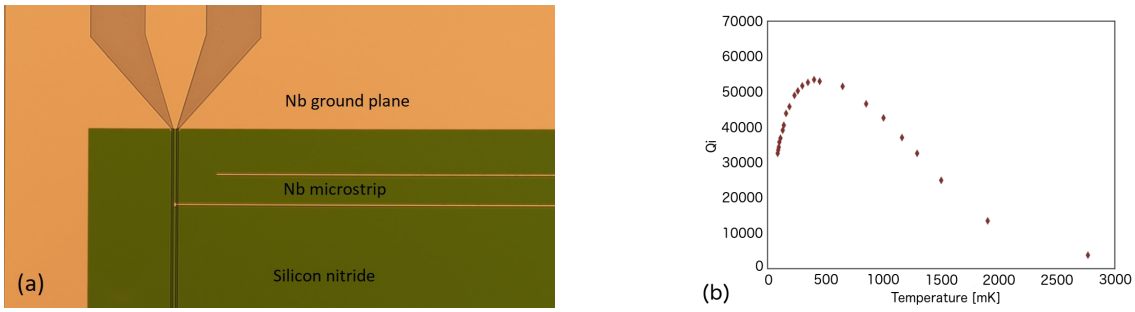

Figure 3.9: *Left.* Optical microscope image of the test Nb microstrip with SiN_x structure. *Right.* Plot of Q_i values obtained from S21 curves at different temperatures of the Nb microstrip with an input power of ≈ -90 dBm. The degradation in Q at $T < 500$ mK is attributed to two-level system behaviour, while at $T \gtrsim 1$ K, this is due to thermally excited quasiparticles.

3.5.1 Data Fitting

We test our devices by mapping the complex transmission as a function of frequency for each resonator, by sending tones from the vector network analyzer to obtain the two-port S_{21} transmission function. The resonance can be modeled as a Lorentzian parametrized by Equation 2.42

Our measurements show the feasibility of fabricating a low-loss microstrip using SiN_x. Figure 3.5.1 shows the Q_i values as a function of stage temperature, inferred from the S_{21} curve fitting at each temperature using Eq. (2.42). The ambient bath temperature on the focal plane of a CMB telescope is estimated to be between 200-300 mK. We measure $Q_i \approx 40,000$ at this temperature and $f_r \sim 5$ GHz. Although these performance at microwave wavelengths are different than that at the mm-wave wavelengths, this measurement gives us confidence that the dielectric loss is will not be significant at the microwave regime.

3.6 Results

3.6.1 Characterizing Resonators

The initial prototypes gave an yield of ~80% across different wafers, mostly due to fabrication defects. A sample VNA sweep of a resonator is shown in Figure 3.10.

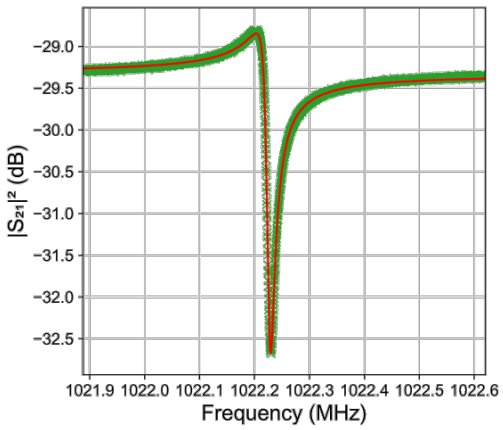

Figure 3.10: S_{21} of a sample resonator on a prototype array.

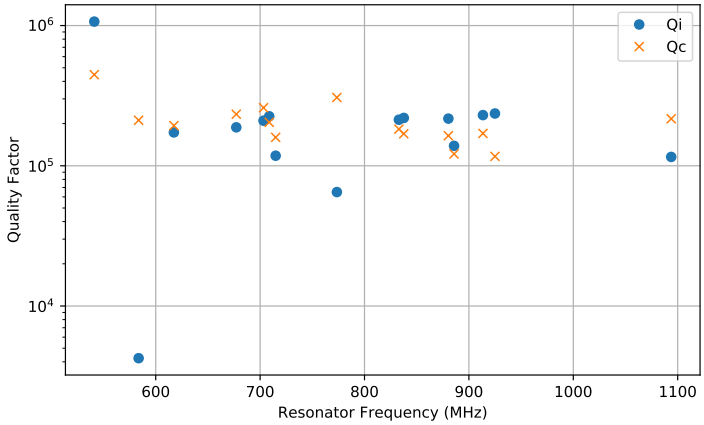

Figure 3.11: Plot of the internal and coupling quality factors (Q_i and Q_c) obtained from fitting to the S_{21} data of the VNA resonator sweeps.

We fit the S_{21} data of each resonance using Equation 2.42 to estimate the resonator's internal and coupling quality factors (Q_i and Q_c). Then the estimated Q_i and Q_c are compiled for all resonances on a prototype chip. The result can be seen in Figure 3.11. Most of the resonators exhibit $Q_i \sim 10^5$, which matches well with Q_c. In addition, the bare Al KID consistently has very high $Q_i \sim 10^6$ across various chips, which indicated very good film quality for our detectors. We also see that dark test resonators that have SiN coverage over the IDC fingers have much lower Q_i ($\sim 10^3$) than rest of the resonator.

3.6.2 Noise Performance

We collect and analyze the noise performance of the prototype array by the method described in Section 2.6.5. Figure 3.12 shows the resulting noise spectrum. A fit is done using Equation 2.63 to extrapolate a quasiparticle lifetime of τ_{qp} =850 µs from the roll off in the noise spectrum. The NEP shown on the right y-axis is calculated using Equation 2.64. As described in Baselmans (2012), we can rewrite $\delta\theta/\delta N_{qp}$ in Equation 2.64 as

$$\frac{\delta\theta}{\delta N_{qp}} = \frac{\delta\theta}{\delta f_r}\frac{\delta f_r}{\delta N_{qp}} \tag{3.4}$$

where f_r is the resonance frequency. For small variations around f_0 (f_r at $T = 0$ K), we can use the approximation $\delta\theta/\delta f_r = 4Q/f_0$. Additionally, $\delta f_r/\delta N_{qp}$ is linear. This means we can measure this relation by looking at the dark response for KIDs with different inductor volumes. The inlet figure of Figure 3.12 shows the dark responsivity (fractional frequency shift) as a function of quasiparticle density, using the different KID geometries described in Table 3.1 and calculating the equilibrium quasiparticle density using Equation 2.8. A linear fit to this data is done, which is then used in Equation 2.64 to calculate the detector NEP.

Figure 3.12 also shows the expected noise from an optical loading of 1 pW at 150 GHz, which is typical for a ground-based CMB experiment. From the results, we see that the performance of this device is well below the expected photon noise down to 1 Hz. There is an obvious increase in noise at lower frequencies, which can be attributed to TLS noise. This can be mitigated by changing the capacitor geometry and better substrate preparation during the device layer fabrication.

3.6.3 Optical Performance

In Section 3.2.2, we described how dark KIDs were placed under each lenslet at the same distance as the optical KIDs. The purpose of this was to characterize any parasitic light coupling directly into the KIDs rather than through the antenna and microstrip.

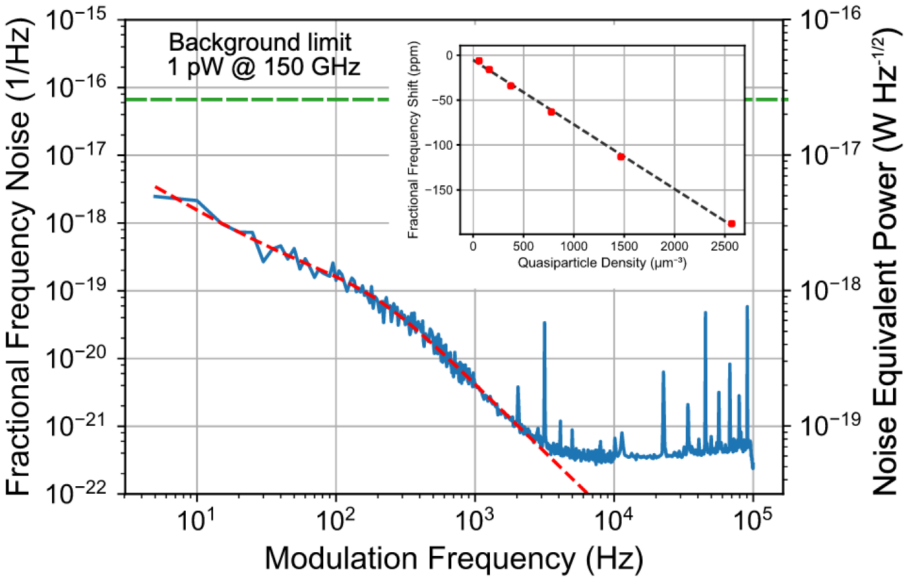

Figure 3.12: Fractional frequency noise spectrum and NEP of the detector. A fit is done (dashed red line) to extrapolate the quasiparticle lifetime $\tau_{qp} = 850\,\mu s$. The inset figure shows the dark responsivity, namely the fractional frequency shift as a function of quasiparticle density, that goes into the NEP calculation in Equation 2.64. This is obtained by looking at the dark response for KIDs with various inductor volumes. Taken with permission from Barry et al. (2018).

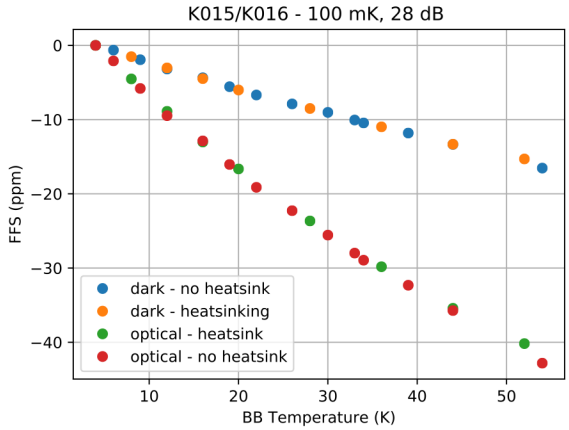

Figure 3.13: Fractional frequency shift of the optical and dark resonator under lenslet E as a function of blackbody temperature, showing the dark resonator (blue and orange dots) are seeing ∼35% of optical power as the optical resonator (red and green dots). This measurement also showed that heat sinking the resonator box did not significantly affect the resonance frequency.

Figure 3.13 shows optical response of the optical and dark KIDs sitting under lenslet E, while sweeping the blackbody temperature. Although we see the optical KID has a good responsivity with optical power, unfortunately we also see the dark KID respond. This behaviour is repeated across the array, with the dark KIDs overall seeing about ∼35% of the optical power as the optical KID.

We theorize there is unwanted stray light that can couple to the silicon substrate outside the lens and antenna architecture. The stray light photons, which may also possibly generate phonons in the wafer substrate, which were able to propagate throughout the wafer, causing the dark KIDs to respond with increasing blackbody power.

3.7 Summary

In summary, we have designed, fabricated, and characterized a 7-pixel prototype antenna-coupled KID array intending for CMB applications. Light couples in through dual-slot antenna, which is connected to a Nb/SiN/Nb microstrip feedline that brings the mm-wave signal to the Nb/Al LEKIDs. A novel alignment technique was developed to align the lens

seating wafer to the detector wafer via an epoxy-like post and holes etched on the detector wafer. The misalignment was characterized to be $\lesssim 20\,\mu\text{m}$. Additionally, we have measured the SiN_x microstrip structure to characterize the dielectric material, which was found to be very low-loss at 5 GHz, with $Q_i \approx 40,000$ at $\sim$200 mK.

The resonators on the prototype array demonstrates high responsivity and quality factors ($Q \gtrsim 10^5$). However, unwanted stray light was found to be coupling to the detectors, where the dark KIDs were responding at about $\sim 35\%$ of the optical power as the optical KIDs. To solve this stray light pick up issue, we need to think of alternative ways to couple light into the detectors that does not cause light to propagate through the silicon substrate. Such a design will be described in the following chapter.

CHAPTER 4

OMT-COUPLED KIDS FOR CMB DETECTION

This chapter describes work that was published in Tang et al. (2020).

In this chapter, we present a prototype planar orthomode transducer (OMT)-coupled multi-colour KID array optimized for 220/270 GHz frequency bands. These devices are made from silicon-on-insulator (SOI) wafers to provide a low-loss substrate for the KIDs. The OMT couples the two polarizations of light from a wide-band feed-horn to separate Nb/SiN/Nb microstrip lines, which are then coupled to Al/Nb lumped-element KIDs (LEKIDs). The silicon on the backside of the OMT is etched away using deep reactive ion etch (DRIE) to release the OMT membrane to enable operation over a wide-bandwidth. Finally, the buried oxide is removed underneath the KID capacitors in order to minimize two-level system (TLS) noise and loss mitigation.

4.1 Introduction

The next generation cosmic microwave background experiment (CMB-S4) is a collaboration with several telescopes in the Atacama desert of Chile and the South Pole. The main science goals include testing the theory of inflation, solving the neutrino mass hierarchy problem, hunting for light relics from the early universe, and measuring the evolution of massive galaxy clusters (Abazajian et al., 2016). However, the target sensitivity needed to do this requires $\approx 5 \times 10^5$ detectors. The traditional detectors used for CMB experiments, the transition edge sensor (TES) bolometers, are well-understood and characterized. Nonetheless, scaling up to 10^5 detectors for TES bolometers remains a challenge in terms of fabrication and readout multiplexing.

Kinetic inductance detectors (KIDs) are a type of athermal pair-breaking detectors that offer high multiplexing ratios without the need for ancillary wired connections.

Several non-CMB millimeter and sub-millimeter wavelength experiments have deployed -

or are currently developing - KIDs, such as SuperSpec (Shirokoff et al., 2012), NIKA2 (Adam et al., 2018), TolTEC (Austermann et al., 2018), and BLAST-TNG (Galitzki et al., 2014). Feedhorn-OMT coupled detectors are now commonly used in CMB experiments due to the low polarization error and control over beam shape that can be achieved with feedhorns.

There are multiple on-going developments toward feedhorn coupled multi-colour KID polarimeters for CMB experiments. To date, most designs have been based on OMT-coupled $\lambda/4$ CPW resonators using a novel optical coupling scheme, such as the devices proposed by Johnson et al. (2018). Resonators based on distributed resonators present a unique challenge, and are constrained by the competing requirements to both absorb the power along the length of the region of high-current density and not sacrifice noise and stability.

In the LEKID-based design we present here, the inductor and capacitor elements of the KID are physically separated, allowing independent optimization of the inductor that forms the mm-wave absorber, and the capacitor geometry, critical to the stability of the resonator. In this chapter, we present the development of a prototype 8-pixel array of two-colour, dual-polarization, OMT-coupled LEKIDs.

4.2 Design

The current design of the detectors is optimized for the 220 GHz and 270 GHz band observation (each with observing band of 20%). These frequencies are needed in CMB experiments to constrain the foreground contamination of the CMB signal by measuring the thermal emission from galactic dust. Incoming light travels down an array of feed horns, feeding a single-mode circular waveguide to the OMT structure on our detector wafer. To maxmize the optical coupling efficiency across the observing band, the OMT probes are placed on a 4 µm thin Si device layer of a silicon-on-insulator (SOI) wafer, which has been released from the bulk Si wafer. A quarter wavelength backshort and RF choke are located behind the OMT probes and are required to maximize coupling of the signal to the OMT and minimize stray signal leakage into the Si carrier wafer. The signal travels from the Nb OMT probes to the

microstrip via a CPW-to-microstrip transition section. We employ a $Nb/SiN_x/Nb$ inverted microstrip, based off Section 3.2. We use a cross-under structure to gather the signal from the orthogonal OMT probes for a single polarization to a hybrid tee. We also use a set of band-pass microstrip filters to define our observing band. The combined mm-wave signal from the hybrid goes into the Al inductor part of the LEKID. The interdigitated capacitor (IDC) is formed from Nb to both maximize responsivity by confining quasiparticles to the inductor, while reducing direct stimulation in the capacitor. Lastly, the KID is capacitively coupled to the Nb readout transmission line. A paper with a more detailed discussion of the design and the optimization procedure of the detectors is currently in preparation.

4.3 Fabrication

Fabrication begins with a 4-inch high resistivity ($> 1\,\mathrm{k}\Omega \cdot \mathrm{cm}$) silicon-on-insulator (SOI) wafer, with a handle thickness of 450 µm, a 0.5 µm silicon oxide layer, and 4 µm device layer. Fig. 4.2 shows the process flow in detail and contains the step numbers referred by the text below in parentheses. The specific parameters used in each lithography and plasma etch/deposition are shown in Tables 4.1 and 4.2, respectively. Microscope images of the final devices are shown in Fig. 4.1.

Prior to each lithography step, the wafer is cleaned using a sonicated acetone, isopropyl alcohol (IPA), and deionized (DI) water baths, followed by a vacuum dehydration step. After spinning resist (cf. Tab. 4.1), we expose the pattern using a maskless direct write lithography writer from Heidelberg Instruments[1]. We remove the resist after each etching step first by using an O_2 plasma asher[2] at 70^oC to remove the crust layer of resist. We then clean the wafer using a heated sonicated NMP (1-Methyl-2-pyrrolidon) bath, followed by an IPA and DI water bath.

1. Heidelberg MLA150: https://himt.de/index.php/maskless-write-lasers.html

2. YES CV200 RFS Plasma Strip/Descum System: http://www.yieldengineering.com/products/plasma-strip-descum-systems/cv200rf-series

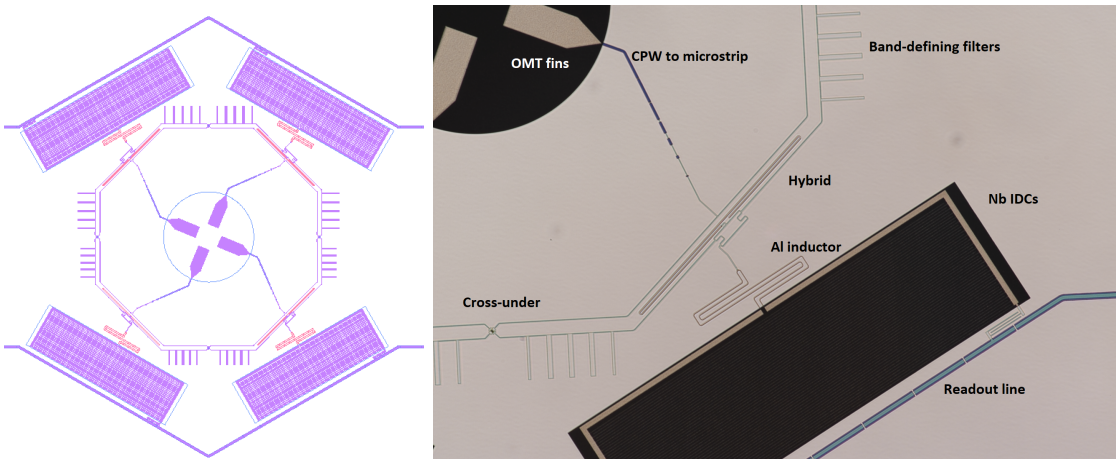

Figure 4.1: *Left.* Layout design of an pixel on the chip. *Right.* Labelled close-up of the OMT structure coupled to a KID through a microstrip.

The SOI wafer (step 0) is first cleaned with a buffered hydrofluoric (HF) acid bath dip to remove the native oxide followed by a dehydration step. We then deposit 100 nm of sputtered Al (step 1) [3]. The Al layer forms the inductor and the sum-port termination of the hybrid, and is etched using a standard phosphoric acid-based Al etchant (step 2). Prior to depositing the Nb layer, we perform a short ion-mill step to remove the native oxide to ensure a clean galvanic contact between the Al and the Nb layers. Then we sputter 250 nm of Nb layer (step 3). We pattern the OMT probes, interdigitated capacitor (IDC) fingers, microstrip wiring, and readout lines on the Nb layer. The Nb layer is then dry etched using an inductively coupled plasma (ICP) fluorine etcher[4] (step 4, cf. Tab. 4.2). We then grow the dielectric layer of our microstrip, 500 nm of SiN_x, over our wafer (step 5) using High Density Plasma Chemical Vapor Deposition (HDPCVD) [5]. We also deposit 2 µm of silicon oxide (SiO_x) on the backside of the wafer (step 6) to counteract the stress of the oxide layer on the device side of our wafer and to serve as extra protection for the deep silicon etch.

After depositing the dielectric layers, we pattern alignment features on the backside of our wafer and etch into the SiO_x layer on the backside of the wafer with the ICP fluorine

3. AJA ATC 2200 UHV Sputtering System: http://www.ajaint.com/atc-series-sputtering-systems.html

4. PlasmaTherm ICP Fluorine Etcher: http://www.plasma-therm.com/apex_SLR.html

5. Plasma-Therm Apex SLR: http://www.plasma-therm.com/versaline.html

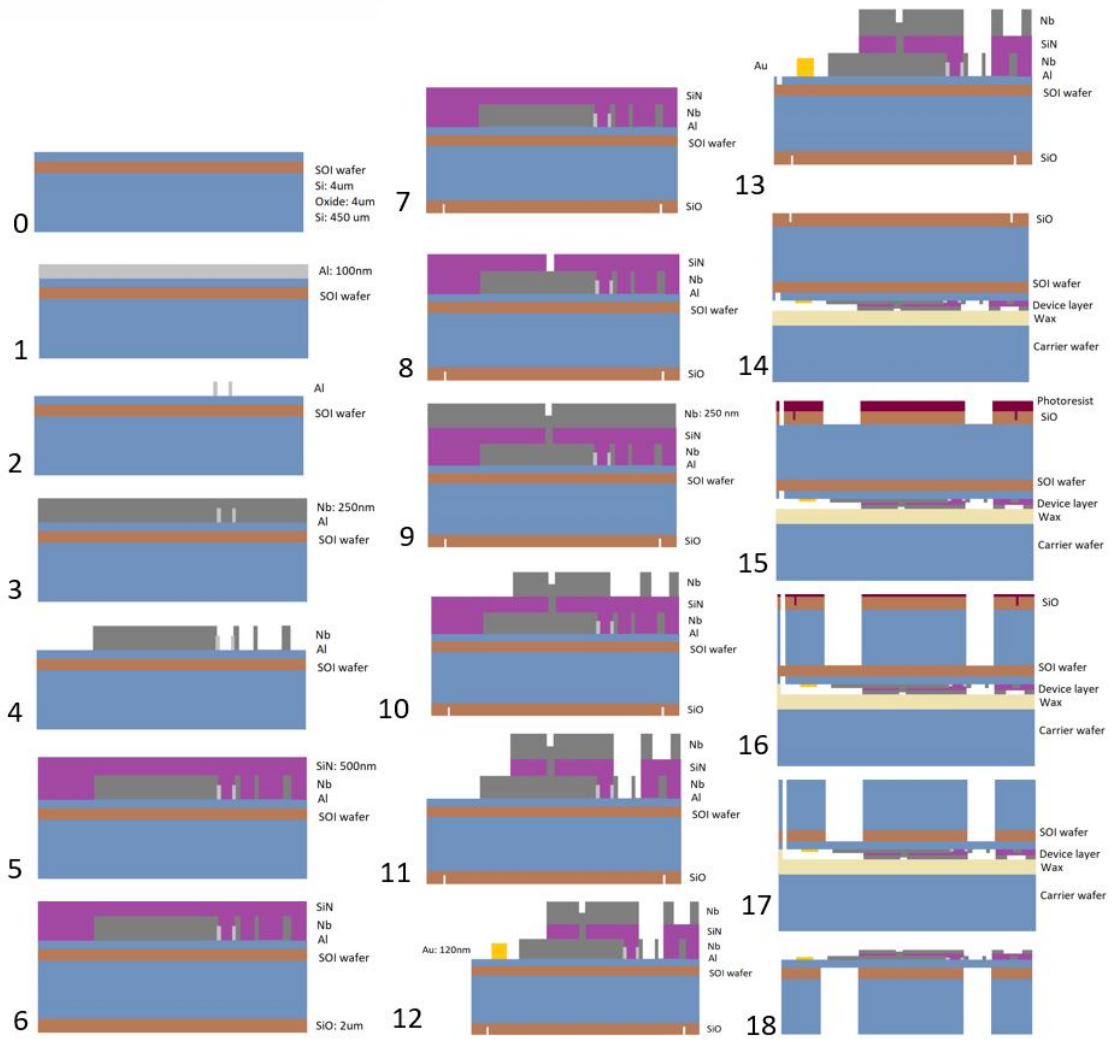

Figure 4.2: Cartoon of cross section view of the wafer during all the processing steps. The bottom right figure shows the OMT and mm-wave transmission line, the IDC, and the microwave readout region from left to right. See text for details of process steps.

etcher (step 7). We then remove the resist and pattern the SiN_x layer on the frontside of the wafer and fluorine etch to open up the nitride for the vias for the crossover structure for our microstrip (step 8). After removing resist, we use an ion gun again to remove any oxide on the exposed bottom layer of Nb structures (to ensure galvanic contact for our cross-under wiring) before sputtering 250 nm of Nb (step 9) as our ground plane. We pattern and etch the Nb layer to form the OMT membranes and open up the KIDs (step 10) and subsequently pattern and etch the SiN_x layer to open the capacitor part of our detectors (step 11). We then do a liftoff to deposit 120 nm of Au pads along the edges of our chips for heat sinking

Step	Layer	Photoresist	Laser (nm)	Dosage (mJ/cm^2)
2	Al KIDs	AZ 1512	375	120
4,10	Nb CPW/ground plane	AZ 703	375	185
7	Backside SiO2 alignment cross	AZ 703	375	220
8	SiN_x vias	AZ 703	375	185
11	SiN_x over KIDs/OMT	AZ 1512	375	110
12,13	Gold liftoff, Frontside Si	AZ 1518	375	200
15	OMT and KID membranes DRIE	AZ 4620	405	600

Table 4.1: Lithography details for fabrication of detector wafer. Step number matches the process step shown in Figure 4.2.

Step	Recipe	ICP Pow. (W)	Bias Pow. (W)	Pres. (mTorr)	He Pres. (Torr)	Gas 1 flow (sccm)	Gas 2 flow (sccm)	Gas 3 flow (sccm)
4,10	Nb etch	600	50	50	5	CF_4, 40	CHF_3, 10	Ar, 10
5	SiN_x dep	1200	1	10	5	SiH_4, 25	N_2, 30	Ar, 10
6	SiO_x dep	800	200	10	5	SiH_4, 20	O_2, 50	Ar, 30
7	SiO_x etch	800	200	5	4	O_2, 45	-	-
8,11	SiN_x etch	100	20	30	5	SF_6, 20	-	-

Table 4.2: Recipes used for chemical vapor deposition and plasma etch. Step number matches the processes shown in Figure 4.2.

(step 12). We also pattern and etch the 4 µm of device Si layer down to the oxide layer to form the dicing lines of our detector (step 13). Fig. 4.1 shows images from an optical microscope of the detector after the front-side processing.

The most delicate part of our detector fabrication is releasing the OMT and KID membranes. We do so by first bonding our detector wafer *detector side down* onto a carrier Si wafer by wax bonding (step 14). The carrier wafer is necessary to physically support the membrane during the DRIE process. We pattern the backside of our detector wafer to form holes for the OMT and KIDs membranes as well as the outlines of the device chip for release from the wax wafer. To etch the backside of the wafer, we first use a buffered hydrofluoric (HF) bath to remove the 2 µm of SiO_x (step 15). Then we use a deep reactive ion etcher (DRIE)[6] to deep etch the bottom layer of 450 µm of Si down to the 0.5 µm of oxide of the

6. Plasma-Therm Versaline DSE: http://www.plasma-therm.com/etch-dse.html

SOI wafer (step 16). We then remove any remaining resist with a nanostrip bath and then all the exposed oxide by another buffered HF bath (step 17) and release the individual chips from the carrier wafer using an acetone bath to dissolve the wax (step 18). A photo of a finished device is shown in Fig. 4.3.

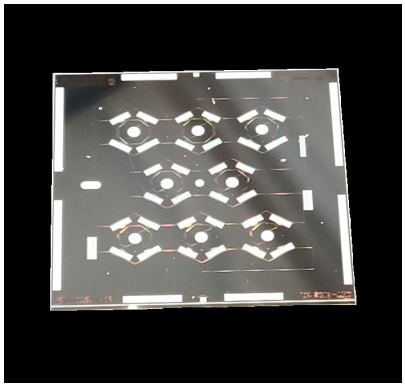

Figure 4.3: Photograph of a finished device.

During our initial fabrication run, we used a SOI wafer with 4 µm thick oxide layer. However, we observed that during the DRIE processing (step 15), the etch rate of the Si handle wafer stayed consistent until the last ∼20 µm of Si before the oxide layer. After this point, the etch rate became negligible for the remaining Si. This is likely due to charge build-up caused by the thick oxide layer just beneath the ∼20 µm thick Si layer, which repelled the ions used in the reactive ion etch. We found that by decreasing the SOI oxide layer thickness to $\lesssim$1 µm, we were able to etch completely through the handle Si layer and expose the oxide layer.

4.4 Setup

The measurement setup mostly follows the procedure described in Section 3.4. The main difference is that since optical coupling is no longer done via lenses and antennae, we use feedhorns instead as waveguide to send light to the OMT probes. Figure 4.4 depicts the feedhorn used in this our setup, which was constructed out of an Al block and then gold-plated. The horn block is aligned to our detector wafer via dowel pins and the whole assembly

is screwed down in place. We also insert small spacer chips ($\sim 300\,\mu$m thick) between the horn and the detector chip to prevent any physical contact and abrasion.

For the setup used to measure data described in Section 4.5, we tested a 220 GHz chip. We used a 12 icm K filter mounted on the 1 K stage, between the blackbody and the feedhorn-detector assembly. Additionally, we installed a 10 icm low pass filter and a 150 GHz high pass filter at the opening of the feedhorn block. Although the low pass filter should be redundant with the feedhorn, it was installed as an extra precautionary step.

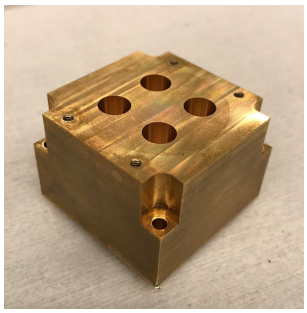

Figure 4.4: Feedhorn used in the OMTKID optical setup.

4.5 Optical Results

Figure 4.5 shows the optical response (fractional frequency shift) of the OMTKID array. KID 0-8 are optical KIDs connected to OMT probes via the Nb microstrip. KIDs 9-11 are dark KIDs that are not coupled to any OMT or microstrip structures. The response of the optical KIDs vary due to the different geometry designs of the KIDs, but overall, the optical response is on par with the results shown in Figure 3.13. More interestingly, although there are slight variations of the frequency shift in the dark KIDs with temperature, likely due to things such as the temperature drift of the mixing chamber stage, the response of the dark KIDs to optical power is overall flat. This is in great contrast to Figure 3.13, where the dark KID response was $\sim 35\%$ of the optical response.

The results are highly suggestive that the stray light pick up we saw in the previous chapter was due to light coupling in through the silicon wafer. Since we etched out the Si

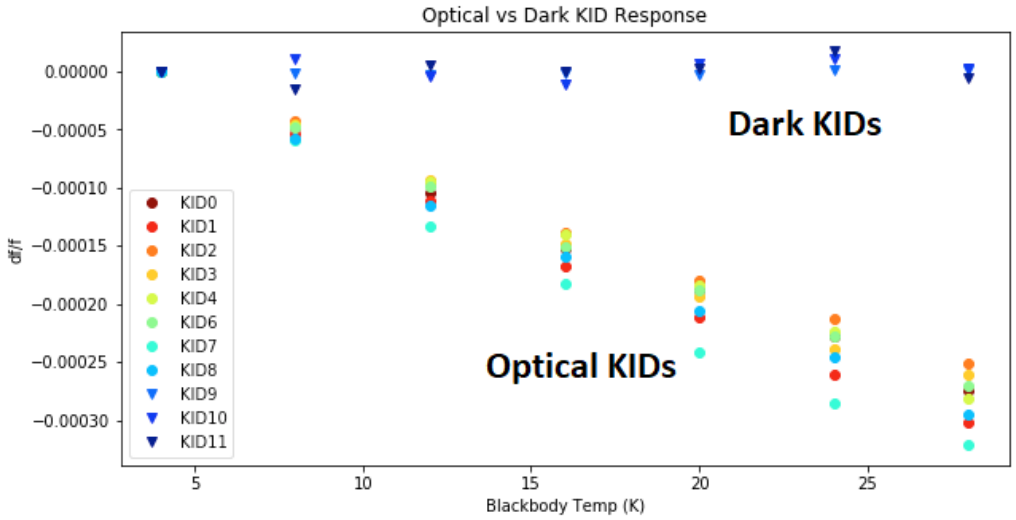

Figure 4.5: Comparison of the optical vs dark KID response on the OMTKID array.

from underneath the OMT probes, this ensures all the light is only coupled via the OMT probes and microstrip. The feedhorns also ensure light will only reach the OMT probes and not other parts of the wafer.

4.6 Summary and Future Work

We have described the development of a prototype OMT-coupled KIDs array for the 220/270 GHz band. The process is compatible with dual-polarization, mutli-chroic pixels. Preliminary optical results show the device is not seeing any stray light pick up that was present in the antenna-coupled KID array described in the previous chapter.

There are several challenges with this design, namely the fabrication process is quite long and prone to failure. We did not achieve very good yield on the prototype device, with the detector yield $< 50\%$. Subsequent iterations of this design will require more development in the fabrication processes with better tolerances and more work needs to be done to understand the polarization detection capabilities. Nonetheless, this prototype is a promising candidate for future mm-wave observations.

CHAPTER 5

CHARACTERIZING MM-WAVE EMISSIONS FROM OPTICALLY SELECTED GALAXIES

5.1 Introduction

Historically, most of the observable light in the universe was assumed to be emitted at the optical and UV wavelengths. However, data from the COBE satellite showed that the universe had about an equal energy output at the infrared and the sub-mm wave frequencies as the optical and UV frequencies, which became known as the cosmic infrared background (CIB) (Puget et al., 1996).

A large fraction of the CIB is emitted by the dusty distant galaxies. In early galaxies where most star formation occurred, UV light from stars is absorbed by surrounding dust and gas and reemitted in the infrared wavelengths, which is then redshifted to the millimeter wavelengths as it travels to Earth. Due to dust obscuration, these galaxies, known as dusty star-forming galaxies (DSFGs) or sub-mm galaxies (SMGs), are often only observable in the infrared and sub-mm band. DSFGs are some of the oldest and farthest galaxies in our universe and have extremely high star formation rates. Surveys from the *Spitzer Space Telescope* and *Herschel Space Observatory* as well as observations from ground-based telescopes like the South Pole Telescope (SPT) have catalogued millions of these galaxies. Observations of these galaxies are extremely important since they serve as a probe for early star formation. However, while most of the contribution to the CIB is thought to come from DSFGs, but the link between DSFGs and galaxies observed in the optical band and how much the CIB can be resolved from optical sources alone are still unclear.

Unfortunately, unlike the optical and UV observations, the beams of single-dish telescopes observing in the mm-wave are much bigger than the angular separation between sources. The density of sources causes the sky observation to be "confusion-limited", rendering it unable to resolve individual galaxies. One way to overcome this barrier in analyzing mm-wave maps

is a method known as stacking. In stacking, we average the flux of pixels corresponding to known galaxy locations in the mm-wave map. With a well-selected large set of galaxies, the noise should be significantly reduced after averaging, while the signal coherently adds up.

Several studies have successfully used stacking in the infrared and far-infrared wavelengths to resolve sources, as seen in Béthermin et al. (2012) and Oliver et al. (2012) with *Herschel* data, Marsden et al. (2009), Devlin et al. (2009), and Pascale et al. (2009) with Balloon-borne Large-Aperture Submillimeter Telescope (BLAST, Pascale et al. (2008)) data, and Millard et al. (2020) with S2COSMOS data. This analysis is especially powerful for stacking data in multiple wavelengths to construct a spectral energy density (SED), as seen in Viero et al. (2013a) and Béthermin et al. (2015). In particular, Viero et al. (2013a) was able to resolve between 45-80% of the CIB with their galaxy catalog ($\sim$80000 K-selected sources) at wavelengths ranging 24-1100 µm using *Spitzer*, *Herschel*, and AzTEC data. Furthermore, Duivenvoorden et al. (2020) refined the SIMSTACK algorithm used in Viero et al. (2013a) to fit to foregrounds and flux leakage from masked galaxies in addition to the galaxies themselves, using the COSMOS galaxy catalog for the *Herschel* maps. With this refinement, the CIB contribution was measured to be 10.5 ± 1.6, 6.7 ± 1.5 and 3.1 ± 0.7 nWm^{-2}sr^{-1} at 250, 350 and 500 µm, respectively. This was in agreement with the FIRAS measurements.

In this study, we extend these analyses to longer wavelength (3mm) by looking at stacking *Herschel* and SPT maps. Section 5.2 describes the datasets used in the analysis. Section 5.3 describes the data reduction and fitting procedures. All magnitudes are quoted in the AB system.

5.2 Data

5.2.1 Stellar Mass Catalog

We construct a stellar mass sample for mm- and sub-mm wavelength characterization making use of optical and infrared galaxies from the *Spitzer* South Pole Telescope Deep Field (Ashby

et al., 2013, SSDF) and the second data release (DR2) of the Dark Energy Survey (DES Collaboration et al., 2021, DES). In this subsection we describe our matching between these two datasets to produce a joint infrared-optical galaxy catalog and our estimation of both photometric redshifts and stellar masses for these galaxies.

As detailed in Ashby et al. (2013), the SSDF is a 94 deg^2 two-band infrared survey by the *Spitzer*/IRAC camera. The survey field (centered at RA=23hr30min,DEC=-55deg) was chosen to overlap with deep data from both the SPT-SZ (Carlstrom et al., 2011) and SPTpol experiments (Austermann et al., 2012) as well as far-infrared observations from *Herschel*/SPIRE and the survey reached 5σ depths of $\sim$21.8 and 21.5 magnitudes in the IRAC 3.6 and 4.6 μm bands, respectively. We select sources with `MAG_AUTO` signal-to-noise > 4 and SourceExtractor flags less than 4 in both bands (the latter cut removes corrupted or saturated photometry), resulting in a catalog of 2.5×10^6 sources. As the infrared *Spitzer* bands are excellent tracers of stellar mass, we adopt this catalog as our base source catalog to which we will match the optical photometry from the DES.

The DES is a galaxy survey in the visible and near-infrared wavelengths which was undertaken to improve our understanding the nature of dark energy and the expansion of the universe (The Dark Energy Survey Collaboration, 2005). The six year survey was conducted with the 570 Mega-pixel camera DECam imager (Flaugher et al., 2015) installed on the Blanco Telescope at the Cerro Tololo Inter-American Observatory (CTIO). From the DES DR2 release we make use of the *griz*-band dereddened `MAG_AUTO` magnitudes for galaxies with `MAG_AUTO_I_DERED`< 25 and SourceExtractor flags less than 4. As reported in DES Collaboration et al. (2021), the typical 10σ `MAG_AUTO` detection threshold is 24, 23.8, 23.1, and 22.3 for the *griz*-bands, respectively. We associate DES and *Spitzer* sources using the closest match within 1 arcsecond (with each infrared and optical source only allowed one match); the median separation for matched sources is 0.3 arcseconds. For infrared sources without an optical counterpart, we conservatively place an upper limit on the optical magnitudes at 0.5 magnitudes brighter than the corresponding peaks ($\sim$ 85% completeness

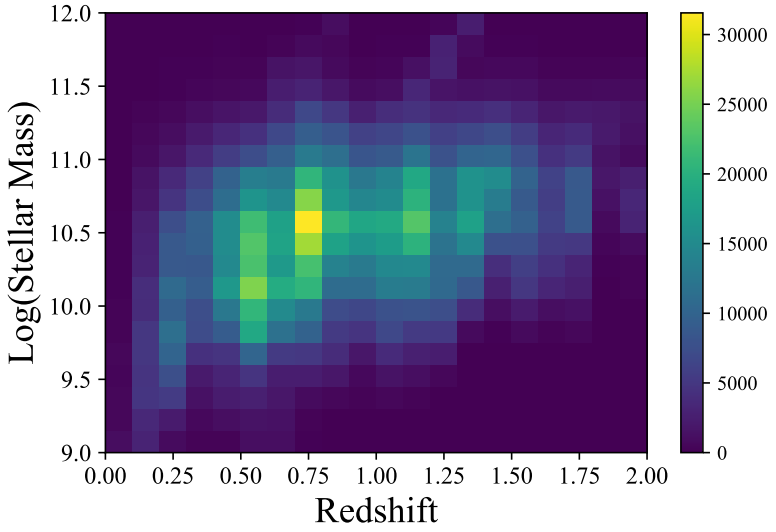

Figure 5.1: The distribution of galaxies as a function of photometric redshift and stellar mass.

threshold) in the histograms of optical source magnitudes in the SSDF region. Following DES Collaboration et al. (2021), we make use of the `SPREAD_MODEL` i-band morphological measure `EXTENDED_COADD` < 1 for sources at $i < 22.5$ to remove stars from our sample[1]; in total this cut removes 3.4×10^5 sources from our sample leaving us with 1.8×10^6 galaxies with optical and infrared photometry and 4.2×10^5 galaxies with solely two-band infrared photometry.

We estimate photometric redshifts using the `Le PHARE` photometric redshift estimation code (Arnouts et al., 1999; Ilbert et al., 2006). For our templates we make use of the 32 galaxy SEDS from (Ilbert et al., 2009). Once we have estimated a photometric redshift for each galaxy, we estimate its stellar mass using `FAST` (Kriek et al., 2009). The estimated redshift and stellar mass distribution of our sample is shown in Figure 5.1 and the galaxy density distribution across the field in Figure 5.2.

1. While at fainter magnitudes the morphological star-galaxy separation becomes less robust, we do perform systematic checks with fainter star-galaxies thresholds, see Section DO THIS.

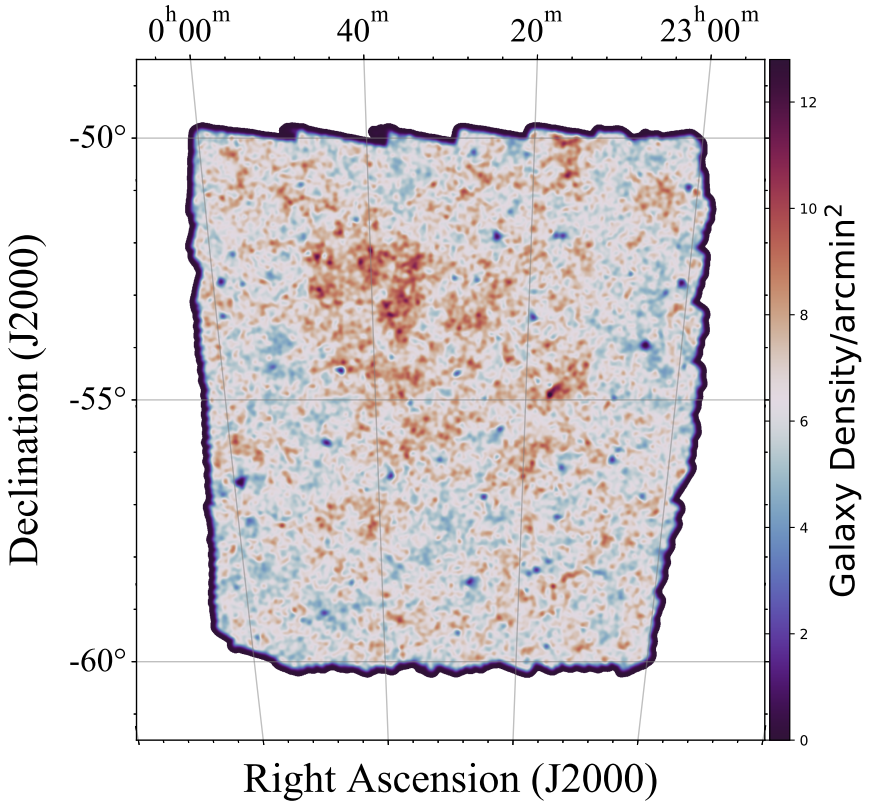

Figure 5.2: Galaxy density of the SSDF-DES stellar mass catalog used in this work. Density smoothed by 5' Gaussian beam for display purposes. The regions with the lowest densities reside in the vicinity of bright stars which are accounted for in our galaxy survey mask.

5.2.2 Herschel/SPIRE

The *Herschel Space Observatory* was a far-infrared and sub-millimetre telescope built by the European Space Agency and was operated from 2009 to 2013. We used the data from the Spectral and Photometric Imaging Receiver (SPIRE) camera on the telescope (Griffin et al. (2010)), which took data on three frequency bands centred on 250, 350, and 500 µm.

The SPIRE maps used in this analysis followed the same treatment as described in Viero et al. (2019) and Holder et al. (2013), which is briefly summarized as follows. The 100 $\deg^2$ map is constructed from a mosaic of twelve 10×3.3 deg scans. The data is then reduced using ESA's Herschel Interactive Processing Environment (HIPE) software and SMAP/SHIM for noise removal (Levenson et al. (2010), Viero et al. (2013b)). The two sets of maps were made for Viero et al. (2019) with both a 15" pixel size and a 30" pixel size, but in this analysis we only used the 15" pixel size map. We project the *Herschel* maps into the same Sanson-Flamsteed projection as the SPT maps.

The SPIRE maps have a beam of full width at half maximum (FWHM) of 18.1", 25.5", and 36.6" with noise levels of 2.8, 4.0, and 5.6 mJy-arcmin at 250, 350, and 500 µm respectively. The beams were estimated with a calibration measurement map of Neptune, which effectively acted as a point source for SPIRE.

5.2.3 SPT-SZ/SPTPol

The South Pole Telescope (Carlstrom et al., 2011) is a 10 meter dish telescope operating in the sub-mm/mm-wave regime located in Antarctica. The first camera was deployed in 2007 and was named SPT-SZ due to one of its main priorities of detecting galaxy clusters via the Sunyaev-Zel'dovich (SZ) effect (Sunyaev & Zeldovich, 1972). The 960-pixel array was used to observe light over three frequency bands: 95, 150, and 220 GHz. The full survey (Story et al., 2013) covered an area of 2540 $\deg^2$ on the sky. For this analysis, we use a roughly 10

$\times 10$

$-sized patch centred at 23^{\mathrm{h}}30^{\mathrm{m}}, -55^{\mathrm{d}}00^{\mathrm{m}}$. The SPT-SZ beams have a FWHM of 1.65, 1.2,

and 1.0 arcminutes at 95, 150, and 220 GHz respectively. The noise levels are 40, 17, and 80 µK·arcmin for the 95, 150, and 220 GHz maps respectively.

In 2012, SPT installed its second camera known as SPTpol. SPTpol had 780 detectors observing at 95 GHz and 150 GHz. These detectors were more sensitive than their predecessors and could also detect polarization, which allowed the first detection of lensing B-mode (Hanson et al., 2013). The final maps have a noise level of 11.8 µK·arcmin at 95 GHz and 5.6 µK·arcmin at 150 GHz.

To take advantage of the lower noise levels in the SPTpol maps, we use the SPTpol 95 and 150 GHz maps with the SPT-SZ 220 GHz maps. In this work, we use a cutout from the SPTpol 500 $\deg^2$ survey map (Henning et al., 2018) to match the 100 $\deg^2$ SPT-SZ field described above. Using the SPTpol data will significantly reduce the noise in the 95 and 150 GHz maps. The SPT-SZ 220 GHz map and point sources used in this analysis are described in Bleem et al. (2021) in more detail. Data reduction is done by filtering the time-ordered data of each detector response, coadding all detector responses for each single observation, and then coadding all the observations for a given field. The SPTpol maps follow similar data processing. An optimal filter is constructed to extract point sources from the map (see 5.2.5 for more details on this process). The full catalog was made by combining data from all three frequencies.

5.2.4 Data Processing

This section describes the data processing methods for making point source filtered maps, which is visually summarized in Figure 5.3

Making maps

The following is a brief overview of the SPT map-making procedure. For more details, please refer to Schaffer et al. (2011). Maps are made from the time-ordered data from bolometers for each scan observation of the sky. The first processing step is to apply a selection cut

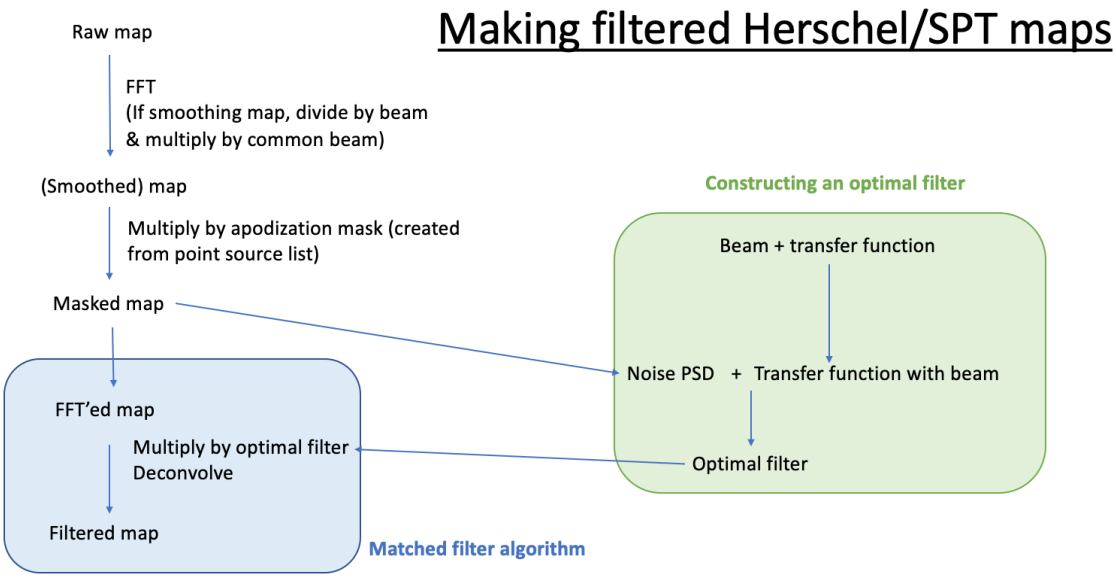

Figure 5.3: Work flow diagram of making filtered maps for SPT and *Herschel*. The map is first masked and the matched filter is calculated using properties of the map and source profile. Then the masked map is convolved with the matched filter to make filtered maps.

to the data based on noise and response properties of each detector. A filtering process is done to remove the effects of the pulse-tube cooler. To remove the atmospheric noise, a low-order polynomial is fitted and subtracted from the time-stream, which effectively results in a high-pass filter at $\ell = 300$ (for SPTpol maps) and $\ell = 200$ (for SPT-SZ 220 GHz map) in the scan direction. A low-pass filter at $\ell = 15000$ (for SPTpol maps) and $\ell \sim 20000$ (for SPT-SZ 220 GHz map) is done to remove high frequency noise aliasing when the data is binned into map pixels.

For each observation, the detector data is projected into pixels using the telescope's pointing model, weighted by the inverse noise variance. The SPT maps are constructed using the Sanson-Flamsteed projection (Calabretta & Greisen, 2002) with a pixel resolution of 0.25 arcmin. The individual observation maps are then coadded with weights determined by the average detector noise for each observation.

Point source and apodization masking

The sharp borders of the maps can cause issues when transforming into Fourier space and back into real space. These sharp borders can be softened by applying an apodization mask, also known as a sky window function. In this analysis, we apply a 3-arcminute cosine to the border to obtain a border apodization mask for the *Herschel* maps. For the SPT maps, we use previously constructed apodization masks (e.g., see Story et al. (2013))We also create a point source apodization mask with sources detected above 5.0 sigma in the 150 GHz band masked with a 5-arcminute radius circle. Similarly to the apodization mask, the edges of the masking circles are smoothed by a cosine.

Transfer function and beam response

The SPT-SZ and SPTpol sky maps described in Section 5.2.4 encode not only the sky signal, but also the instruments' beam responses and additional filtering processes applied to the maps. The SPT instrument beam can be approximated as a Gaussian with a FWHM of 1.65', 1.2', and 1.0' for the 95, 150, and 220 GHz bands. However, the exact shape of the beams is calculated by using data from emissive sources in the survey fields and dedicated planet observations, as described in Schaffer et al. (2011). The effect of the data processing can be reconstructed by making a transfer function. As we are focused on galaxy scale features, this can be well modeled by performing "mock observations" on a simulated sky map of a 0'75 Gaussian beam, using the method described in Bleem et al. (2021). The time-ordered data is processed in the same process as the real bolometer data described in Section 5.2.4, and the individual processed mock observation maps are coadded using the same weighting. The transfer function is then calculated as the ratio of the 2D power spectrum of this coadded map to the input power spectrum of the simulated sky map.

For the *Herschel* maps, we instead generate our own transfer function used for the match filter algorithm. We first set two variables, l_{highpass} and l_{lowpass}, at which point the transfer function rolls off for lower and higher *ell*s respectively. For our *Herschel* maps, this ends up

being $l_{\rm highpass} = 10$ and $l_{\rm lowpass} = 25000$. We then create the 1D transfer function, $TF_{\rm 1D}$, using the formula:

$$F(l) = \exp\left(-\left(\frac{l_{\rm highpass}}{l}\right)^6\right) \exp\left(-\left(\frac{l}{l_{\rm lowpass}}\right)^6\right) \tag{5.1}$$

where *ell* is the *ell* values along k_x. The 2D transfer function, $F(k_x k_y)$, is made by tiling this 1D function along k_y.

We then fold in the beam into the transfer function to make the total response function by multiplying the 2D beam grid by the transfer function. The 2D beam, $B(k_x, k_y)$, is generated from *Herschel*'s 1D beam response assuming azimuthal symmetry. We create a 2D *ell*-grid based on the resolution and size of the map and interpolate the beam at each ℓ value.

Noise PSD

For SPT maps, the noise PSD was estimated using a resampling technique described in Bleem et al. (2021) and previous SPT works. Individual observations are randomly assigned ± 1 and coadded. The resulting map can be considered as pure noise since the sky signal in each observations are highly suppressed. The PSD for each coadded noise map is computed and the final noise PSD is calculated by taking the average of jackknife of these PSDs. For *Herschel* maps, we use the FFT of the map itself as the noise PSD.

5.2.5 Matched Filter Algorithm

In both the SPT and *Herschel* maps, scale-dependent noise fluctuations can lower the sensitivity to those signals. To optimize the signal-to-noise of our desired signals, we multiply the map in Fourier space with an optimal filter to specifically look for galaxies, which are effectively point sources. This algorithm is described in more detail in e.g, Everett et al. (2020).

The optimal filter can be calculated as:

$$\psi(k_x, k_y) = \frac{\tau(k_x, k_y) N^{-1}(k_x, k_y)}{\tau^2(k_x, k_y) N^{-1}(k_x, k_y) dk_x dk_y} \tag{5.2}$$

where $N(k_x, k_y)$ is the noise covariance matrix, taking into account the pixel noise and any unwanted sky signal like the CMB, and $\tau(k_x, k_y)$ is source shape in Fourier space, which is determined by the source profile convolved with the beam and the transfer function, i.e. all the filtering done to the time-ordered data in map-domain described in Section 5.2.4.

Noise spectrum

In order to make the noise spectrum needed for the matched filter algorithm, we feed in a 1D unwanted sky signal spectrum across the *ell* range of interest. In the case of SPT maps, we feed in the CIB covariance matrix numbers from Reichardt et al. (2021) as well as the CMB spectrum. For *Herschel* maps, we set this to zero since we do not expect any significant unwanted sky signal in the *Herschel* frequency bands. Although the CIB is quite prominent in *Herschel* maps, we already take this into account by taking the FFT of the *Herschel* maps and using that as the noise PSD.

We construct our initial 2D noise power spectrum by multiplying the unwanted 2D sky signal spectrum ($P(k_x, k_y)$) by the square of the transfer function and beam calculated above, and adding the square of the pixel noise PSD, N_{pix},

$$N^2 = P(k_x, k_y) * |F(k_x, k_y) * B(k_x, k_y)|^2 + N_{pix}^2 \tag{5.3}$$

.

Filter construction

The last ingredient needed to construct the optimal filter is the source profile $S(k_x, k_y)$. In this analysis, we treat the galaxies in the maps as point sources, so the source profiles are

simply delta functions.

Thus, we can calculate $\tau(k_x, k_y)$ simply as

$$\begin{aligned} \tau(k_x, k_y) &= S(k_x, k_y) * F(k_x, k_y) * B(k_x, k_y) \\ &= F(k_x, k_y) * B(k_x, k_y) \end{aligned} \tag{5.4}$$

Then we can construct the optimal filter using Equation 5.2. A sample optimal filter for the SPTpol 150 GHz map is shown in Figure 5.4. The SPTpol 150 GHz map that has been matched filtered using this filter is shown in Figure 5.5.

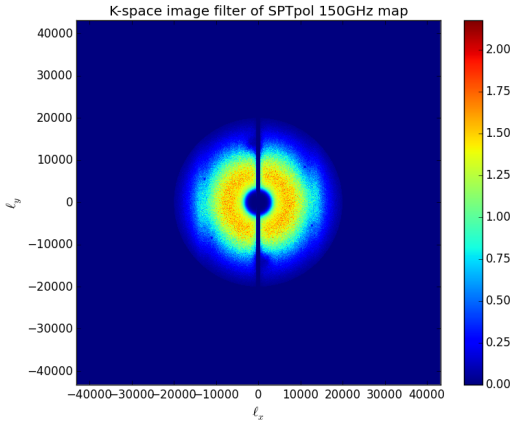

Figure 5.4: A 2D optimal filter at 150 GHz used for this analysis.

5.3 Method

This section describes the method used to create stacked galaxy SEDs and the fitting model. An overview of the SED measurement process is described in Figure 5.6 and Figure 5.7 describes the fitting method used to fit galaxy SEDs.

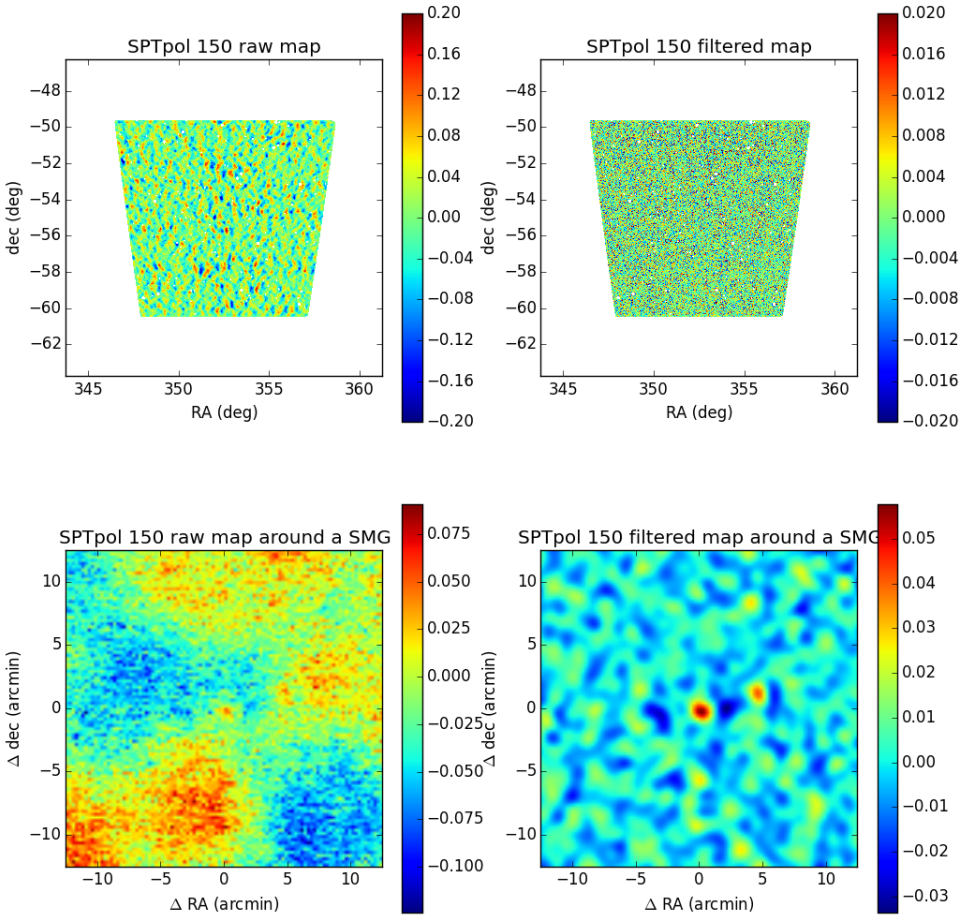

Figure 5.5: SPTpol 150 GHz raw map (top left) and the equivalent map that has been matched filtered for point sources (top right). Colour scale for both maps are modified to ignore bright sources and show the fluctuation variations. Bottom shows a 25'x25' cutout centred on a SMG. Units of all maps are expressed in temperature fluctuations (ΔT) of milliKelvin (mK).

5.3.1 SED Fitting

We follow a similar SED fitting function as described in Viero et al. (2013a). The modified function of the blackbody can be described by

$$S_{\nu,BB} = A\nu^{\beta}B(\nu,T) \tag{5.5}$$

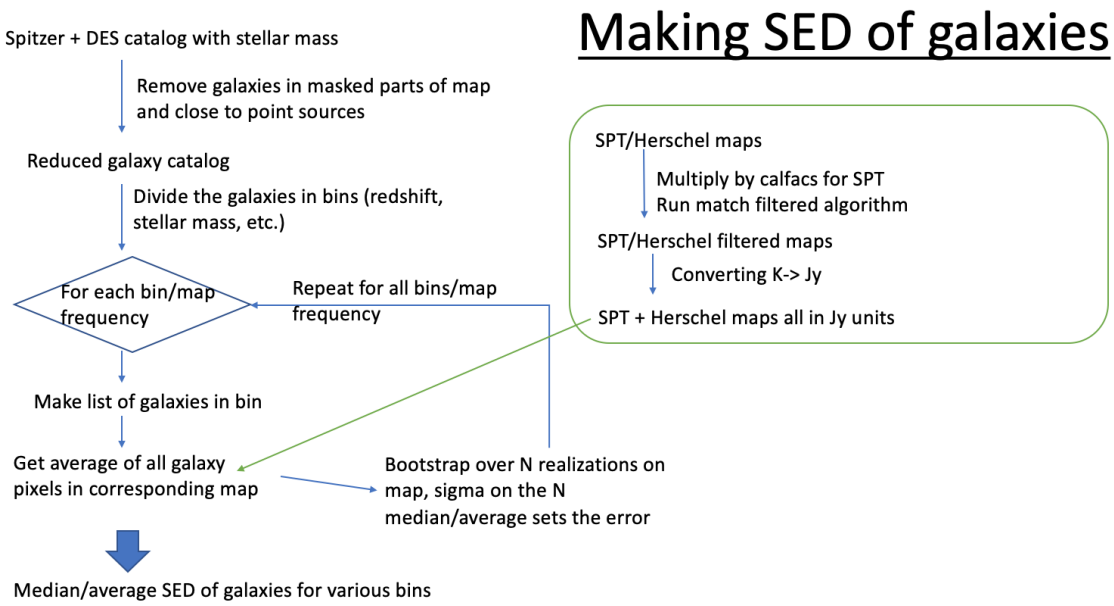

Figure 5.6: Work flow diagram of making stacked galaxy SEDs. First, galaxies are divided into different redshift and stellar mass bins. For each bin, all the galaxy fluxes are averaged for every filtered map. Errors are estimated by using bootstrap over 100 realizations of the galaxy samples in the bin.

where A is the overall amplitude parameter, β is the power dependency of the frequency (ν) scaling, which varies between 1.5 and 2, and $B(\nu, T) = (2h\nu^3/c^2)/(e^{h\upsilon/k_BT} - 1)$ is the Planck blackbody equation. We set $\nu = \nu_{eff}(1 + z)$ to take redshifting into account, where ν_{eff} is the effective frequency discussed in 5.3.2. Since β is degenerate with z, we set $\beta = 2$, similarly to Viero et al. (2013a).

We also include the thermal-SZ spectrum as part of fitting function. From (Sunyaev & Zeldovich, 1972), the temperature distortion of the CMB from tSZ can be described by

$$\frac{\Delta T_{CMB}}{T_{CMB}} = f_{SZ}(x) \int n_e \frac{k_B T_e}{m_e c^2} \sigma_T dl = f_{SZ}(x) y_{SZ} \tag{5.6}$$

where $x = h\nu/k_BT_{CMB}$, n_e the electron density, T_e is the electron temperature,σ_T is the Thomson cross-section, and $f_{SZ}(x)$ is non-relativistic the frequency dependence of the tSZ effect compared to the spectrum of fluctuations of a 2.73K blackbody, which can be calculated

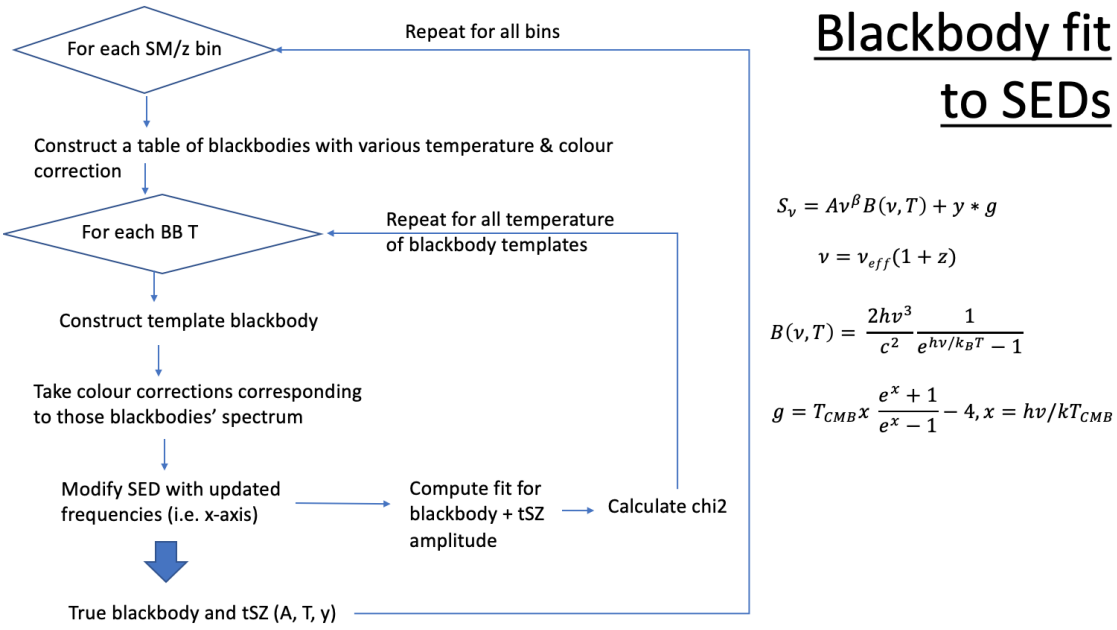

Figure 5.7: Work flow diagram of fitting method to the stacked galaxy SEDs. Due to computation constraints, we compute beforehand the effective frequencies a table of different blackbody temperatures and redshifts, effectively creating a lookup table of template blackbodies. The algorithm iteratively fits each template blackbody to the stacked SED data and fits for the amplitude of the dust and tSZ component and the χ^2 value is calculated. The best fit model corresponds to the blackbody template with the smallest χ^2 value.

as

$$f_{SZ} = \left(x\frac{e^x+1}{e^x-1} - 4\right) \tag{5.7}$$

(see Wright (1979), Nozawa et al. (2000), Chluba et al. (2012)).

In total, we fit for 3 parameters: A, T, and $y_{\rm SZ}$. The full model can then be described as

$$\begin{aligned} S_\nu &= S_{\nu,BB} + S_{\nu,tSZ} \\ &= A\nu^\beta \frac{2h\nu^3/c^2}{e^{h\nu/k_BT}-1} + y_{\rm SZ}\left(x\frac{e^x+1}{e^x-1} - 4\right)\Delta T_{CMB} C_{K-Jy} \end{aligned} \tag{5.8}$$

where C_{K-Jy} is the flux conversion factor from Kelvin to Jansky (see 5.3.3). Figure 5.8 shows an example of the two component fitting on a set of 24 stacked SPTpol galaxy clusters. The fit does not match very well, but this can be explained by the fact we did not account for

the SZ selection in these galaxies. We expect the tSZ component to be much lower for the galaxies in our catalog.

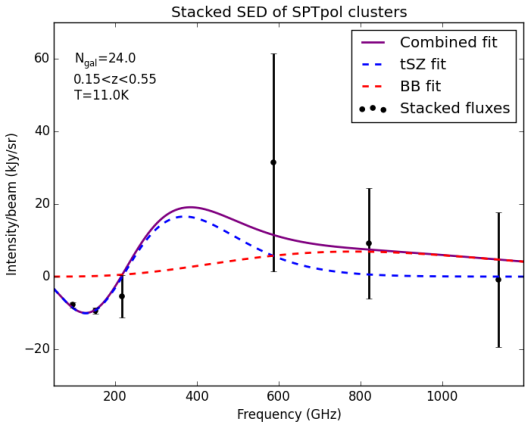

Figure 5.8: SED composed of stacked fluxes of 24 SPTpol galaxy clusters in the redshift of $0.15 < z < 0.55$. Errorbars are calculated using the bootstrap method over 50 realizations. The lack of fitting at 220 GHz band may come from not accounting for the SZ selection in this sample.

5.3.2 Effective Frequency Bands

Since the bandpasses of *Herschel*, SPT-SZ, and SPTpol have a distinct spectral shape, the "effective" frequency observed depends on both the telescope's transmission response t_ν and the source spectrum I_ν. The source spectrum is the modified blackbody or thermal SZ described in Section 5.3.1. This effective frequency can be calculated by integrating the product of the transmission response with the source spectrum, and the transmission response with the partial derivative of the CMB spectrum with respects to temperature (B'_ν). We then take the ratio of these two integrals and compare it to the ratio of I_ν to B'_ν. The effective frequency is where these two ratios are the closest in value. This can be summarized by making sure the effective frequency, ν_{eff}, satisfies the following equation

$$\Delta T_s = \frac{I_\nu(\nu_{eff})}{B'_\nu(\nu_eff)} = \frac{\int I_\nu t_\nu d\nu}{\int B'_\nu t_\nu d\nu} \tag{5.9}$$

where ΔT_s is temperature of the source calibrated against the CMB temperature at the same frequency band.

We can calculate the effective frequencies for the case of tSZ source spectrum (see Equation 5.7). For the SPTpol and SPT-SZ bands, we obtain an effective frequency of 95.9, 148.5, and 220.0 GHz for the SPTpol 95 and 150 GHz and SPT-SZ 220 GHz band respectively. For the *Herschel* bands, we obtain 1076.4630, 804.72065, 560.62342, for the 250, 350, and 500 µm bands (or 1200, 857, and 600 GHz bands).

5.3.3 K-to-Jy Conversion

SPT-SZ and SPTpol maps are usually made in units of fluctuations of the CMB (Kelvin). However, it is often useful to measure sky sources in units Jansky (Jy) or milliJansky (mJy), which is a unit of spectral flux density where 1 Jansky = 10^{-26} W/m^2·Hz.

As described in Mocanu et al. (2013), we can determine the flux of the point sources by taking the temperature fluctuation of the brightest pixel associated with the source ($T_{\rm peak}$) and converting it to units of Jansky via

$$S[\mathrm{Jy}] = T_{\rm peak}[\mathrm{K}] \cdot \Delta\Omega_f \cdot 10^{26} \frac{2k_B}{c^2} \left(\frac{k_B T_{\rm CMB}}{h}\right)^2 \frac{x^4 e^x}{(e^x-1)^2} \tag{5.10}$$

where $x = h\nu/k_B T_{\rm CMB}$ and $\Delta\Omega_f$ is the effective solid angle under the source template and can be calculated as

$$\Delta\Omega_f = \left[\int d^2k \psi(k_x, k_y)\tau(k_x, k_y)\right]^{-1} \tag{5.11}$$

The solid angles for SPTpol 95 and 150 GHz map are calculated to be 3.98×10^{-7} sr and 1.83×10^{-7} sr. For the SPT-SZ 220 GHz map, this was calculated to be 1.21×10^{-7} sr. The corresponding K-to-Jy conversion factors are 87.93 Jy/K, 72.90 Jy/K, and 58.36 Jy/K for the SPTpol 95 and 150 GHz and SPT-SZ 220 GHz maps.

5.4 Results

5.4.1 Stacking

We first identify galaxies within a bin of interest by imposing redshift and stellar mass cuts. We take the mean of all the fluxes from the selected galaxies for every map, each corresponding to a single point on the stacked galaxy SED. To estimate the error, we perform the bootstrap method on the galaxy sample over 100 realizations, taking the mean for each re-sample. The error is calculated by taking the median absolute deviation of the 100 means.

Figure 5.9 shows a table of SEDs from stacking galaxy fluxes using the method described in Section 5.4.1 along with its best fit. The galaxies are divided in redshift from $z = 0$ to $z = 2$ with bin width of 0.5. The stellar mass bins vary from $\log(M/M_{\odot}) = 9$ to $\log(M/M_{\odot}) = 12$ in increments of 0.5. The temperature of the best-fit to Equation 5.8 and the number of galaxies in each bin are also shown in each plot. To maintain statistical significance, SEDs for bins where the number of galaxies is less than 10 are not shown. The signal to noise (S/N) and strength of the signal of interest of the stacked fluxes scale with the map beam size and noise fluctuations, with the S/N from *Herschel* maps being typically a few factors higher than that from SPT maps.

Figure 5.10 depicts variations of temperature obtained from the fit to different redshift (left) and stellar mass bins (right). A strong correlation between the dust temperature and redshift can be seen across different stellar masses. This is expected since star formation increases from $z = 0$ to $z = 2.5$ and star formation and dust temperatures are strongly correlated (Magnelli et al., 2014). The correlation between dust temperature and stellar masses is significantly weaker. However, a slight increase in dust temperature with stellar masses can be seen across different redshifts. This is supported by models such as the one described in Imara et al. (2018), where it is shown that the dust temperature is expected to increase between $\log(M/M_{\odot}) = 9.0 - 12.0$ for $z = 0 - 2$.

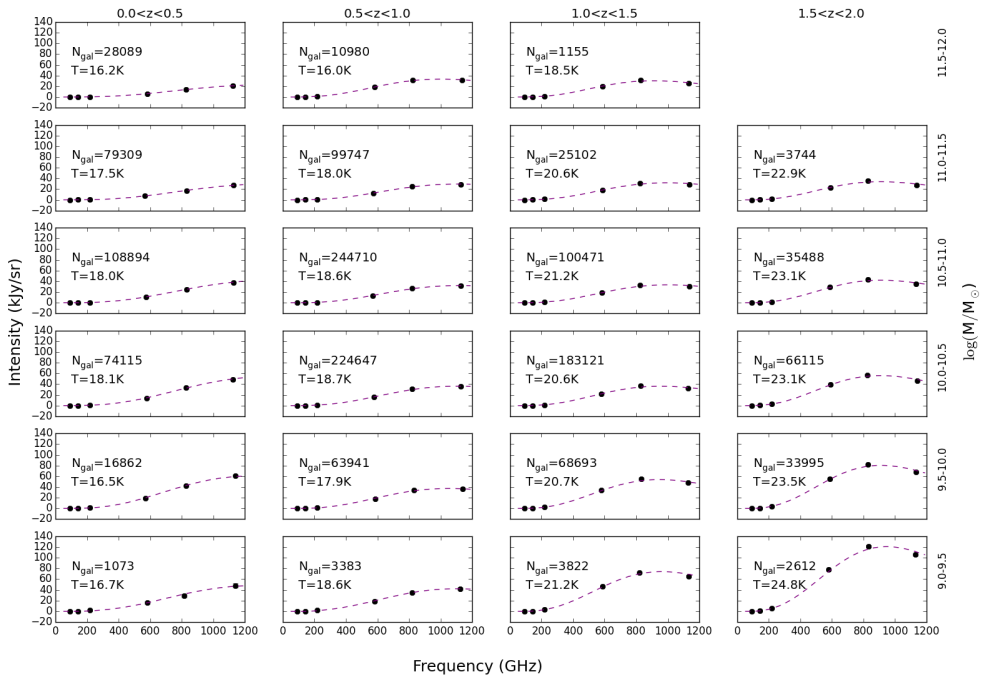

Figure 5.9: Stacked galaxy fluxes (black dots) divided into redshift bins (columns) and stellar mass bins (row) along with its best SED fit (purple dashed line). The errorbars are within the size of the dots (roughly ± 0.1 K). The number of objects in each bin and the dust temperature obtained from fitting are also shown.

5.4.2 Quiescent Galaxies

The tSZ is proportional to the total pressure along the line of sight since it is proportional to the electron number density (n_e) and temperature. Therefore, by integrating the tSZ signal across a patch of sky, it can be used to estimate the volume integral of the pressure and therefore the thermal energy of circumgalactic medium (Meinke et al., 2021), which is critical in understanding current active galactic nuclei (AGN) feedback models. Quiescent galaxies are ideal for this type of study since the lack of star formation is thought to arise from the AGN feedback and strong tSZ signal is expected.

As a preliminary analysis, we look at the stacked galaxy fluxes and SED from a sample of 202 quiescent galaxies (Figure 5.11), which have redshifts between $z = 0.01 - 0.185$ and stellar masses between $\log(M/M_\odot) = 8.52 - 9.43$. We use the Milky Way's star formation

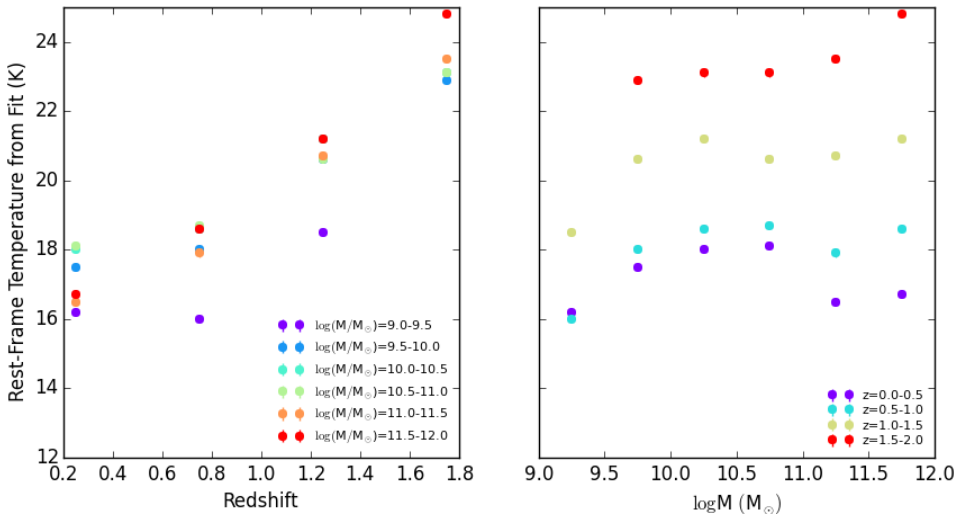

Figure 5.10: Temperatures from the best fit modified blackbody SEDs (Equation 5.8) of stacked galaxy fluxes. *Left:* Dust temperature correlation with redshift for different stellar mass bins. *Right:* Dust tmeperature correlation with stellar mass for different redshift bins. The errors for the temperature fit are roughly ± 0.1 K, which are within the size of the markers.

rate (SFR) as a metric to classify galaxies as quiescent ($\log(\mathrm{SFR}) < -11$) and star-forming ($\log(\mathrm{SFR}) > -11$), following Triani et al. (2021). However, a more complete analysis may be using the the observed bimodality in rest-frame colour, such as $U - V$ vs $V - J$ (UVJ technique) as described in Viero et al. (2013a), which would more robustly separate the two populations. We also note that tSZ contribution is notably more prominent in this sample, as seen by the negative stacked flux the SPTpol 150 GHz band. However, due to our low samples, the tSZ fit component does not match well. We expect this to be mitigated once we obtain a more complete sample of quiescent galaxies using the UVJ technique.

5.5 Next Steps and Future Work

5.5.1 Galaxy Clustering Bias

For uncorrelated sources, stacking should give an unbiased estimate of average flux (Marsden et al., 2009). However, since galaxies are often clustered, stacking can artificially bias the

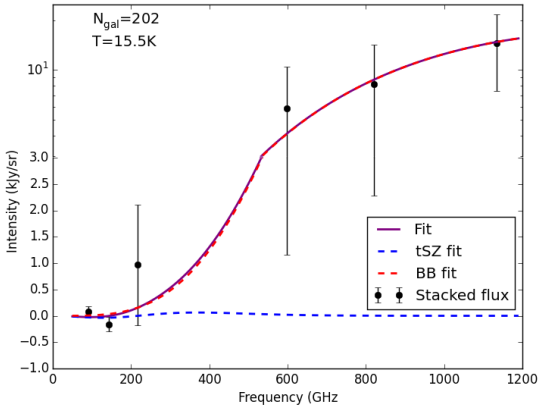

Figure 5.11: Stacked fluxes of quiescent galaxies (defined as log(SFR) < -11) along with the fit.

flux. Previous attempts to correct this bias include estimating the bias by using simulations (Béthermin et al., 2012), comparing the stacked beam width to the measured correlation function (Béthermin et al., 2012; Heinis et al., 2013), and using the median instead of the average for stacking, which would discount biases from outliers (Bourne et al., 2011). In addition, the stacked fluxes strongly depend on beam size.

Kurczynski & Gawiser (2010), Roseboom et al. (2010), and Bourne et al. (2012) independently developed a method to fit for the fluxes of multiple sources simultaneously, accounting for the bias as part of the stacking itself. Viero et al. (2013a) expanded this method to fit for the fluxes for galaxies in different redshift and mass bins, called `SIMSTACK`. In `SIMSTACK`, sources at different redshifts are assumed to be uncorrelated. For each list of sources, a map is generated with delta functions for pixels corresponding to the list of sources. The map is convolved with the instrument beam's PSF and regressed with the real map of the sky. However, Duivenvoorden et al. (2020) showed that `SIMSTACK` does not take the foreground into account nor the signals from the masked areas of the map, which leads to an underestimation of the mean fluxes. They corrected for this by allowing `SIMSTACK` to also fit for a foreground and flux leakage from masked areas of the map. The foreground is a flat term and adding the masked pixels to the list of sources.

To quantify the clustering bias, we can perform a test similar to `SIMSTACK` for our maps

which have been filtered for point sources. Like `SIMSTACK`, we first divide our galaxies into different stellar mass bins, with bin sizes varying from $\log(M/M_{\odot}) = 9$ to $\log(M/M_{\odot}) = 12$ in increments of 0.5. Within each stellar mass bin, we further divide the galaxies into different redshift bins, varying from $z = 0$ to $z = 2$ in increments of 0.5. For each subset of galaxies in the redshift bin, we create a hitmap with the delta functions for pixels corresponding to the list of galaxies in the bin. We take the FFT of the hitmap and convolve with the telescope's beam and transfer function as well as the optimal filter generated from the point source filtering algorithm described in Section 5.2.5. The maps are deconvolved back into real space to make filtered version of the hitmaps. Lastly, we can fit for the coefficients a_i for the filtered hitmaps ($M_{i,filt}$) such that

$$M_{real,filt} = \sum_{i=1}^{N} a_i M_{i,filt} \tag{5.12}$$

where $M_{real,filt}$ is the real sky map that has been match filtered. The error of this fit can be estimated via jackknife, where we divide the map into N patches. For each patch, we mask out that area on the map and calculate the variance of the distributions of coefficients of the filtered hitmaps.

We then can compare the values of a_i to the average stacked flux values from the real filtered map of the galaxies in the particular bin, which will give an estimate of the galaxy clustering bias.

5.5.2 Estimation of CIB Contribution

Following Viero et al. (2013a), we can estimate the CIB contribution in each bin by multiplying the stacked galaxy fluxes by the total number of galaxies of the bin. A study of the completeness will need to be done. This can be done by scaling the fluxes and masses of galaxies that are slightly above our brightness cutoff described in Section 5.2.1 down to the magnitude cutoff. We can then use the fraction of objects below cutoff as an estimate for

the completeness for different redshift and stellar mass bins. A full comparison of our results to previous studies will be done.

5.5.3 Galaxy Luminosity

In addition to redshift and stellar mass, we can also study galaxy luminosity of our sample. This can be done by integrating the rest-frame SED (Viero et al., 2013a). A further classification can be done by dividing the infrared galaxies into normal ($L < 10^{11} L_{\odot}$), luminous (LIRG: $L = 10^{11-12} L_{\odot}$), and ultra-luminous (ULIRG: $L > 10^{12} L_{\odot}$) galaxies. Further studies of how the galaxy luminosity varies with redshift, stellar mass, star formation rate, and dust temperature will be done, which can inform us of dust and gas content in these galaxies.

5.5.4 Other Applications

An extension of this analysis would be to model galaxy halos using CMB lensing. Large scale structures between the source and observe distorts light, resulting in shears and magnification effects in the observation. The amount of distortion can then estimate the gravitational potential along the line of sight to the source. Using a similar method described in Planck Collaboration et al. (2014), this can be done by cross correlating the *Herschel* and SPT maps with the CMB lensing map. The bulk of the CMB lensing potential comes from dark matter halos at $1 < z < 3$ (Lewis & Challinor, 2006). Since the CIB is the dominant signal in the *Herschel* bands and the population of DSFGs are expected to peak at $1 < z < 2$, we can study the correlations between distribution of dark matter (CMB lensing map), the integrated star formation history (CIB from infrared maps), and the optical galaxies in the DES catalog.

REFERENCES

Abazajian, K. N., Adshead, P., Ahmed, Z., et al. 2016, arXiv e-prints, arXiv:1610.02743. https://arxiv.org/abs/1610.02743https://arxiv.org/abs/1610.02743

Adam, R., Adane, A., Ade, P. A. R., et al. 2018, , 609, A115, doi: http://doi.org/10.1051/0004-6361/20173150310.1051/0004-6361/201731503

Ade, P., Aguirre, J., Ahmed, Z., et al. 2019, , 2019, 056, doi: http://doi.org/10.1088/1475-7516/2019/02/05610.1088/1475-7516/2019/02/056

Arnouts, S., Cristiani, S., Moscardini, L., et al. 1999, , 310, 540, doi: http://doi.org/10.1046/j.1365-8711.1999.02978.x10.1046/j.1365-8711.1999.02978.x

Ashby, M. L. N., Stanford, S. A., Brodwin, M., et al. 2013, , 209, 22, doi: http://doi.org/10.1088/0067-0049/209/2/2210.1088/0067-0049/209/2/22

Austermann, J. E., Aird, K. A., Beall, J. A., et al. 2012, in Society of Photo-Optical Instrumentation Engineers (SPIE) Conference Series, Vol. 8452, Society of Photo-Optical Instrumentation Engineers (SPIE) Conference Series, doi: http://doi.org/10.1117/12.92728610.1117/12.927286

Austermann, J. E., Beall, J. A., Bryan, S. A., et al. 2018, Journal of Low Temperature Physics, 193, 120, doi: http://doi.org/10.1007/s10909-018-1949-510.1007/s10909-018-1949-5

Bardeen, J., Cooper, L. N., & Schrieffer, J. R. 1957, Physical Review, 108, 1175, doi: http://doi.org/10.1103/PhysRev.108.117510.1103/PhysRev.108.1175

Barry, P. 2014, PhD thesis

Barry, P. S., Doyle, S., Hornsby, A. L., et al. 2018, Journal of Low Temperature Physics, 193, 176, doi: http://doi.org/10.1007/s10909-018-1943-y10.1007/s10909-018-1943-y

Baselmans, J. 2012, Journal of Low Temperature Physics, 167, 292, doi: http://doi.org/10.1007/s10909-011-0448-810.1007/s10909-011-0448-8

Baselmans, J., Yates, S. J. C., Barends, R., et al. 2008, Journal of Low Temperature Physics, 151, 524, doi: http://doi.org/10.1007/s10909-007-9684-310.1007/s10909-007-9684-3

Bennett, C. L., Halpern, M., Hinshaw, G., et al. 2003, , 148, 1, doi: http://doi.org/10.1086/37725310.1086/377253

Benson, B. A., Ade, P. A. R., Ahmed, Z., et al. 2014, in Society of Photo-Optical Instrumentation Engineers (SPIE) Conference Series, Vol. 9153, Millimeter, Submillimeter, and Far-Infrared Detectors and Instrumentation for Astronomy VII, ed. W. S. Holland & J. Zmuidzinas, 91531P, doi: http://doi.org/10.1117/12.205730510.1117/12.2057305

Béthermin, M., Le Floc'h, E., Ilbert, O., et al. 2012, , 542, A58, doi: http://doi.org/10.1051/0004-6361/20111869810.1051/0004-6361/201118698

Béthermin, M., Daddi, E., Magdis, G., et al. 2015, , 573, A113, doi: http://doi.org/10.1051/0004-6361/20142503110.1051/0004-6361/201425031

Blain, A. W., Smail, I., Ivison, R. J., Kneib, J. P., & Frayer, D. T. 2002, , 369, 111, doi: http://doi.org/10.1016/S0370-1573(02)00134-510.1016/S0370-1573(02)00134-5

Bleem, L. E., Crawford, T. M., Ansarinejad, B., et al. 2021, arXiv e-prints, arXiv:2102.05033. https://arxiv.org/abs/2102.05033https://arxiv.org/abs/2102.05033

Bourne, N., Dunne, L., Ivison, R. J., et al. 2011, , 410, 1155, doi: http://doi.org/10.1111/j.1365-2966.2010.17517.x10.1111/j.1365-2966.2010.17517.x

Bourne, N., Maddox, S. J., Dunne, L., et al. 2012, , 421, 3027, doi: http://doi.org/10.1111/j.1365-2966.2012.20528.x10.1111/j.1365-2966.2012.20528.x

Calabretta, M. R., & Greisen, E. W. 2002, , 395, 1077, doi: http://doi.org/10.1051/0004-6361:2002132710.1051/0004-6361:20021327

Carlstrom, J. E., Ade, P. A. R., Aird, K. A., et al. 2011, , 123, 568, doi: http://doi.org/10.1086/65987910.1086/659879

Casey, C. M., Narayanan, D., & Cooray, A. 2014, , 541, 45, doi: http://doi.org/10.1016/j.physrep.2014.02.00910.1016/j.physrep.2014.02.009

Chluba, J., Nagai, D., Sazonov, S., & Nelson, K. 2012, Monthly Notices of the Royal Astronomical Society, 426, 510, doi: http://doi.org/10.1111/j.1365-2966.2012.21741.x10.1111/j.1365-2966.2012.21741.x

Day, P. K., LeDuc, H. G., Mazin, B. A., Vayonakis, A., & Zmuidzinas, J. 2003, Nature, 425, 817–821, doi: http://doi.org/10.1038/nature0203710.1038/nature02037

de Visser, P. 2014, PhD thesis

DES Collaboration, Abbott, T. M. C., Adamow, M., et al. 2021, arXiv e-prints, arXiv:2101.05765. https://arxiv.org/abs/2101.05765https://arxiv.org/abs/2101.05765

Devlin, M. J., Ade, P. A. R., Aretxaga, I., et al. 2009, , 458, 737, doi: http://doi.org/10.1038/nature0791810.1038/nature07918

Doyle, S., Mauskopf, P., Naylon, J., Porch, A., & Duncombe, C. 2008, Journal of Low Temperature Physics, 151, 530, doi: http://doi.org/10.1007/s10909-007-9685-210.1007/s10909-007-9685-2

Duivenvoorden, S., Oliver, S., Béthermin, M., et al. 2020, , 491, 1355, doi: http://doi.org/10.1093/mnras/stz311010.1093/mnras/stz3110

Everett, W. B., Zhang, L., Crawford, T. M., et al. 2020, , 900, 55, doi: http://doi.org/10.3847/1538-4357/ab9df710.3847/1538-4357/ab9df7

Filipovic, D. F., Gearhart, S. S., & Rebeiz, G. M. 1993, IEEE Transactions on Microwave Theory Techniques, 41, 1738, doi: http://doi.org/10.1109/22.24791910.1109/22.247919

Fixsen, D. J., Cheng, E. S., Gales, J. M., et al. 1996, , 473, 576, doi: http://doi.org/10.1086/17817310.1086/178173

Flaugher, B., Diehl, H. T., Honscheid, K., et al. 2015, , 150, 150, doi: http://doi.org/10.1088/0004-6256/150/5/15010.1088/0004-6256/150/5/150

Galitzki, N., Ade, P. A. R., Angilè, F. E., et al. 2014, Journal of Astronomical Instrumentation, 3, 1440001, doi: http://doi.org/10.1142/S225117171440001710.1142/S2251171714400017

Gao, J. 2008, PhD thesis

Geerlings, K. L. 2013, PhD thesis

Gorter, C., & Casimir, H. 1934, Physica, 1, 306, doi: http://doi.org/https://doi.org/10.1016/S0031-8914(34)90037-9https://doi.org/10.1016/S0031-8914(34)90037-9

Griffin, M. J., Abergel, A., Abreu, A., et al. 2010, , 518, L3, doi: http://doi.org/10.1051/0004-6361/20101451910.1051/0004-6361/201014519

Hanson, D., Hoover, S., Crites, A., et al. 2013, , 111, 141301, doi: http://doi.org/10.1103/PhysRevLett.111.14130110.1103/PhysRevLett.111.141301

Hanson, D., Hoover, S., Crites, A., et al. 2013, Phys. Rev. Lett., 111, 141301, doi: http://doi.org/10.1103/PhysRevLett.111.14130110.1103/PhysRevLett.111.141301

Heinis, S., Buat, V., Béthermin, M., et al. 2013, , 429, 1113, doi: http://doi.org/10.1093/mnras/sts39710.1093/mnras/sts397

Henning, J. W., Sayre, J. T., Reichardt, C. L., et al. 2018, , 852, 97, doi: http://doi.org/10.3847/1538-4357/aa9ff410.3847/1538-4357/aa9ff4

Holder, G. P., Viero, M. P., Zahn, O., et al. 2013, , 771, L16, doi: http://doi.org/10.1088/2041-8205/771/1/L1610.1088/2041-8205/771/1/L16

Hui, H., Ade, P. A. R., Ahmed, Z., et al. 2018, in Society of Photo-Optical Instrumentation Engineers (SPIE) Conference Series, Vol. 10708, Millimeter, Submillimeter, and Far-Infrared Detectors and Instrumentation for Astronomy IX, ed. J. Zmuidzinas & J.-R. Gao, 1070807, doi: http://doi.org/10.1117/12.231172510.1117/12.2311725

Ilbert, O., Arnouts, S., McCracken, H. J., et al. 2006, , 457, 841, doi: http://doi.org/10.1051/0004-6361:2006513810.1051/0004-6361:20065138

Ilbert, O., Capak, P., Salvato, M., et al. 2009, , 690, 1236, doi: http://doi.org/10.1088/0004-637X/690/2/123610.1088/0004-637X/690/2/1236

Imara, N., Loeb, A., Johnson, B. D., Conroy, C., & Behroozi, P. 2018, , 854, 36, doi: http://doi.org/10.3847/1538-4357/aaa3f010.3847/1538-4357/aaa3f0

Johnson, B. R., Flanigan, D., Abitbol, M. H., et al. 2018, Journal of Low Temperature Physics, 193, 103, doi: http://doi.org/10.1007/s10909-018-2032-y10.1007/s10909-018-2032-y

Kaplan, S. B., Chi, C. C., Langenberg, D. N., et al. 1976, Phys. Rev. B, 14, 4854, doi: http://doi.org/10.1103/PhysRevB.14.485410.1103/PhysRevB.14.4854

Kovac, J. M., Leitch, E. M., Pryke, C., et al. 2002, , 420, 772, doi: http://doi.org/10.1038/nature0126910.1038/nature01269

Kozorezov, A. G., Volkov, A. F., Wigmore, J. K., et al. 2000, Phys. Rev. B, 61, 11807, doi: http://doi.org/10.1103/PhysRevB.61.1180710.1103/PhysRevB.61.11807

Kriek, M., van Dokkum, P. G., Labbé, I., et al. 2009, , 700, 221, doi: http://doi.org/10.1088/0004-637X/700/1/22110.1088/0004-637X/700/1/221

Kurczynski, P., & Gawiser, E. 2010, , 139, 1592, doi: http://doi.org/10.1088/0004-6256/139/4/159210.1088/0004-6256/139/4/1592

Levenson, L., Marsden, G., Zemcov, M., et al. 2010, , 409, 83, doi: http://doi.org/10.1111/j.1365-2966.2010.17771.x10.1111/j.1365-2966.2010.17771.x

Lewis, A., & Challinor, A. 2006, , 429, 1, doi: http://doi.org/10.1016/j.physrep.2006.03.00210.1016/j.physre

Magnelli, B., Lutz, D., Saintonge, A., et al. 2014, , 561, A86, doi: http://doi.org/10.1051/0004-6361/20132221710.1051/0004-6361/201322217

Marsden, G., Ade, P. A. R., Bock, J. J., et al. 2009, , 707, 1729, doi: http://doi.org/10.1088/0004-637X/707/2/172910.1088/0004-637X/707/2/1729

Mattis, D. C., & Bardeen, J. 1958, Phys. Rev., 111, 412, doi: http://doi.org/10.1103/PhysRev.111.41210.1103/PhysRev.111.412

Mazin, B. A. 2005, PhD thesis

McCarrick, H., Jones, G., Johnson, B. R., et al. 2018, , 610, A45, doi: http://doi.org/10.1051/0004-6361/20173204410.1051/0004-6361/201732044

McGeehan, R., Barry, P. S., Shirokoff, E., et al. 2018, Journal of Low Temperature Physics, 193, 1024, doi: http://doi.org/10.1007/s10909-018-2061-610.1007/s10909-018-2061-6

Meinke, J., Böckmann, K., Cohen, S., et al. 2021, , 913, 88, doi: http://doi.org/10.3847/1538-4357/abf2b410.3847/1538-4357/abf2b4

Millard, J. S., Eales, S. A., Smith, M. W. L., et al. 2020, , 494, 293, doi: http://doi.org/10.1093/mnras/staa60910.1093/mnras/staa609

Mocanu, L. M., Crawford, T. M., Vieira, J. D., et al. 2013, , 779, 61, doi: http://doi.org/10.1088/0004-637X/779/1/6110.1088/0004-637X/779/1/61

Nozawa, S., Itoh, N., Kawana, Y., & Kohyama, Y. 2000, The Astrophysical Journal, 536, 31, doi: http://doi.org/10.1086/30893810.1086/308938

Oliver, S. J., Bock, J., Altieri, B., et al. 2012, , 424, 1614, doi: http://doi.org/10.1111/j.1365-2966.2012.20912.x10.1111/j.1365-2966.2012.20912.x

Pascale, E., Ade, P. A. R., Bock, J. J., et al. 2008, , 681, 400, doi: http://doi.org/10.1086/58854110.1086/588541

Pascale, E., Ade, P. A. R., Bock, J. J., et al. 2009, , 707, 1740, doi: http://doi.org/10.1088/0004-637X/707/2/174010.1088/0004-637X/707/2/1740

Penzias, A. A., & Wilson, R. W. 1965, Astrophys. J., 142, 419, doi: http://doi.org/10.1086/14830710.1086/148307

Planck Collaboration, Ade, P. A. R., Aghanim, N., et al. 2014, , 571, A18, doi: http://doi.org/10.1051/0004-6361/20132154010.1051/0004-6361/201321540

Planck Collaboration, Aghanim, N., Akrami, Y., et al. 2020, , 641, A1, doi: http://doi.org/10.1051/0004-6361/20183388010.1051/0004-6361/201833880

Pozar, D. M. 2005, Microwave engineering; 3rd ed. (Hoboken, NJ: Wiley). https://cds.cern.ch/record/882338https://cds.cern.ch/record/882338

Puget, J. L., Abergel, A., Bernard, J. P., et al. 1996, , 308, L5

Quealy, E. 2012, PhD thesis

Reichardt, C. L., Patil, S., Ade, P. A. R., et al. 2021, , 908, 199, doi: http://doi.org/10.3847/1538-4357/abd40710.3847/1538-4357/abd407

Roseboom, I. G., Oliver, S. J., Kunz, M., et al. 2010, , 409, 48, doi: http://doi.org/10.1111/j.1365-2966.2010.17634.x10.1111/j.1365-2966.2010.17634.x

Schaffer, K. K., Crawford, T. M., Aird, K. A., et al. 2011, , 743, 90, doi: http://doi.org/10.1088/0004-637X/743/1/9010.1088/0004-637X/743/1/90

Shirokoff, E., Barry, P. S., Bradford, C. M., et al. 2012, in Society of Photo-Optical Instrumentation Engineers (SPIE) Conference Series, Vol. 8452, Millimeter, Submillimeter, and Far-Infrared Detectors and Instrumentation for Astronomy VI, ed. W. S. Holland & J. Zmuidzinas, 84520R, doi: http://doi.org/10.1117/12.92707010.1117/12.927070

Story, K. T., Reichardt, C. L., Hou, Z., et al. 2013, , 779, 86, doi: http://doi.org/10.1088/0004-637X/779/1/8610.1088/0004-637X/779/1/86

Sunyaev, R. A., & Zeldovich, Y. B. 1972, Comments on Astrophysics and Space Physics, 4, 173

Swenson, L. J., Day, P. K., Dowell, C. D., et al. 2012, in Society of Photo-Optical Instrumentation Engineers (SPIE) Conference Series, Vol. 8452, Millimeter, Submillimeter, and Far-Infrared Detectors and Instrumentation for Astronomy VI, ed. W. S. Holland & J. Zmuidzinas, 84520P, doi: http://doi.org/10.1117/12.92622310.1117/12.926223

Tang, Q. Y., Barry, P. S., Basu Thakur, R., et al. 2018, Journal of Low Temperature Physics, 193, 149, doi: http://doi.org/10.1007/s10909-018-1941-010.1007/s10909-018-1941-0

Tang, Q. Y., Barry, P. S., Cecil, T. W., & Shirokoff, E. 2020, Fabrication of OMT-Coupled Kinetic Inductance Detector for CMB Detection, 199, 362, doi: http://doi.org/10.1007/s10909-020-02341-510.1007/s10909-020-02341-5

The Dark Energy Survey Collaboration. 2005, arXiv e-prints, astro. https://arxiv.org/abs/astro-ph/0510346https://arxiv.org/abs/astro-ph/0510346

Triani, D. P., Sinha, M., Croton, D. J., Dwek, E., & Pacifici, C. 2021, , 503, 1005, doi: http://doi.org/10.1093/mnras/stab55810.1093/mnras/stab558

Viero, M. P., Moncelsi, L., Quadri, R. F., et al. 2013a, , 779, 32, doi: http://doi.org/10.1088/0004-637X/779/1/3210.1088/0004-637X/779/1/32

Viero, M. P., Wang, L., Zemcov, M., et al. 2013b, , 772, 77, doi: http://doi.org/10.1088/0004-637X/772/1/7710.1088/0004-637X/772/1/77

Viero, M. P., Reichardt, C. L., Benson, B. A., et al. 2019, , 881, 96, doi: http://doi.org/10.3847/1538-4357/ab2da010.3847/1538-4357/ab2da0

Wright, E. L. 1979, , 232, 348, doi: http://doi.org/10.1086/15729410.1086/157294

Zmuidzinas, J. 2012, Annual Review of Condensed Matter Physics, 3, 169, doi: http://doi.org/10.1146/annurev-conmatphys-020911-12502210.1146/annurev-conmatphys-020911-125022